Multiphysics Simulation of Nanostructured Semiconductor Devices

Wenjun Jiang

A dissertation
submitted in partial fulfilment of the
requirements for the degree of

Doctor of Philosophy

University of Washington

2013

Reading Committee:

Scott T. Dunham, Chair

John J. Rehr

Marjorie A. Olmstead

Program Authorized to Offer Degree:
UW Physics

University of Washington

Abstract

Multiphysics Simulation of Nanostructured Semiconductor Devices

Wenjun Jiang

Chair of the Supervisory Committee:
Professor Scott T. Dunham
Department of Electrical Engineering

This dissertation describes how to utilize multiphysics simulation techniques to develop physical (optics and device) models of nanostructured semiconductor devices. A hierarchy of approaches (ab − initio, continuum, transfer-matrix, finite-difference time-domain) is used to bridge the gaps in computational efficiency and physical accuracy. This modeling approach is demonstrated by investigating several challenging applications: organic solar cells and atomic force microscope direct writing.

In the first application, optics and device simulation techniques are coupled together with the aim of improving organic solar cell efficiency. Transfer matrix method (TMM) is used to understand the photon distribution and absorption in photovoltaics with layered structure. The optimized thickness of organic light-absorbing layer can be matched accurately with experiments. We also investigate the light absorption enhancement due to surface-plasmonic effect in presence of silver nano-prisms. Finite-difference time-domain (FDTD) solutions of Maxwell′s equations suggest benefits of utilizing silver nano-prisms only for ultra-thin organic light-absorbing layer (thickness < 50 nm). Device models involve the Poisson equation, charge continuity equations, and organic-specific singlet exciton generation/dissociation equation. By considering the effect from deep trap states, we calibrate our model via matching the quantum efficiency and current-voltage curves with experimental data. We can also control the current-voltage response by tuning the work-function of metal nano-prisms, due to tunneling current through ultra-thin dielectric layer between

silver nano-prism and surrounding organic light-absorbing material, which leads to charge accumulation. Finally, by combining optics and device simulation, we identify a trade-off between plasmon-mediated optical enhancement and optical and electronic losses associated with low aspect-ratio silver nanoprisms in plasmonic organic solar cells. We predict up to 26% enhancement of power conversion efficiency (PCE) for active layer thicknesses less than 50 nm.

The second application addresses the effect of temporary-negative-ion (TNI) generation and dissociation in the liquid precursor located between the tip of atomic force microscope and silicon wafer coated with SiO_2. $Ab - initio$ calculations were used to extract the density of states of the TNI′s at their energy-favorable states. Device simulation illustrates nonlocalized Fowler-Nordheim type of tunneling current, in which the current density is a function of applied electric field. Based on the device simulation models considering the TNI′ tunneling effect, we can match the current-voltage curve of direct AFM writing with experiments under various applied voltages. We also developed a methodology to extract the shape and deposition rate of silicon/germanium nanostructures under extremely high external electric field at the tip of atomic force microscopy. Finally, we derived an analytical model that can predict the deposited shape of silicon/germanium nanostructures as a function of AFM writing voltage and speed.

TABLE OF CONTENTS

Page

LIST OF FIGURES

LIST OF TABLES

GLOSSARY

BHJ: bulk heterojunction.

DPG: diphenylgermane.

DPS: diphenylsilane.

FDTD: finite-difference time-domain method.

FF: fill factor.

FFT: fast Fourier transform.

FEM: finite element method.

HOMO: highest occupied molecular orbital.

ITO: tin-doped indium oxide.

I-V: current-voltage.

J_{SC}: short-circuit current.

LSP: localized surface plasmon.

LUMO: lowest unoccupied molecular orbital.

NP: nanoparticle.

OPV: organic photovoltaics.

OSC: organic solar cell.

P3HT:PCBM: poly(3-hexylthiophene):[6,6]-phenyl-C61-butyric acid methyl ester.

PCE: power conversion efficiency

PEDOT:PSS: poly(3,4-ethylenedioxythiophene) poly(styrenesulfonate).

PML: perfectly matched layer.

P_{MAX}: maximum power density.

SPP: surface plasmon polariton.

RT: ray-tracing method.

TE: transverse electric.

TM: transverse magnetic.

TMM: transfer-matrix method.

TNI: temporary-negative ions.

V_{OC}: open-circuit voltage.

ACKNOWLEDGMENTS

I would like to thank all the people who have helped me with my study, research, and career build-up at the University of Washington. My research is very interdisciplinary from the beginning and we have a wide collaboration with many different research groups on campus and from industry, so I have many people to acknowledge.

I especially want to thank my supervisor, Professor Scott T. Dunham. His wide knowledge, creativity, and logical way of thinking have been of great value for me. His enthusiasms in research and natural sensitivity to finding and solving problems have motivated all the members in the group. I also want to gratefully acknowledge Professor Marjorie A. Olmstead and Professor John J. Rehr for their conscientious reading of my thesis and advice during my PhD study.

Many talented group members in the NanoTechnology Modeling Laboratory have helped me and stimulated my interest in exploring the unknown world: thanks to Renyu Chen, Bart Trzynadlowski, Haoyu Lai, Jason Guo, Doctor Daniel Mutter, Armin Yazdani, Yu Jin, and Shifeng Zhu.

My next thank you goes to my collaborating groups. Without them, my research would be incomplete. I thank Doctor Michael Salvador in Professor David S. Ginger′s group for his collaboration and work with the surface plasmonic effect described in Chapter 5. Also I would acknowledge Stephanie E. Vasko in Professor Marco Rolandis group for the experimental measurements of high-field chemistry at the tip of atomic force microscopy, which is described in Chapter 6.

My doctoral projects come from many different funding resources. I would thank Office of Naval Research (ONR), National Science Foundation (NSF), Semiconductor Research Corporation (SRC), Silicon Wafer Engineering and Defect Science (SiWEDS), and Micron Technology Inc. Their generous support allowed me to fully concentrate my time on research

and this thesis. I especially thank Intel Corporation for their donation of computing clusters on which all my calculations are running.

I also want to appreciate the help from my friends in Seattle during the six years: Jie Liu, Wei Zhang, Xiaolin Duan, Wei Lu, Long Gui, Shuang Zhang, and Yun Zhang. A big thank you goes to Margy Lawrence for her help in my oral English in my first two years of TA job.

Finally, my deepest gratitude goes to my family for their selfless support throughout my life, which I could never fully repay. I am totally indebted to my grandparents, Haolong Jiang and Chaofan Chen, my parents, Shitao Xie and Lian Jiang, for their care and love. I also owe my loving thanks to my wife Jinting Zhang for all the support, encouragement, and understanding during our years of PhD study.

DEDICATION

to my parents, Shitao and Lian

and my dear wife, Jinting

Chapter 1

INTRODUCTION

1.1 Technology Computer-Aided Design

Technology CAD, or Technology Computer-Aided Design (TCAD), has become more and more important in modern semiconductor industry due to the huge cost of research and design based on experiments. TCAD provides fundamental insights into the nanostructured devices, including the modeling of process steps (such as diffusion, ion implantation, and cluster formation), optical distribution, as well as device behavior (based on doping profile, recombination, and trap states) (Fig. 1.2). The accuracy and robustness of TCAD models has been increased dramatically and into the nanoscale due to the fast development of computer hardware, which follows the empirical observation of Moore′s Law (Fig. 1.1), stating that the number of transistors that can be placed on an integrated circuit doubles every 18 months.

Table 1.1: Hierarchy of Multiscale TCAD Approaches

Methods	DFT	MD	KLMC	Continuum
Parameter Interaction	Quantum mechanics	Empirical potentials	Migration barriers	Reaction kinetics
Number of atoms	100	10^4	10^6	10^8
Length scale	1 nm	10 nm	25 nm	100 nm
Time scale	$\approx$ psec	$\approx$ nsec	$\approx$ msec	$\approx$ sec

There are many modeling techniques, based on different levels of time, space, and accuracy requirements. Fig. 1.3 and Table 1.1 illustrates the multi-scale technology computer-aided design (TCAD) hierarchy. $Ab-initio$ methods such as density functional theory

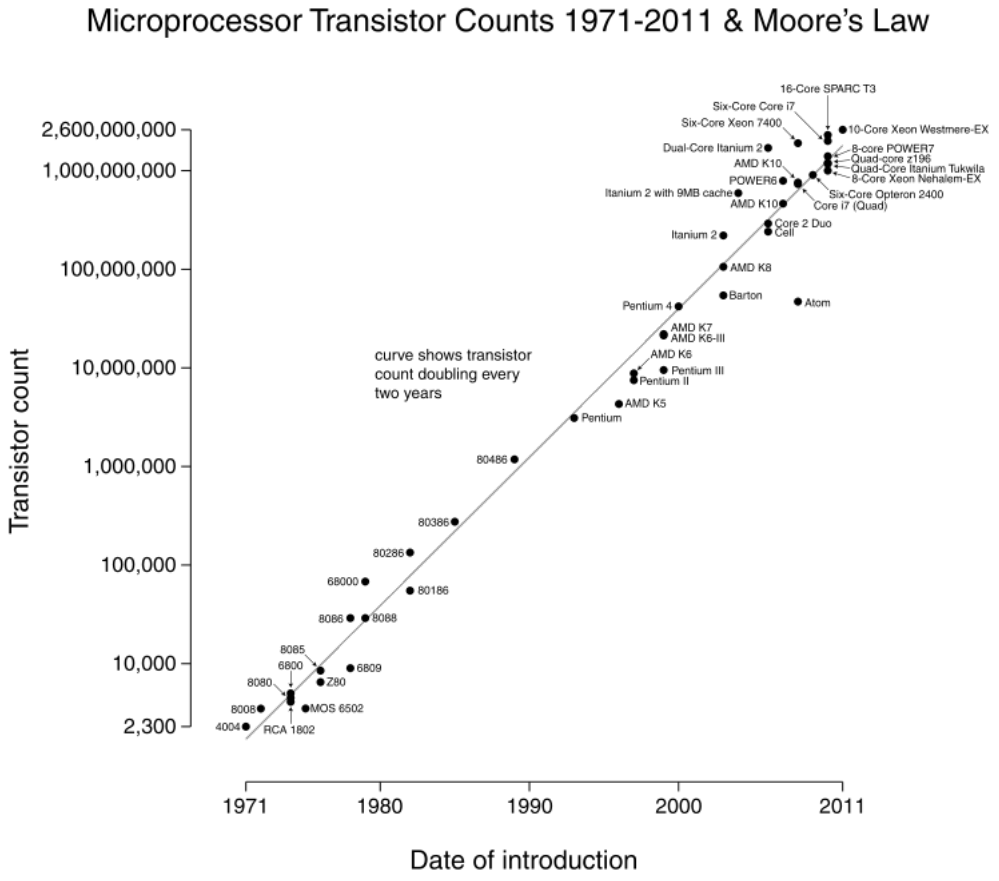

Figure 1.1: Transistor counts for integrated circuits plotted against their dates of introduction. It is clear from the curve that Moore′s law - the doubling of transistor counts for every 18 month still holds. The y-axis is logarithmic, so the line corresponds to exponential growth.

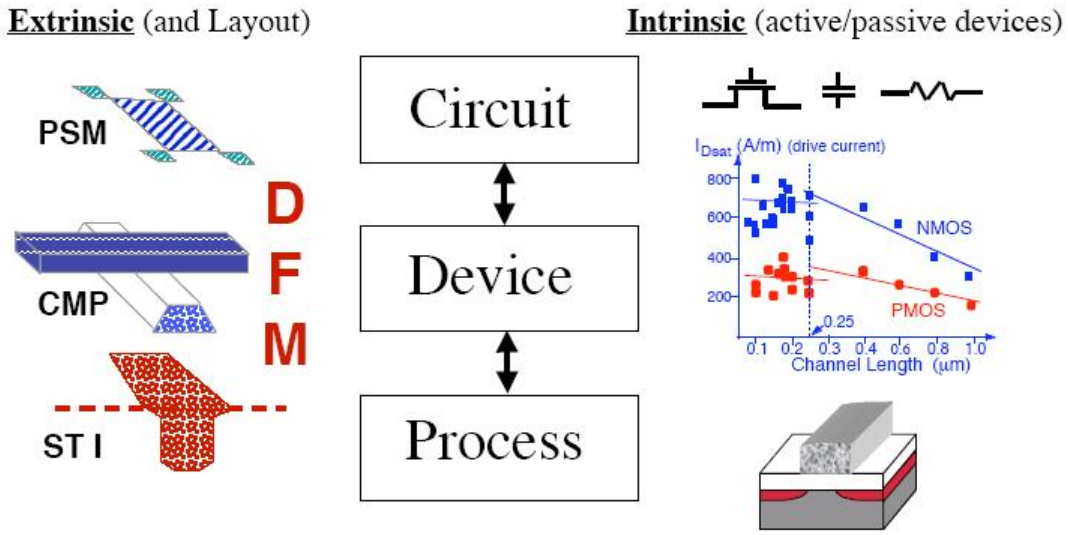

Figure 1.2: Hierarchy of technology CAD tools building from the process level to circuits. Left side icons show typical manufacturing issues; right side icons reflect MOS scaling results based on TCAD.

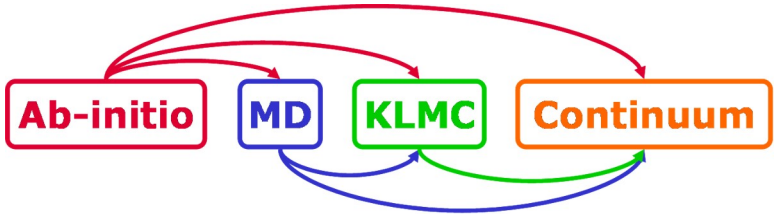

Figure 1.3: Illustration of TCAD Approaches. Density-functional theory (DFT) solves basic Schroedinger's equation, molecular dynamics calculation (MD) utilizes empirical potential, kinetic lattice Monte-Carlo simulation (KLMC) sets up migration barriers and thus define probability for parameters to interact, all these approaches provide input parameters for continuum model.

(DFT) solves the fundamental Schrödinger equation for quantum mechanics with all atomic details, but requires huge computational resources and lowest number of atoms. On the other hand, continuum process, device, and circuit simulation ignore the study of semiconductor physics at the macroscale with the largest regimes. To bridge the time- and space-scale differences between atomic and continuum modeling, molecular dynamics (MD) and kinetic lattice Monte-Carlo (KLMC) simulation are introduced to focus on the nano-scale, with moderate calculation capability of time scale between nanoseconds and milliseconds.

1.2 Energy Consumption

Modern industry depends on the large consumption of energy in various types. Fig. 1.4 illustrates the various types of energy consumption between 1820 and 2000 A.D. It is of no doubt, but still quite shocking, that the total energy consumption increases exponentially since the the industrial revolution. The largest consumption for electricity generation are oil and coal, which are very pollutive. Natural-gas-generated electricity is cleaner, compared to oil and coal, but it still releases a huge amount of green-house gas (such as CO_2 and vapour) into the atmosphere. By contrast, nuclear and hydroelectricity are more expensive, and are environmentally hazardous due to potential nuclear leakage and river channel sedimentation. In recent years, most gasoline provided in U.S. gas stations contains up to 10% biofuel, thus reducing the consumption of non-renewable oil. However, biofuel consumes a huge amount of corns, thus increasing the price of corns (see Fig. 1.5) and having the potential of endanger people who live with corn consumption.

Due to the environmental issued with fossil fuels such as green-house gas emission (more than 90% of green-house gas emission in the United States is from the use of fossil fuels), pollutants emission (such as NO_x, SiO_2, heavy metals, and ashes), as well as the non-renewable nature of fossil fuels, renewable energy receives more and more attention from government support. As illustrated from Fig. 1.6, U.S. Department of Energy (DoE), Venture Capital (VC) and Private Equity (PE) investment on the renewable energy research experiences steady increase, resulting exponentially increasing number of patents.

Among renewable energy research, photovoltaic technology is one of the most attractive and active in current research. Photovoltaic devices have many advantages over other types

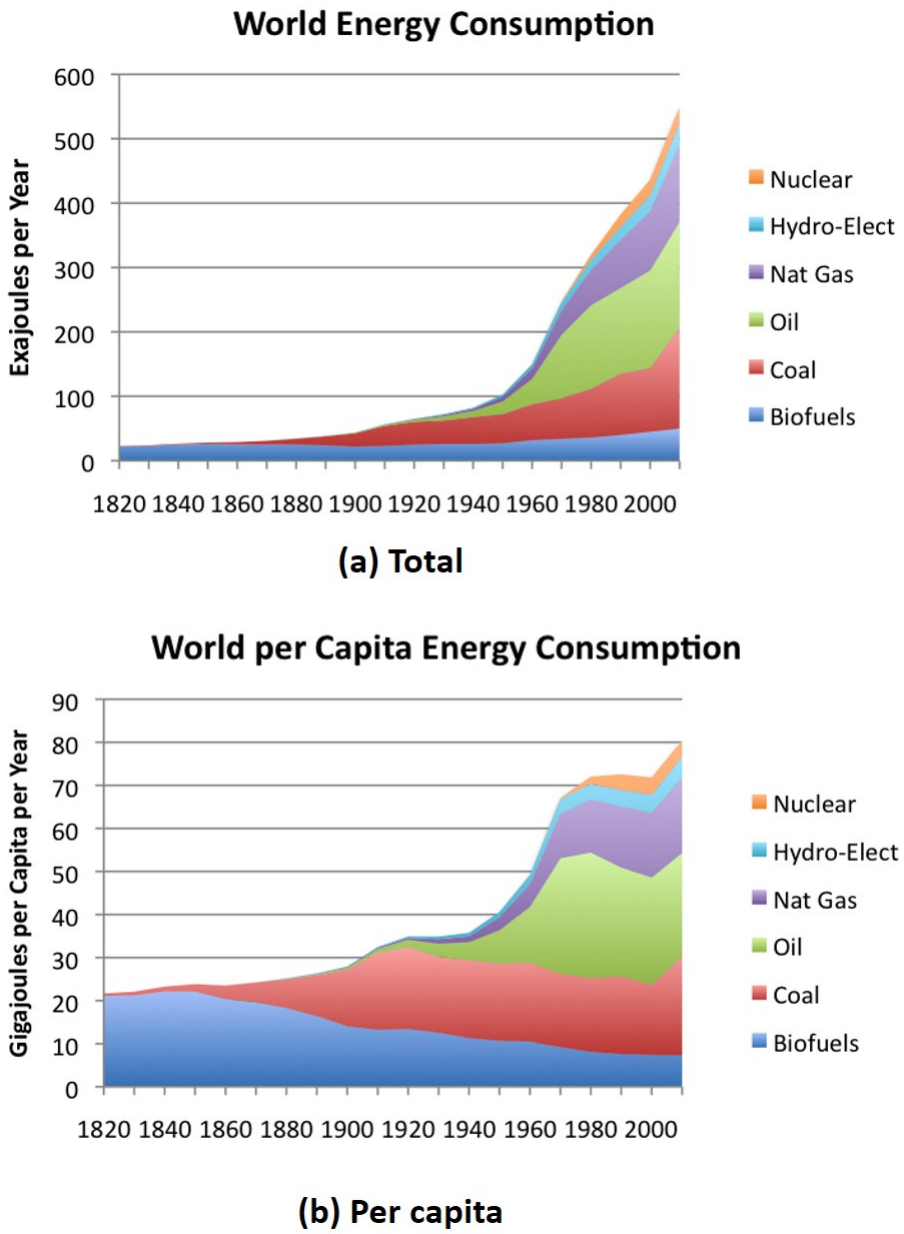

Figure 1.4: World energy consumption from 1820 to 2000 AD, in forms of (a) total energy consumption and (b) energy consumption per capita. Six types of energies are taken into account: 1. nuclear electricity; 2. Hydroelectric power; 3. Natural gas power generation; 4. Oil generated power; 5. Coal power; and 6. Renewable biofuels.

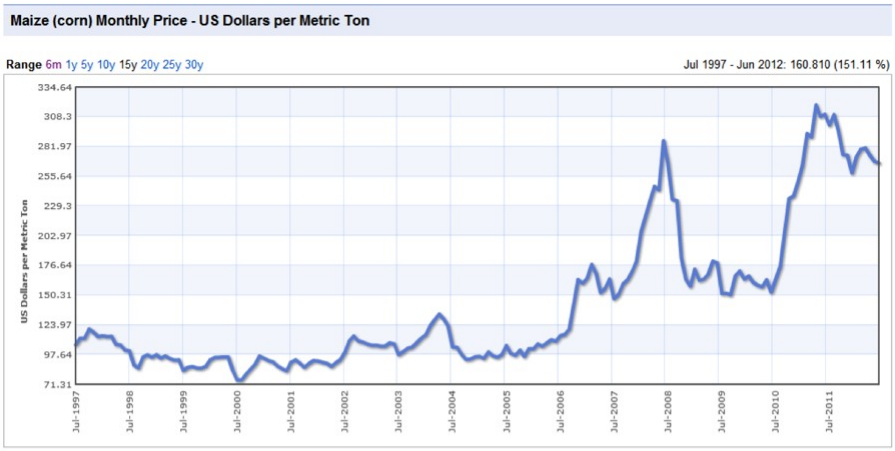

(a)

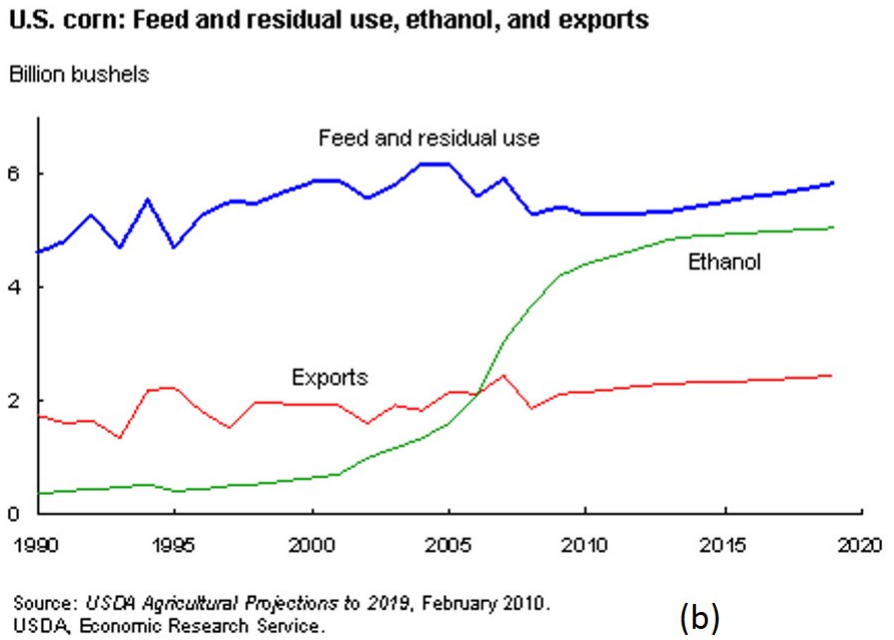

(b)

Figure 1.5: The corn price (a) and consumption (b) in the United States. Notice that the corn monthly price has increased by a factor of 2-3 since 2007, which is consistent with the dramatic increase of bio-ethanol use of maize.

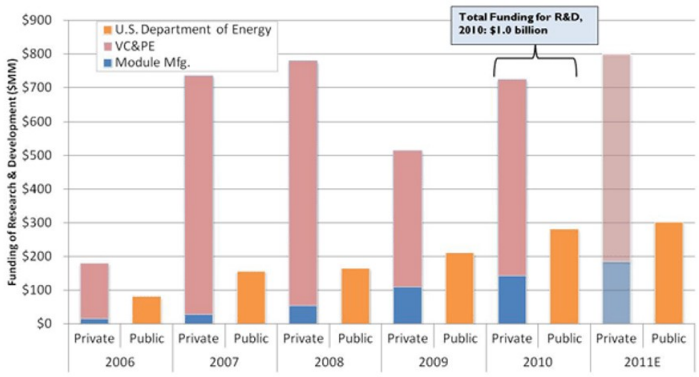

(a)

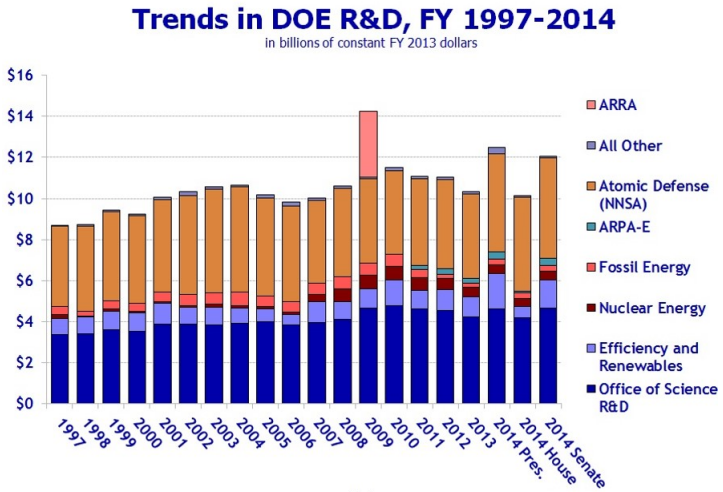

(b)

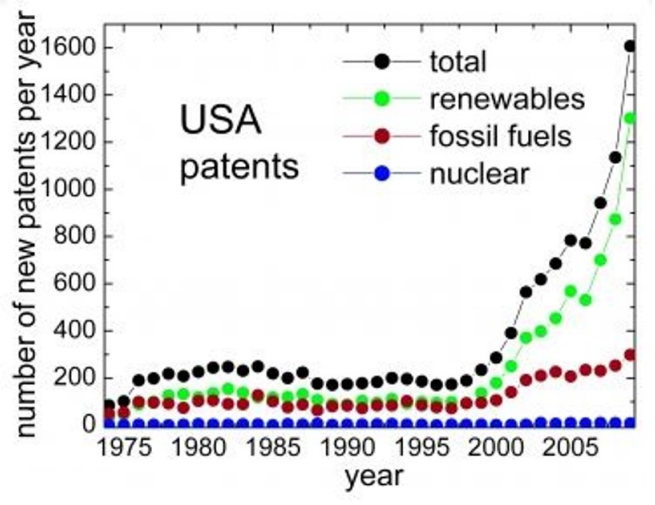

(c)

Figure 1.6: Funding and patents trend for renewable energy research.

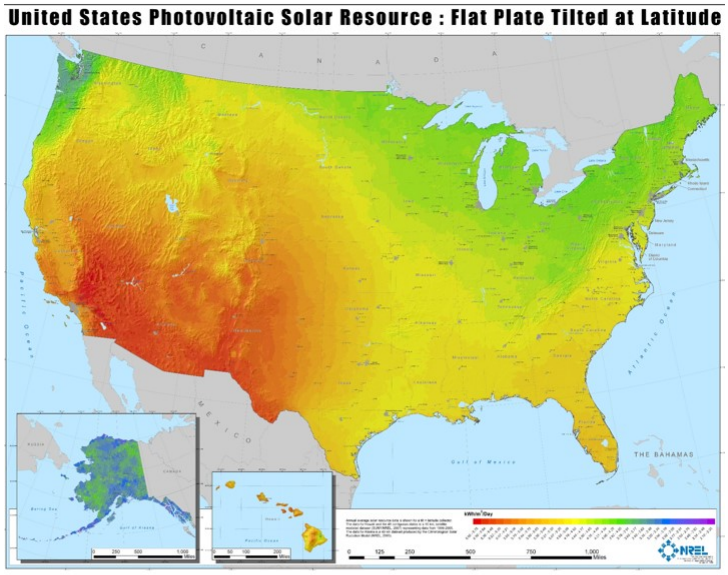

(a)

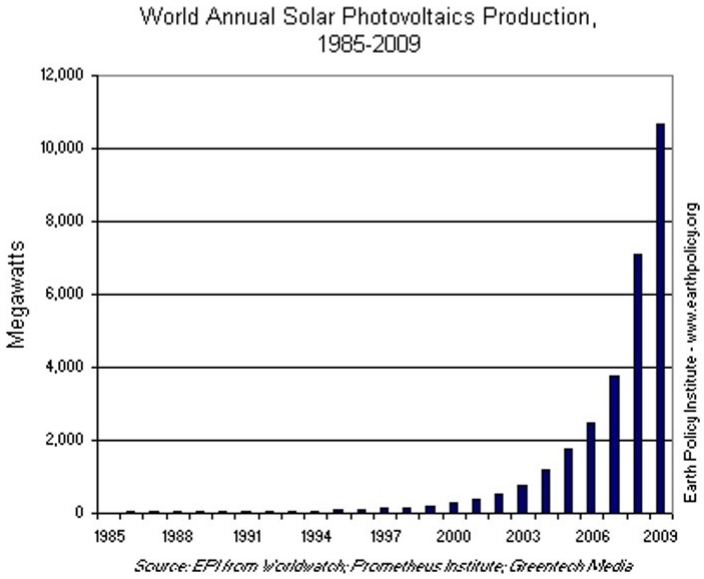

(b)

Figure 1.7: (a). The solar irradiation map of the United States; (b). The world annual solar photovoltaics production from 1985 to 2009 A.D.

of energy conversion: direct conversion from solar energy into electricity, no noise or high temperature during generation, no pollution or waste generation. The U.S. has abundant solar irradiation resources, especially in the southwest region such as New Mexico, Arizona, and Nevada. Even in the rainy Seattle, the solar energy in summer is very rich. By developing sophisticated but relatively cheap photovoltaic technology, the sun can offer enough electricity that we do not have to burn coal or oil that can lead to air pollution and global warming.

1.3 Conductive Polymers and Organic Solar Cells

Since it was first demonstrated that organic materials could be used to conduct electrons, many efforts have been concentrated on using organic materials to absorb sunlight. Three main types of organic photovoltaic devices (OPV) have been developed, that is, single layer OPV, double layered OPV, and bulk heterojunction OPV [1, 2, 3]. Currently, a record efficiency of 11.1% has been achieved [4]. However, at least 15% efficiency needs to be achieved to beat silicon-based solar cells from the cost point of view [5]. Many process, optics, and device engineering techniques have been used to absorb more light in organic active layers by properly designing back metal reflector [6] and reducing the recombination rate by controling the phase-separation morphology of heterojunctions [7].

1.3.1 Working Principle of Organic Photovoltaic Devices

Fig. 1.8 illustrates the basic working principle of a typical organic photovoltaic device. In total, there are five steps for turning incident light into electricity, as shown in Table 1.2.

Organic solar cell has the advantages of being transparent, flexible, and has low production costs in high volumes. Combined with the flexibility of organic molecules, organic solar cells are potentially cost-effective for photovoltaic applications. The optical absorption coefficient of organic molecules is high, so a large amount of light can be absorbed with a small amount of materials. However, during the fabrication process of P3HT:PCBM, which are the most commonly-used light-absorbing materials for polymer-based solar cells, heat annealing after the spin-on process is essential for the formation of charge-carrier conduction channels. Due to its fabrication nature, the main disadvantages associated with organic

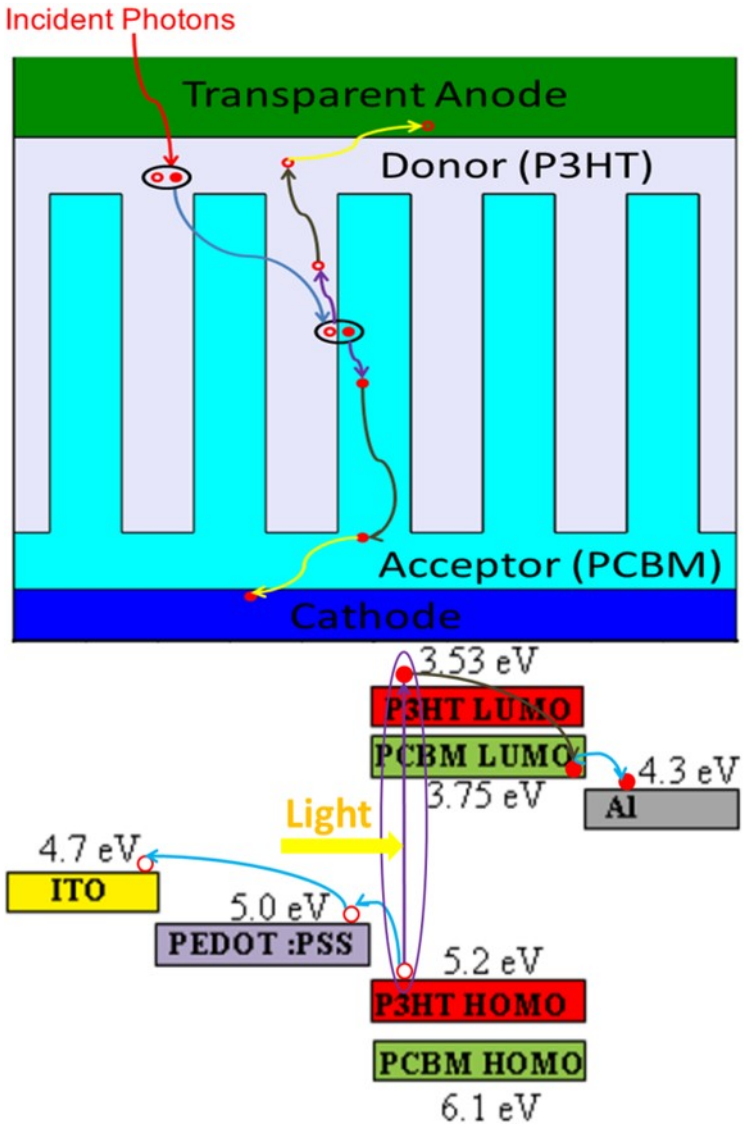

Figure 1.8: Illustration of the working principle of organic photovoltaic devices. It consists of five steps: 1. Incident photon absorption; 2. Exciton diffusion toward P3HT:PCBM interface; 3. Exciton dissociation at P3HT:PCBM interface; 4. Electron/hole diffusion toward electrodes; 5. Carrier collection at electrodes.

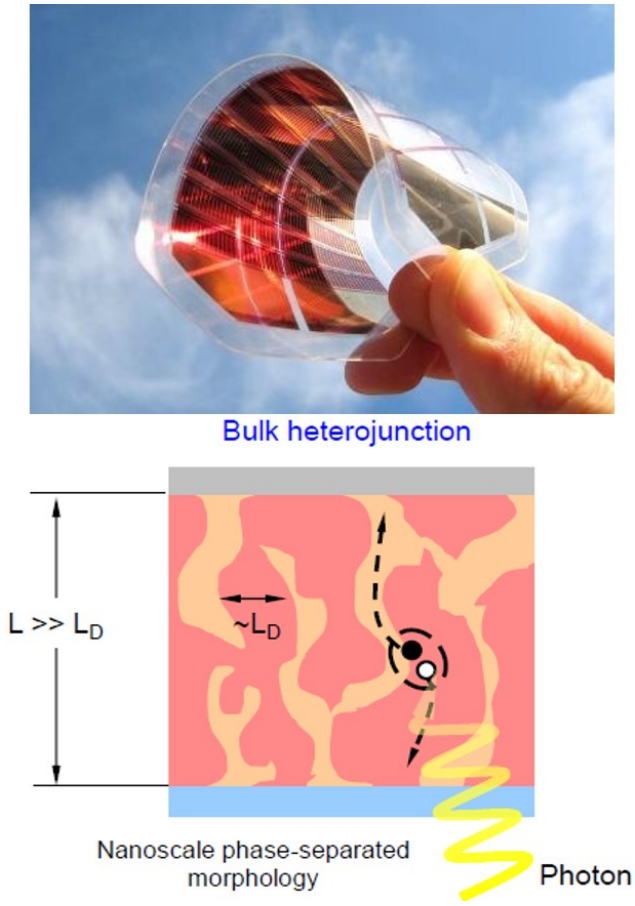

Figure 1.9: Advantage and disadvantage of utilizing organic photovoltaic devices. (a) illustrates the flexibility of a transparent OPV; while (b) illustrates a huge difference in the very short exciton diffusion length ($L_D \approx 10$ nm) vs. long photon absorption length ($L \approx 180$ nm).

Table 1.2: Steps of Organic Solar Cell Operation

Step	Process	Place
1	Incident photon absorption	P3HT:PCBM bulk
2	Exciton diffusion toward P3HT:PCBM interface	P3HT:PCBM bulk
3	Exciton dissociation	P3HT:PCBM interface
4	Electron/hole diffusion toward electrodes	Electrons in PCBM, holes in P3HT
5	Carrier collection	Electrons at cathode, holes at anode

photovoltaic cells are low efficiency, low stability and low strength compared to inorganic photovoltaic cells.

From the electronic device point of view, the difference in the charge-carrier generation and collection mechanism between silicon-based solar cells and polymer solar cells is that the latter has singlet excitons with large binding energy, known as Frenkel excitons. The generated singlet excitons then dissociate at the P3HT:PCBM interface, providing electrons and holes as the charge carrier outcome.

1.4 Light Trapping Techniques

A key challenge for organic solar cells is that the absorption is relatively weak compared to silicon solar cells, due to the low light absorption coefficient. On the other hand, OPV cells generate electron-hole pairs called excitons in presence of incoming photons. These excitons only have a diffusion length on the order of $\approx$ 10 nm before recombine. This mismatch between light absorption length ($\approx$ 100 - 200 nm) and exciton diffusion length prevents the OPV efficiency from being high enough to compete with silicon-based solar cells. Therefore, it is always a trade-off between light absorption percentage and device performance for organic solar cells with layered structure. Therefore, light trapping techniques are essential to reduce the active layer thickness without hurting the light absorption dramatically.

1.4.1 Surface Plasmonic Effect

Recent advances in nanotechnology allow materials to be fabricated and characterized on the nanoscale [8, 9], which enable researchers to control the properties of materials to reveal new aspects of science and to find new applications. Surface plasmons are of great interest to many research areas ranging from physics, materials science and chemistry to biology. Silver nanoparticles are of particular interest due to high conductivity, the LSPR tunability, and thickness of adjacent materials precisely. For example, surface plasmons are under research for their promising potential in transformational optics [10], magneto-optics [11], optical sensors [12], light-emitting diodes [13], and solar cells [14].

According to Mie theory, a nanoparticle with random shape has the total electric and magnetic field in the form of:

$$\begin{cases} \mathbf{E}_{tot} = \mathbf{E}_{inc} + \mathbf{E}_{sca} \\ \mathbf{H}_{tot} = \mathbf{H}_{inc} + \mathbf{H}_{sca} \end{cases} \tag{1.1}$$

where $\mathcal{E}_{\mathrm{tot}}$ and $\mathcal{H}_{\mathrm{tot}}$ are total electric/magnetic field, $\mathcal{E}_{\mathrm{inc}}$ and $\mathcal{H}_{\mathrm{inc}}$ are incident electric/magnetic field, and $\mathcal{E}_{\mathrm{sca}}$ and $\mathcal{H}_{\mathrm{ca}}$ are scattering electric/magnetic field, respectively.

So the Poynting vector, which is the electromagnetic power flow, can be written as:

$$\mathbf{S}_{tot} = \frac{1}{2} Re\left\{\mathbf{E}_{tot} \times \mathbf{H}^*_{tot}\right\} = \frac{1}{2} Re\left\{(\mathbf{E}_{inc} + \mathbf{E}_{sca}) \times (\mathbf{H}^*_{inc} + \mathbf{H}^*_{sca})\right\} \tag{1.2}$$

It is generally difficult to calculate the energy absorbed in a nanoparticle with random shape. C. F. Bohren et al calculated the absorption in a spherical region of surface area A by using Riccati-Bessel function:

$$W_{abs} = -\oint \mathbf{S}_{tot} \cdot \mathrm{d}\mathbf{A} \tag{1.3}$$

$$= -\oint \frac{1}{2} Re\left\{(\mathbf{E}_{inc} + \mathbf{E}_{sca}) \times (\mathbf{H}^*_{inc} + \mathbf{H}^*_{sca})\right\} \cdot \mathrm{d}\mathbf{A} \tag{1.4}$$

$$= \frac{\pi |E_0|^2}{\omega\mu} \sum_{n=1}^{\infty} Re\left\{i \cdot \tfrac{2n+1}{k} A_n\right\} \tag{1.5}$$

where $\mathrm{A_n} = \psi'_{\mathrm{n}}\psi^*_{\mathrm{n}} - \psi_{\mathrm{n}}\psi'^*_{\mathrm{n}} + \mathrm{b_n}\xi_{\mathrm{n}}\psi'^*_{\mathrm{n}} - \mathrm{a_n}\xi'_{\mathrm{n}}\psi^*_{\mathrm{n}} + \mathrm{a^*_n}\psi'_{\mathrm{n}}\xi^*_{\mathrm{n}} + \mathrm{b^*_n}\psi_{\mathrm{n}}\xi^*_{\mathrm{n}} - |\mathrm{b_n}|^2\,\xi_{\mathrm{n}}\xi'^*_{\mathrm{n}} + |\mathrm{a_n}|^2\,\xi'_{\mathrm{n}}\xi^*_{\mathrm{n}}$

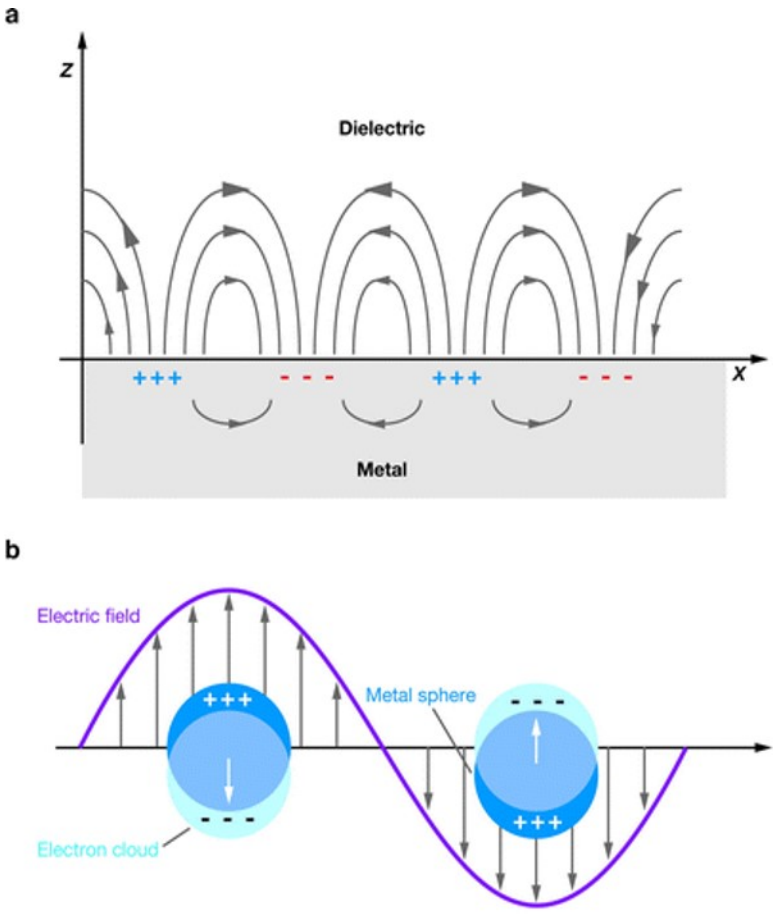

Figure 1.10: Illustration of plasmon excitation due to the presence of nano-particles. (a). Propagating surface plasmon. Plasmons propagate along metal / dielectric interface; (b). Localized surface plasmon for nano-particle size much smaller than incident light wavelength. Plasmon oscillate locally around the nano-particles.

with $\psi_n = \rho \cdot j_n(\rho)$ and $\xi_n = \rho \cdot h_n^{(1)}(\rho)$ are Riccati-Bessel functions, in which $j_n(\rho)$ and $h_n^{(1)}(\rho)$ are spherical Bessel functions of 1st and 3rd kind.

Eq. 1.3 clearly illustrates the square-dependence of energy absorbed in the nanoparticle, W_{abs}, on the electric field, E_0. Thus, increasing the electric field in light absorber material will lead to enhancement of energy absorption.

Recently, metallic nanoparticles/nano-gratings have received much attention due to their capability of energy concentration and tunability according to solar spectrum. In general, plasmonic effect can be classified into two modes: propagating surface plasmons (SPPs) and localized surface plasmons (LSPs), as illustrated in Fig. 1.10. For SPPs, energy flow along the metal/dielectric interface; while for LSPs, the energy is concentrated very locally. Atwater et al. reviewed the plasmonic light trapping techniques and classified them into three categories [15]: (1) metal nanoparticles serve as scattering centers on top of solar cells (Fig. 1.11(a)), (2) metal nanoparticles serve as nano-antennas inside the light absorber material (Fig. 1.11(b)), and (3) metal nano-grating structure at the metal backcontact (Fig. 1.11(c)).

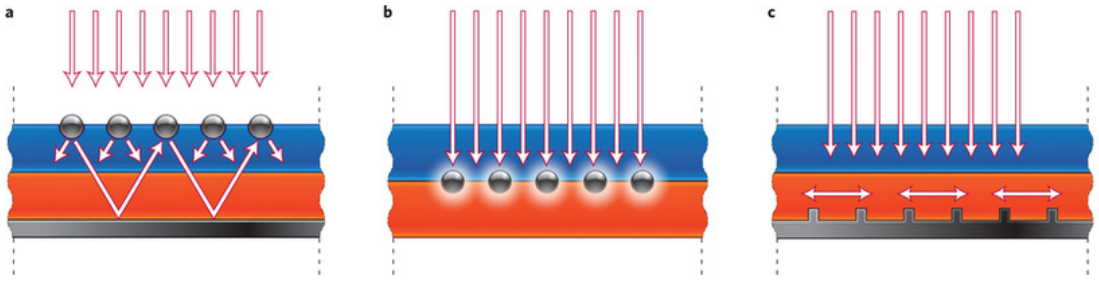

Figure 1.11: Plasmonic light trapping schemes for thin-film solar cells [86]. (a). Light trapping by scattering from metal nanostructures at the surface of the solar cell; (b). Light trapping by excitation of localized surface plasmons in particles embedded in the active layer; (c). Light trapping by the excitation of surface plasmon polaritons at the metal/active layer interface.

1.5 Tunneling Effect of Atomic Force Microscopy

Scanning probe microscopy can confine chemical reactions at the nanoscale through the delivery of specific stimuli or reactants to a small area of the sample surface. One common strategy for reaction confinement is to apply a moderate bias between the tip and the sample. In a humid environment, the water meniscus at the tip-sample interface is often described as a nanoscale electrochemical cell where H+ and OH- are created. The extremely high electric field ($> 10^9$V/m) arising from tip-sample proximity directs the desired ions onto the sample, which is oxidized or reduced depending on bias. In this fashion, the field-induced oxidation or reduction of conducting substrates and organic monolayers has been demonstrated. Recent efforts at replacing the water meniscus in the tip-sample gap with menisci of organic and inorganic molecules have introduced a novel class of chemical reactions that do not seem to follow a clear electrochemical pathway. It has been previously theorized that these reactions are triggered by the high electric field and are analogous to the processes occurring in field ionization microscopy. These reactions include self-assembled monolayer activation, polymer cross linking, sulfur polymerization, and localized synthesis of carbon nanostructures.

1.5.1 Tunneling Mechanisms in Semiconductor Devices

Fowler-Nordheim tunneling is the quantum-mechanical tunneling of electrons through a triangular barrier created at the surface of a conductor by applying a very high electric field. It has two characteristics: (1). The barrier is triangular; (2). Electrons only tunnel through part of the insulating layer, as illustrated in Fig. 1.12(a). After tunneling through the triangle barrier, the rest of the insulating layer does not block the current flow. In this manner, the whole insulating layer impacts the current indirectly by influencing the electric field. The current of Fowler-Nordheim tunneling can be written as [16]:

$$J = \frac{q^2\mathcal{E}^2}{16\pi^2\hbar\phi_{ox}} exp\left[-\frac{4\sqrt{2m^*}\left(q\phi_{ox}\right)^{3/2}}{3\hbar q\mathcal{E}}\right] = C_4\mathcal{E}^2 exp\left(-\frac{C_5}{\mathcal{E}}\right) \qquad (1.6)$$

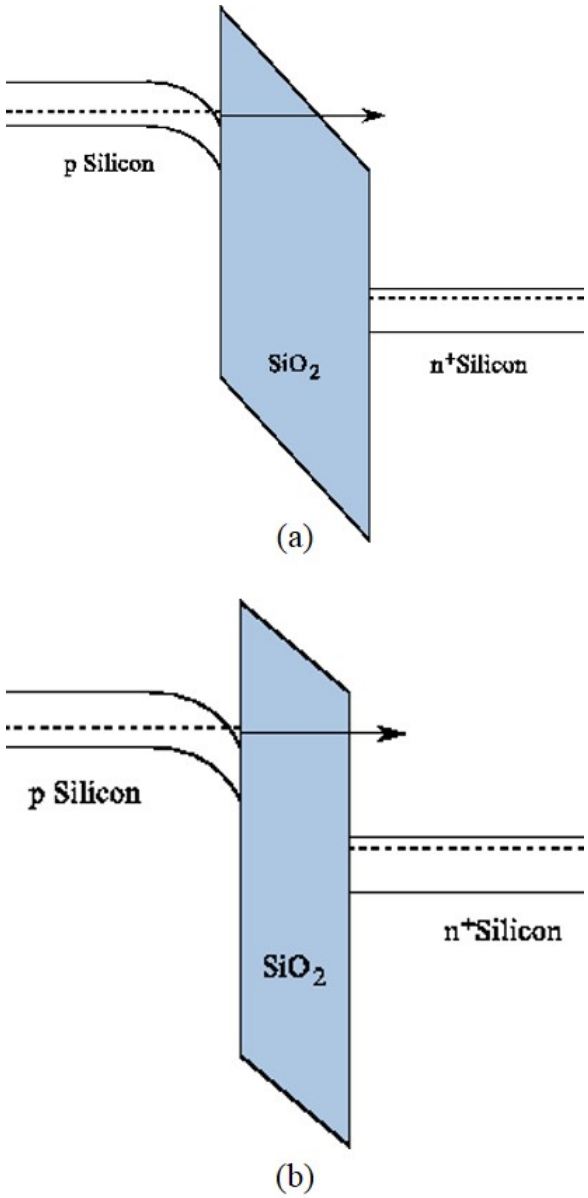

Figure 1.12: Tunneling mechanisms for different band structures. (a). Fowler-Nordheim tunneling mechanism, the electron tunnels through part of the barrier to the conduction band of the insulator; (b). Direct tunneling mechanism, the electron tunnel through the whole SiO_2 layer.

where $\mathcal{E}$ is external electric field, m^* is the effective mass in insulating layer. For thermal oxide layer, the constant $C_4 = 9.63 \times 10^{-7}$A/V^2, $C_5 = 2.77 \times 10^8$V/cm. Notice that the thickness of insulating layer, d_{ox}, plays no rule in Eq. 1.6.

On the other hand, direct tunneling occurs when the thickness of oxide is less than 5 nm. Electron from the inverted silicon surface can tunnel directly through the forbidden energy barrier formed by the dielectric layer to the heavy n-doped silicon side, as illustrated in Fig. 1.12(b). The tunneling current can be modelled by Tsu-Esaki formula [17]:

$$J = \frac{4\pi qm}{h^3} \int_{E_{min,0}}^{E_{max}} TC(E_x, m_{ox}^*) N(E_x) \mathrm{d}E_x \tag{1.7}$$

where the supply function is:

$$N(E_x) = \int_0^{\inf} \left[f_1(E) - f_2(E) \right] \mathrm{d}E_x \tag{1.8}$$

with f_1 and f_2 being energy distribution functions near the interfaces [18].

1.6 Chapter Organization

In the following chapters, we first discuss the general methods for semiconductor modeling, including optics models (TMM, Raytracing, FDTD) (Chapter 2). Then optics and device optimization of organic photovoltaic design is discussed in Chapter 3, followed by P3HT:PCBM′s phase separation and charge-carrier screening effect at nanogap (Chapter 4). In Chapter 5, silver nanoprisms are utilized to enhance the light absorption thus I-V performance due to surface plasmonic effect. Finally, the mechanism of diphenylgermane (DPG) and diphenylsilane (DPS) tunneling through the tip of atomic force microscopy (AFM) has been modeled and matched with experiments (Chapter 6). We then suggest the future work in Chapter 7 after conclusion.

Chapter 2

BACKGROUND AND NUMERIC METHODS

2.1 Optics Models

There are three major models for calculation of light absorption and energy conversion that occurs in solar cells. Transfer-matrix method (TMM) is easily to realize, but can only be used for stratified (layered) medium. Ray-tracing solves basic optical transmission and reflection problems by repeatedly advancing idealized narrow beams called rays through the medium by discrete amounts. It can treat complicated surface, but the dimension of object in calculation should be large compared to the incident light wavelength. Finite-difference time-domain (FDTD) method solves the fundamental Maxwells equations so it is able to treat any shape, material, and dimension, but is computationally expensive.

2.1.1 Ray-Tracing (RT) Method

Ray tracing is a method for calculating the path of light wave through a system with regions of varying reflection coefficients and geometric structures. Wavefronts can bend, reflect, and transmit through different regions in the system. The raytracer uses a recursive algorithm: It starts with a source ray and builds a binary tree that tracks the transmission and reflection of the ray. A reflection/transmission process occurs at interfaces with refractive index differences, as illustrated in Fig. 2.1 [19].

According to Fresnel equations, the reflection coefficients can be described as [20]:

$$\begin{cases} R_s = \left| \frac{n_1 cos\theta_i - n_2 cos\theta_t}{n_1 cos\theta_i + n_2 cos\theta_t} \right|^2 = \left| \frac{n_1 cos\theta_i - n_2 \sqrt{1 - \left(\frac{n_1}{n_2} sin\theta_i\right)^2}}{n_1 cos\theta_i + n_2 \sqrt{1 - \left(\frac{n_1}{n_2} sin\theta_i\right)^2}} \right|^2 \\ R_p = \left| \frac{n_1 cos\theta_t - n_2 cos\theta_i}{n_1 cos\theta_t + n_2 cos\theta_i} \right|^2 = \left| \frac{n_1 \sqrt{1 - \left(\frac{n_1}{n_2} sin\theta_i\right)^2} - n_2 cos\theta_i}{n_1 \sqrt{1 - \left(\frac{n_1}{n_2} sin\theta_i\right)^2} + n_2 cos\theta_i} \right|^2 \end{cases} \tag{2.1}$$

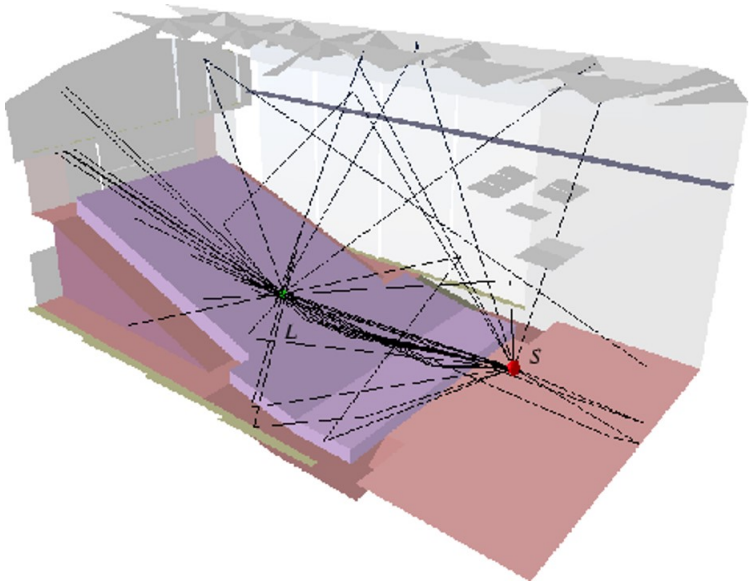

Figure 2.1: The direct sound and first- and second-order reflection paths in a concert hall obtained by a ray-tracing simulation. The source and the listener are denoted by S and L, respectively.

According to energy conversion, the transmission coefficients for s- and p-polarized light are: $\mathrm{T_s} = 1 - \mathrm{R_s}$ and $\mathrm{T_p} = 1 - \mathrm{R_p}$ respectively. So the overall reflection and transmission coefficients for unpolarized light are:

$$\begin{cases} R = \frac{R_s + R_p}{2} \\ T = \frac{T_s + T_p}{2} \end{cases} \tag{2.2}$$

If the refractive index is complex, the reflection and transmission coefficients are also complex. In such cases, only the absolute value is taken into account. The raytracer automatically computes the plane of incidence at each interface, decomposes the polarization vector into s- and p-polarization components, and applies the respective reflection and transmission coefficients to these s- and p-polarization components.

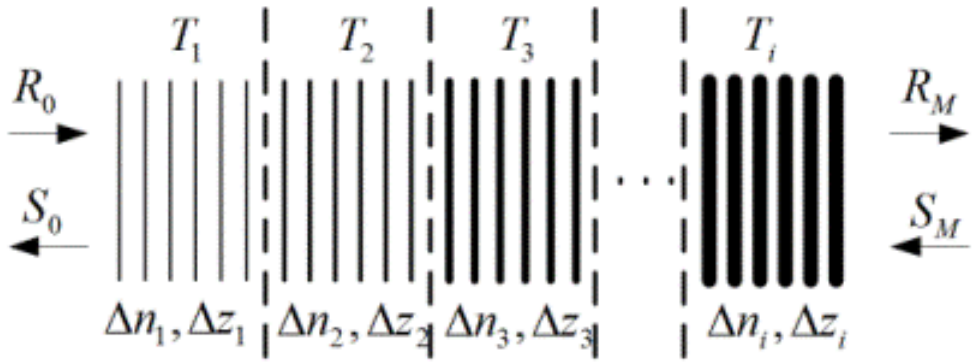

Figure 2.2: The direct sound and first- and second-order reflection paths in a concert hall obtained by a ray-tracing simulation. The source and the listener are denoted by S and L, respectively.

2.1.2 Transfer-Matrix Method (TMM)

Transfer-matrix method is used primarily to analyze the wave propagation through layered medium, as illustrated in Fig. 2.2 [21, Chapter 8]. According to Maxwells equations, the electric field, $\mathrm{E(z)} = \mathrm{E_r exp(ikz)} + \mathrm{E_l exp(-ikz)}$, and its first order derivative $\mathrm{F(z)} = \mathrm{ikE_r exp(ikz)} - \mathrm{ikE_l exp(-ikz)}$ across boundaries from one medium to the next can be expressed by simple continuity conditions:

$$\begin{pmatrix} E(z+L) \\ F(z+L) \end{pmatrix} = M \begin{pmatrix} E(z) \\ F(z) \end{pmatrix} \tag{2.3}$$

where

$$M = \begin{pmatrix} coskL & \frac{1}{k}sinkL \\ -ksinkL & coskL \end{pmatrix} \tag{2.4}$$

is the transfer matrix for light propagation over a thickness of L into the positive z direction, given k the wave number in the medium. For a system with N different layers, we can easily calculate the transfer matrix for the system by:

$$M_s = M_N \cdots M_2 \cdot M_1 \tag{2.5}$$

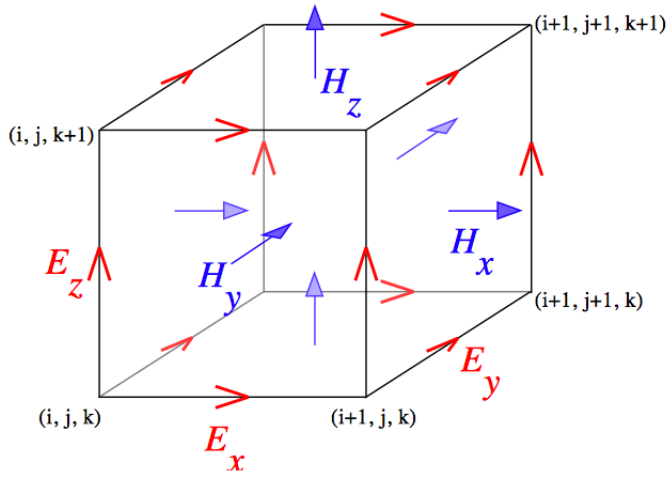

Figure 2.3: Illustration of a standard Cartesian Yee′s cell used for FDTD calculation. i+1, j+1, and k+1 represent the space evolution during FDTD simulation.

2.1.3 Finite-Difference Time-Domain (FDTD) Method

Finite-difference time-domain method discretizes the time-dependent Maxwell's equations using central-difference approximations to the space and time partial derivatives. At any point in space at any time, the updated value of E-field can be expressed as a function of E-field and curl of magnetic field: $\tilde{\mathrm{E}}(\mathrm{z},\mathrm{t}+\triangle\mathrm{t}) = \mathrm{f}(\tilde{\mathrm{E}}(\mathrm{z},\mathrm{t}), \nabla\times\tilde{\mathrm{H}}(\mathrm{z},\mathrm{t}), \mathrm{t}, \triangle\mathrm{t})$. It can deal with electromagnetic wave interactions with any kind of materials and structures as long as materials' permeability, permittivity, and conductivity are specified [22].

The Maxwell′s curl equations in linear, isotropic, non-dispersive materials are:

$$\begin{cases} \frac{\partial \mathbf{E}}{\partial t} = \frac{1}{\epsilon}\left(\nabla\times\mathbf{H} - \mathbf{J} - \sigma\mathbf{E}\right) \\ \frac{\partial \mathbf{H}}{\partial t} = -\frac{1}{\mu}\left(\nabla\times\mathbf{E} + \mathbf{M} + \sigma^{*}\mathbf{H}\right) \end{cases} \tag{2.6}$$

where $\mathbf{E}$ is the vectorial electric field, $\mathbf{H}$ is the vectorial magnetic field, $\mathbf{J}$ is the electric current density, $\mathbf{M}$ is the magnetic current density, ϵ is the electrical permittivity, μ is the magnetic permeability, σ is the electric conductivity, σ^{*} is the magnetic conductivity. In terms of x-, y-, and z-components, the curl equations can be decomposed into a system of

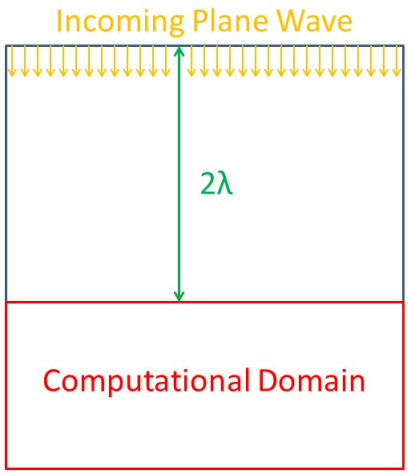

Figure 2.4: Illustration of the distance between incoming plane wave and computational domain. Visualized as a cubic voxel, the electric field components form the edges of the cube, and the magnetic field components form the normals to the faces of the cube. A three-dimensional space lattice consists of a multiplicity of such Yee′s cells. An electromagnetic wave interaction structure is mapped into the space lattice by assigning appropriate values of permittivity to each electric field component, and permeability to each magnetic field component.

six coupled scalar equations:

$$\begin{cases} \frac{\partial E_x}{\partial t} = \frac{1}{\epsilon}\left[\frac{\partial H_z}{\partial y} - \frac{\partial H_y}{\partial z} - (J_x + \sigma E_x)\right] \\ \frac{\partial E_y}{\partial t} = \frac{1}{\epsilon}\left[\frac{\partial H_x}{\partial z} - \frac{\partial H_z}{\partial x} - (J_y + \sigma E_y)\right] \\ \frac{\partial E_z}{\partial t} = \frac{1}{\epsilon}\left[\frac{\partial H_y}{\partial x} - \frac{\partial H_x}{\partial y} - (J_z + \sigma E_z)\right] \\ \frac{\partial H_x}{\partial t} = \frac{1}{\mu}\left[\frac{\partial E_y}{\partial z} - \frac{\partial E_z}{\partial y} - (M_x + \sigma^* H_x)\right] \\ \frac{\partial H_y}{\partial t} = \frac{1}{\mu}\left[\frac{\partial E_z}{\partial x} - \frac{\partial E_x}{\partial z} - (M_y + \sigma^* H_y)\right] \\ \frac{\partial H_z}{\partial t} = \frac{1}{\mu}\left[\frac{\partial E_x}{\partial y} - \frac{\partial E_y}{\partial x} - (M_z + \sigma^* H_z)\right] \end{cases} \tag{2.7}$$

as illustrated as Yee′s cell in Fig. 2.3.

The advantage of FDTD method is that the computational domain is exactly the same as the physical domain, with materials defined via their permittivity, conductivity, and permeability values. Usually, the incoming light source is plane wave, which is placed at a distance of at least two wavelengths away from the simulating system, as illustrated in Fig. 2.4.

2.1.4 Comparison of Optics Solvers

Fig. 2.5 illustrates the comparison of the optical charge carrier generation rate for a typical single-crystalline silicon-based solar cell (thickness of silicon absorbing layer is 1 μm, covered by 100 nm ITO as anode layer to collect holes, and 100 nm aluminum layer as cathode to collect electrons) calculated by three optics solvers discussed above (FDTD, TMM, and Ray-Tracing methods). Comparing between Fig. 2.5(a)-(c), it is obvious that the peak values of optical charge carrier generation rate calculated by all three solvers are the same. However, Fig. 2.5 does not show the interference nature of light with a period of $\approx$ 67 nm, compared to Fig. 2.5(a) and (b). This is consistent with the fact that Ray-Tracing method considers incoming light as rays rather than waves, thus neglecting any information of phases.

Table 2.1: Comparison of Calculation Speed of Three Optics Solvers

Method	TMM	RT	FDTD
Time [min]	5	7	180

Table 2.1 compares the calculation speed between three optics solvers for the same silicon-based solar cells. We use a workstation with 8 CPUs of Intel(R) Core(TM) i7-3770 CPU @ 3.40GHz and 32 GB memory, and run 2-D simulation (with extension in the 3$^{\text{rd}}$ dimension to be 1 μm) using Sentaurus Electromagnetic Wave Solver and Sentaurus Device simulator (Synopsys®). It is quite obvious that calculation using Finite-Difference Time-Domain (FDTD) method takes $>$ 30 times more computational resources to finish the same job, compared to Transfer-Matrix (TMM) and Ray-Tracing (RT) methods. As a result,

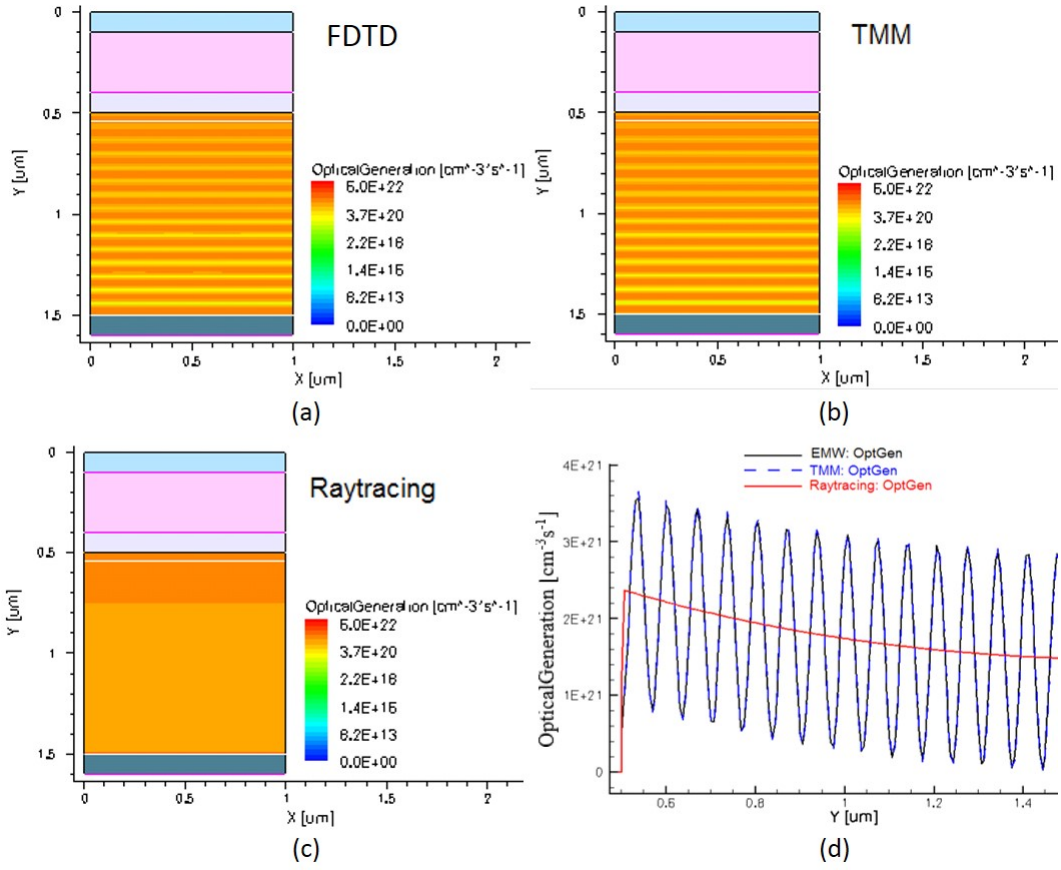

Figure 2.5: Comparison of the optical charge carrier generation rate calculated by three optics solvers. (a). by Finite-Difference Time-Domain (FDTD) method; (b). by Transfer-Matrix Method (TMM); (c). by Ray-Tracing (RT) method; (d). Comparison of the optical charge carrier generate rate for a typical silicon-based solar cell, the thickness of silicon is 1 μm, with 100 nm of ITO on top as anode layer and 100 nm of aluminum as cathode layer.

FDTD algorithm is suggested to use only in cases of complex geometry with dimensions on the order of/ smaller than the incoming wavelength where TMM and RT methods fail.

2.2 Device Models

The popular drift-diffusion model can be derived directly from Boltzmann's transport equation by the method of moments [23] or from the basic principles of irreversible thermodynamics [24]. For a simple drift-diffusion model at constant temperature, it contains ten equations:

2.2.1 Drift-Diffusion Model for Inorganic Materials

1. Charge density equation:

$$\rho = q\left(p - n + N_d^+ - N_a^-\right) \tag{2.8}$$

where n and p are electron/hole density, N_d^+ and N_a^- are ionized donor/acceptor density.

2. Poisson equation:

$$\begin{cases} \nabla \cdot \mathbf{E} = \frac{\rho}{\epsilon} \\ \nabla\varphi = -\mathbf{E} \\ \nabla E_i = q\mathbf{E} \end{cases} \tag{2.9}$$

where $\mathbf{E}$ is electric field, φ is electrostatic potential, ϵ is material's permittivity, and E_i is the intrinsic energy.

3. Carrier density equations:

$$\begin{cases} n = n_i exp\left(\frac{F_n - E_i}{k_B T}\right) \\ p = n_i exp\left(\frac{E_i - F_p}{k_B T}\right) \end{cases} \tag{2.10}$$

where F_n and F_p are electron/hole quasi-Fermi energies.

4. Drift and diffusion current equations:

$$\begin{cases} \mathbf{J}_n = q\left(n\mu_n\mathbf{E} + D_n\nabla n\right) \\ \mathbf{J}_p = q\left(p\mu_p\mathbf{E} - D_p\nabla p\right) \end{cases} \tag{2.11}$$

where μ_{n} and μ_{p} are electron/hole mobility, and $\mathrm{D_n}$ and $\mathrm{D_p}$ are electron/hole diffusivity.

5. Continuity equation with recombination:

$$\begin{cases} \nabla\cdot\mathbf{J}_n = q\left(R_{net} - R_{bimolec}\right) + q\frac{\partial n}{\partial t} \\ -\nabla\cdot\mathbf{J}_p = q\left(R_{net} - R_{bimolec}\right) + q\frac{\partial p}{\partial t} \end{cases} \tag{2.12}$$

where the Shockley-Read-Hall recombination rate is:

$$R_{net} = \frac{np - ni^2}{n + p + 2n_i cosh\left(\frac{E_f - E_i}{k_B T}\right)} \tag{2.13}$$

and the singlet exciton generation rate in Langevin form reads:

$$R_{bimolec} = \frac{q}{\epsilon_0\epsilon_r}\left(\mu_n + \mu_p\right)\left(np - n_{i,eff}^2\frac{n_{se}}{n_{se}^{eq}}\right) \tag{2.14}$$

2.2.2 Singlet Exciton Equation for Organic Materials

For organic light-absorbing materials such as P3HT:PCBM, since the refractive index is very low ($\approx$ 1.6-2.15 for various wavelength as shown in Fig. 2.6 [25]), the binding energy between electron/hole pairs generated by photon absorption is strong enough to form excitons. Thus, besides solving the Poisson and continuity equations, the singlet exciton equation is introduced to account for optical properties of polymer materials related to Frenkel excitons, in which triplet excitons dont contribute directly to light emission:

$$\frac{\partial n_{se}}{\partial t} = R_{bimolec} + D_{se}\nabla^2 n_{se} - \frac{n_{se} - n_{se}^{eq}}{\tau} - R_{se} \tag{2.15}$$

where $\mathrm{n_{se}}$ is the density of singlet excitons, $\mathrm{D_{se}}$ is the diffusivity of singlet excitons, $\mathrm{R_{bimolec}}$ is the carrier bimolecular recombination rate acting as a singlet excitons generation, τ is singlet exciton lifetime, and $\mathrm{R_{se}}$ is the net singlet exciton recombination rate term. The

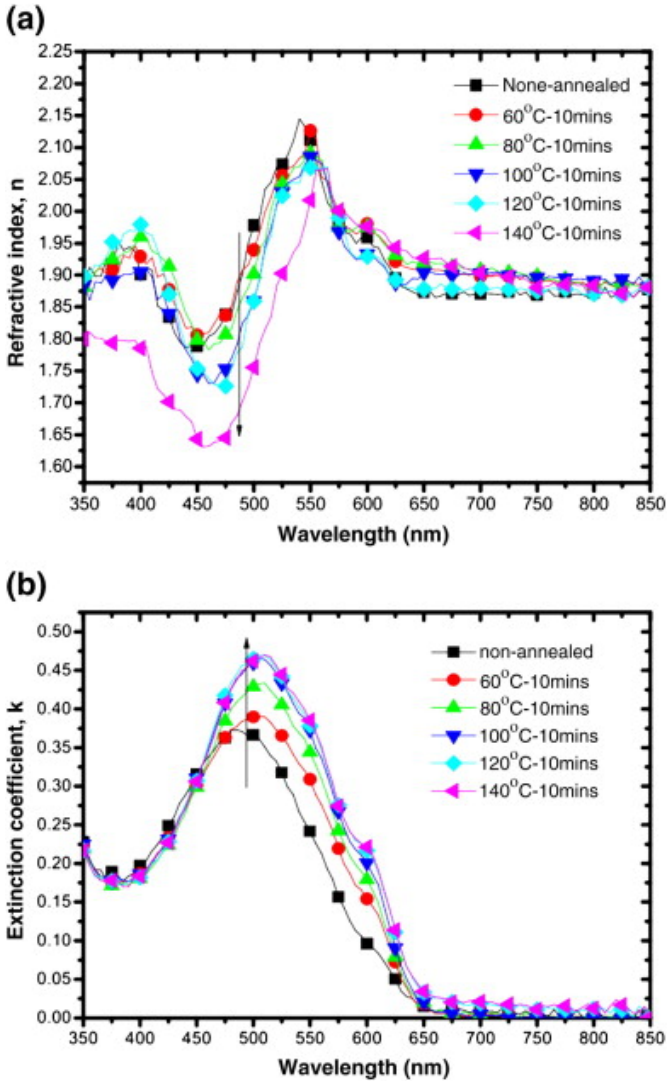

Figure 2.6: The (a) refractive index and (b) extinction coefficient of P3HT:PCBM annealed at various temperatures obtained from spectrometric ellipsometry measurement.

equation models the dynamics of the generation, diffusion, recombination, and radiative decay of singlet excitons in organic semiconductors.

2.3 Numerical Techniques

2.3.1 Fast Fourier Transform (FFT)

FFT method is an integral transform defined over the entire domain x $\in (-\infty, \infty)$. It is an efficient algorithm to compute the discrete Fourier transform (DFT) and its inverse. Let $\mathrm{X}_0, \cdots, \mathrm{X}_{\mathrm{N}-1}$ be complex numbers, the DFT is defined by the formula:

$$X_k = \sum_{n=0}^{N-1} x_n e^{-i2\pi \overrightarrow{k} \cdot \left(\frac{\overrightarrow{n}}{N}\right)} \tag{2.16}$$

where $\overrightarrow{k} = (\mathrm{k}_1, \cdots \mathrm{k}_{\mathrm{dim}})$, and $\overrightarrow{n} = (\mathrm{n}_1, \cdots \mathrm{n}_{\mathrm{dim}})$ represent the multidimensional case.

Evaluating this definition directly requires $\mathrm{O}(\mathrm{n}^2)$ operations. An FFT calculation, however, computes the same results in O(nlogn) operations. However, the FFT calculation can only deal with system having periodic boundary conditions. This is not the actual case experimentally since the surface energy of P3HT/air and PCBM/substrate is different.

2.3.2 Finite-Element Method (FEM)

Finite element method is a numerical technique for finding approximate solutions of partial differential equations as well as of integral equations. It is a good choice for solving partial differential equations over complicated domains which change with time. One example is the simulation of the tip of atomic force microscopy (AFM), as illustrated in Fig. 2.7.

However, standard FEM is very time-consuming. It requires $\mathrm{O}(\mathrm{n}^3)$ operations to get the same result as FFT. In order to accelerate the calculation, we split the non-zero pivot calculation matrix A into a lower triangular matrix L and an upper triangular matrix U, which is called LU-decomposition:

$$A = LU \Rightarrow \begin{pmatrix} a_{11} & a_{12} & a_{13} \\ a_{21} & a_{22} & a_{23} \\ a_{31} & a_{32} & a_{33} \end{pmatrix} = \begin{pmatrix} 1 & 0 & 0 \\ m_{21} & 1 & 0 \\ m_{31} & m_{32} & 1 \end{pmatrix} \begin{pmatrix} u_{11} & u_{12} & u_{13} \\ 0 & u_{22} & u_{23} \\ 0 & 0 & u_{33} \end{pmatrix} \tag{2.17}$$

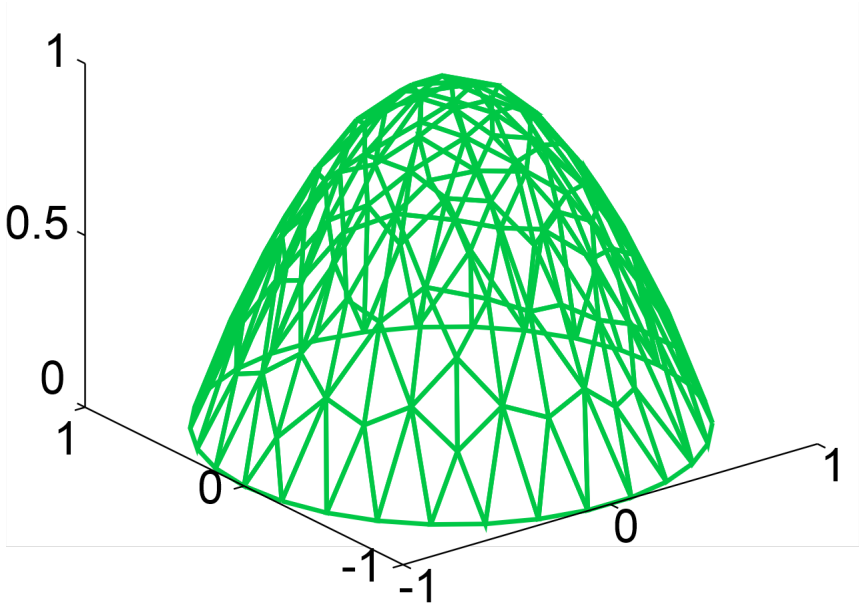

Figure 2.7: The finite-element meshing of the tip of atomic force microscopy.

2.4 Summary

In this chapter, we review the common numerical methods for modeling semiconductor devices. For optics simulation, ray-tracing (RT), transfer-matrix method (TMM), and finite-difference time-domain (FDTD) method are the three major techniques, among which, and TMM and FDTD methods take into account the plasmonic effect. From the device simulation perspective, Poisson equation, together with charge carrier continuity equations are the foundation of modeling silicon-based semiconductor devices. We need to include the singlet exciton generation and dissociation equation to account for the excitons in organic semiconductor materials.

Chapter 3

OPTICS AND DEVICE ENGINEERING FOR ORGANIC PHOTOVOLTAICS

3.1 Overview

Organic semiconductors have attracted a lot of attention due to the flexibility and low weight, as well as ultra-low cost production compared to silicon-based solar cells [26, 27]. Many efforts have been made in order to improve the efficiency of organic solar cells by developing new materials with smaller bandgap [28], modifying the thickness of active layer [29], as well as using charge-collecting materials with higher conductivity [30, 31]. In this work, we describe efforts at coupled optical and electrical modeling with the aim of optimizing material choices and device structures for maximum performance. The optical processes inside organic solar cells include electromagnetic transmission, reflection, and absorption in multilayer structures. We explore the optimized active layer thickness and choices of using ultra-thin metals to replace ITO as transparent anode layer, with the aim of coupling light strongly into P3HT:PCBM layer while simultaneously reducing cost. From the electrical device point of view, we have derived a simple formula for dependence of required contact sheet resistance on the width and spacing of interdigitated anode contact metal. We use Sentaurus Device simulator (Synopsys®), adapted with material-specific models for electronic polymers, to explore impact of illumination and material properties on device behavior. Finally, the coupling of optical and electrical simulation helps us to find the trade-off solutions to device geometry. These properties are then used as the basis of computational exploration of device structure and materials to optimize solar cell performance[1].

---

[1]This chapter is adapted from a paper published in *Mater. Res. Soc. Symp. Proc.* [32].

3.2 Optimization of P3HT:PCBM Thickness

Fig. 3.1(a) shows the optical generation under stack structure, with materials being gas on top, glass as substrate, ultra-thin silver or 100 nm ITO as transparent anode layer, 50 nm PEDOT:PSS, P3HT:PCBM polymer as active layer and 100 nm aluminum as back metal layer.

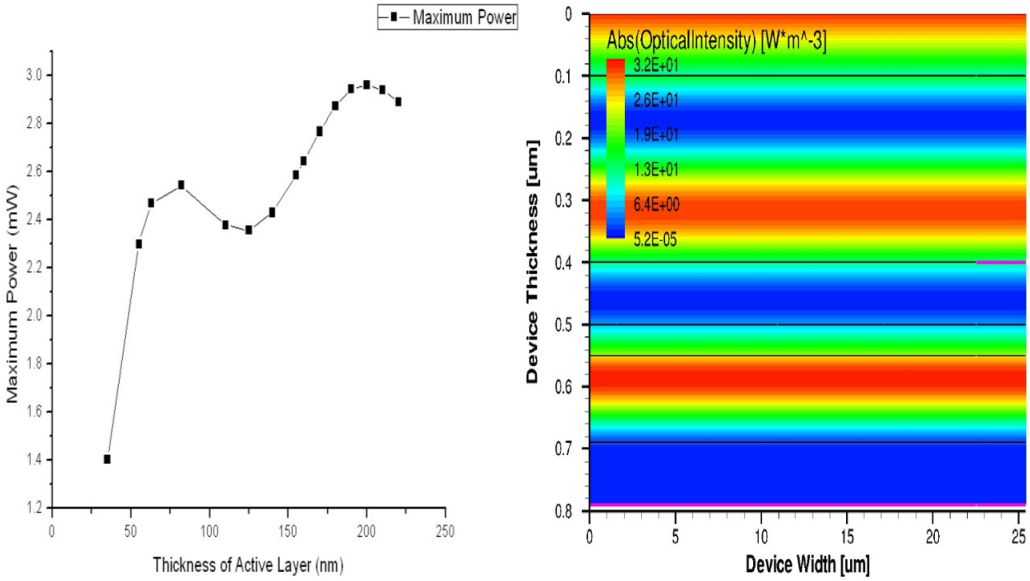

Figure 3.1: (a). Maximum power vs. P3HT:PCBM layer thickness; (b). Optical intensity under optimized P3HT:PCBM layer thickness

Here we assume normal incidence of sunlight with wavelength distribution following standard AM1.5G spectrum, energy bandgap of P3HT/PCBM being 1.5 eV [33], exciton diffusion length being ≈10 nm [34, 35], exciton binding energy being 0.3 eV, and exciton lifetime being 100 ps [36]. From optical absorption point of view, the thicker the active layer is, the larger portion of incident light is absorbed. However, from the exciton recombination perspective, thicker active layer will cause larger portion of excitons and/or dissociated electrons and holes to recombine prior to collection by electrodes. Thus there is a trade-off in the active layer thickness. Fig. 3.1(b) shows solar cell performance as a function of active layer thickness given a fixed value of trap states. Together with Fig. 3.1(a), the best device

performance corresponds to active layer thickness equaling 200 nm, in which there are two peaks of optical generation.

3.3 Choice of Ultra-Thin Anode Materials

The reflectivity and transmissivity equations for a plane parallel, absorbing film situated between two dielectric media can be expressed as [20]:

$$\begin{cases} R = \frac{\rho_{12}^2 exp(2k_2\eta)+\rho_{23}^2 exp(-2k_2\eta)+2\rho_{12}\rho_{23}cos(\varphi_{23}-\varphi_{12}+2n_2\eta)}{exp(2k_2\eta)+\rho_{12}^2\rho_{23}^2 exp(-2k_2\eta)+2\rho_{12}\rho_{23}cos(\varphi_{23}+\varphi_{12}+2n_2\eta)} \\ T = \frac{n_3}{n_1}\frac{\tau_{12}^2\tau_{23}^2}{exp(2k_2\eta)+\rho_{12}^2\rho_{23}^2 exp(-2k_2\eta)+2\rho_{12}\rho_{23}cos(\varphi_{23}+\varphi_{12}+2n_2\eta)} \end{cases} \tag{3.1}$$

where these parameters are in the form of:

$$\begin{cases} \rho_{12}^2 = \frac{(n_1-n_2)^2+k_2^2}{(n_1+n_2)^2+k_2^2}, & \rho_{23}^2 = \frac{(n_3-n_2)^2+k_2^2}{(n_3+n_2)^2+k_2^2} \\ \varphi_{12} = tan^{-1}\left(\frac{2n_1k_2}{n_2^2+k_2^2-n_1^2}\right), & \varphi_{23} = tan^{-1}\left(\frac{2n_3k_2}{n_2^2+k_2^2-n_3^2}\right) \\ \tau_{12}^2 = \frac{4n_1^2}{(n_1+n_2)^2+k_2^2}, & \tau_{23}^2 = \frac{4(n_2^2+k_2^2)}{(n_3+n_2)^2+k_2^2} \end{cases} \tag{3.2}$$

with $(\mathrm{n_i}, \mathrm{k_i})$ being refractive index and attenuation index of material i, and $\mathrm{h} = (\lambda_0/2\pi)\eta$ being the thickness of metal layer.

In order to estimate the value of resistivity for ultra-thin metal layer, the reduction of electron mean-free-path (MFP) from that of bulk metals must be considered. Since the thickness of metal film (and thus also generally the grain size) is on the scale of tens of nanometers, the impact of excess scattering is very important. Since $\rho = \rho_{\mathrm{bulk}} + \rho_{\mathrm{surface}}$ with $1/\rho_{\mathrm{bulk}} = \mathrm{A}_1 \cdot \mathrm{MFP}$ and $1/\rho_{\mathrm{surface}} = \mathrm{A}_2 \cdot \mathrm{MFP}$ where we assume $\mathrm{A}_1 = \beta \mathrm{A}_2$, we get:

$$\rho = \rho_{bulk} \cdot \left(1 + \beta \frac{MFP}{thickness}\right) \tag{3.3}$$

Table 3.1 shows the basic parameters of several metals as bulk material. Comparing the experimental data that $\rho_{\square,\mathrm{silver}} = 20\Omega/\square$ for silver thickness equals 10 nm [37], we get $\beta \approx 2$. Eq. 3.3 illustrates that the resistivity increases dramatically as the thickness goes below the mean-free-path (MFP). Clearly from the resistivity point of view, thick metal films can transport carriers more efficiently. For the transmission perspective, however,

Table 3.1: Optical properties of bulk metals for wavelength of 550 nm

Metal	n	k	MFP [nm]	Resistivity [$\Omega \cdot$ nm]
Silver	0.2	3.44	52	15.9
Gold	0.47	2.83	39	22.1
Copper	0.62	2.57	38	16.8
aluminum	1.44	5.23	14.9	26.5
ITO	1.92	0.048	27	1500

thinner metal films are more transparent, and thus block less light. From Fig. 3.2, for those metals for which mean free path is large, 5 nm thickness gives 85% transmission and very good conductivity at the same time. However, for metals with small value of mean free path, such as aluminum, even 3 nm thickness will cause 20% reflection/absorption. Thus, for subsequent analyses, we use silver as the transparent anode material, and aluminum as the cathode material.

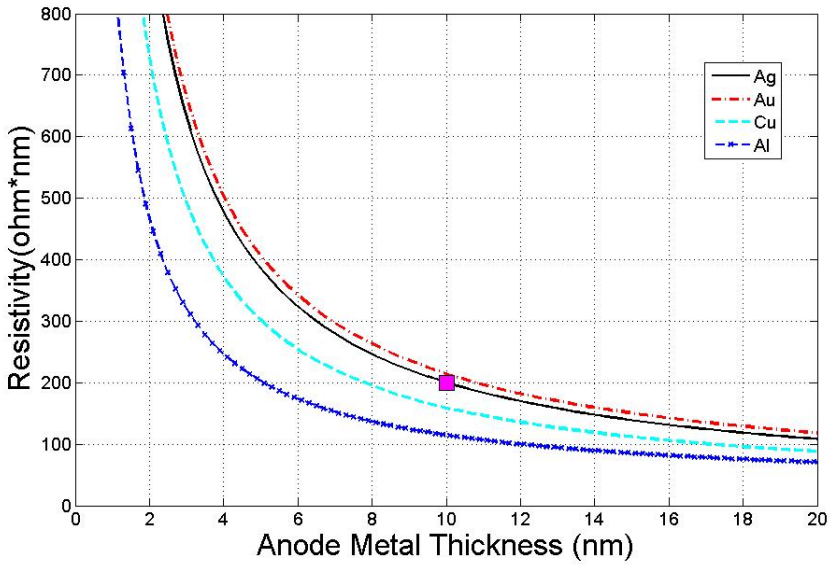

Figure 3.2: Electrical resistivity vs. Metal film thickness

PEDOT:PSS and ITO serve as transparent anode layer to collect dissociated holes generated from light absorption in P3HT:PCBM due to its limited conductivity. However, since ITO is usually expensive and brittle, from the cost-effective point of view, researchers are looking for its replacement. One natural choice would be ultra-thin metal layer because of its high transmissivity and conductivity. Fig. 3.3 illustrates the relationship between ultra-thin metal transmissivity with its conductivity. It is clear that most metals with high conductivity out-perform ITO, if using Eq. 3.1-3.3.

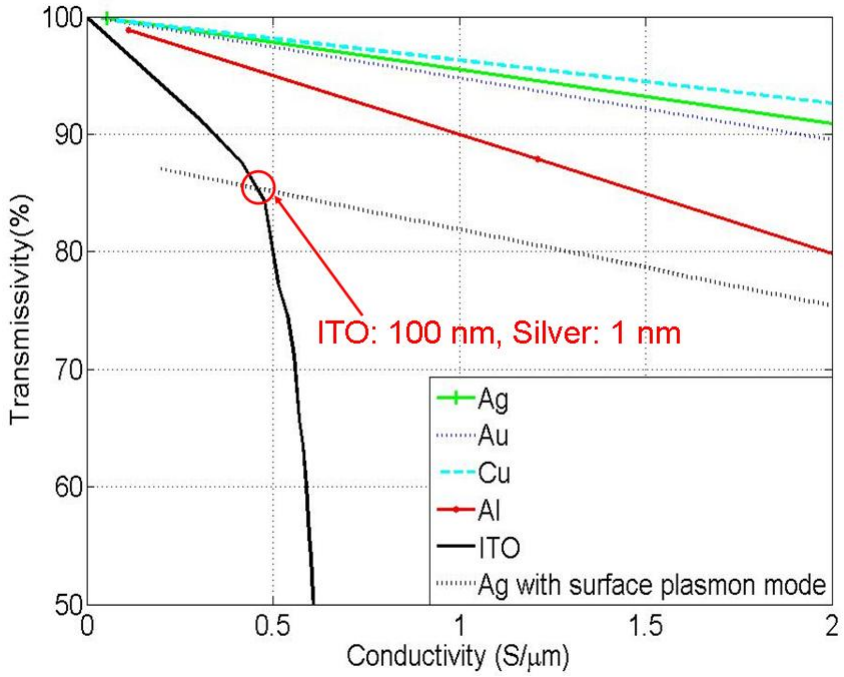

Figure 3.3: Transmissivity through vs. conductivity of ultra-thin anode layer. The intersection point indicates that 100 nm ITO is equivalent to 1 nm ultra-thin silver as transparent anode layer.

3.4 Critical Spacing of Anode

From the electronic device perspective, the conductivity of transparent anode layer affects the carrier transport rates dramatically [38]. Consider a device which contains anode contact

(with the length of a) and total width of L (as illustrated in Fig. 3.4), for small forward bias, the voltage drop across the device can be expressed as:

$$I_{lat}(y) = \int_0^y I_{ph} \mathrm{d}y' = y \cdot I_{ph} \tag{3.4}$$

so that:

$$\triangle V(y) = -\int_{\frac{L-a}{2}}^{y} I_{lat}(y') \rho \mathrm{d}y' = \frac{\rho I_{ph}}{2} \left[\left(\frac{L-a}{2} \right)^2 - y^2 \right] \tag{3.5}$$

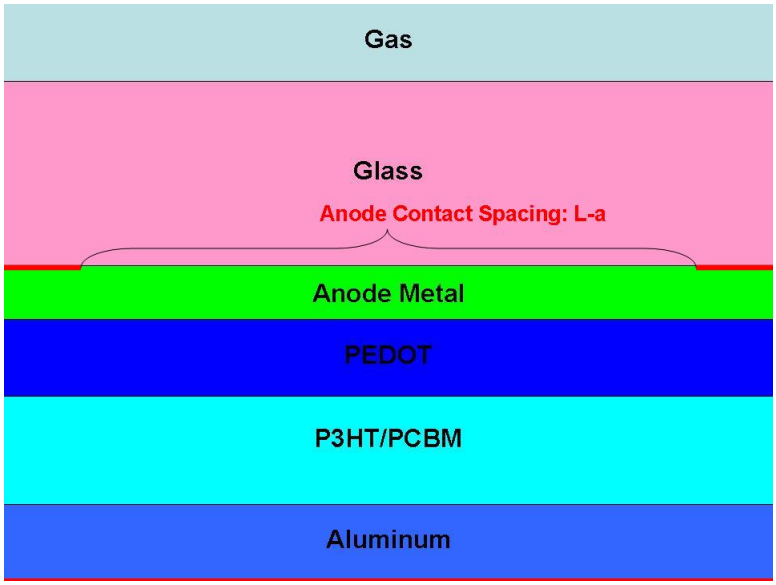

Figure 3.4: Stack structure of organic photovoltaic device with anode grid.

Since we want the voltage drop across the device to be no larger than thermal voltage for minimal degradation, we get the criteria for device performance:

$$\triangle V_{max} \leq \frac{k_B T}{q} \Rightarrow \frac{\rho I_{ph}}{8} (L-a)^2 \leq \frac{k_B T}{q} \tag{3.6}$$

Considering the fact that $\rho_{\square,\mathrm{metal}} \ll \rho_{\square,\mathrm{PEDOT}}$, we finally derived the maximal distance between neighboring anodes:

$$L = 2\sqrt{\frac{2k_B T}{q} \frac{1}{\rho I_{ph}}} \approx 2\sqrt{\frac{2k_B T}{q} \frac{1}{\rho_{\square,metal} I_{ph}}} \tag{3.7}$$

Fig. 3.5(a) illustrates the device performance dependence on the anode layer resistivity, with the anode grid structure illustrated in Fig. 3.4. For 5 nm thick anode layer with 5 μm contact width and 50 μm device width, the critical resistivity calculated by Eq. 3.7 is $\rho_{\text{critical}} = 0.51\Omega \cdot \text{cm}$. As a comparison, we increase/decrease it by several times to show its impact on the I-V curves. It is clear that the device performance stays almost the same if the anode resistivity is lower than critical resistivity. However, both the maximum power and fill-factor decrease dramatically if the anode resistivity is higher than critical one. This shows that Eq. 3.7 serves as reasonable criteria for designing anode contact pattern.

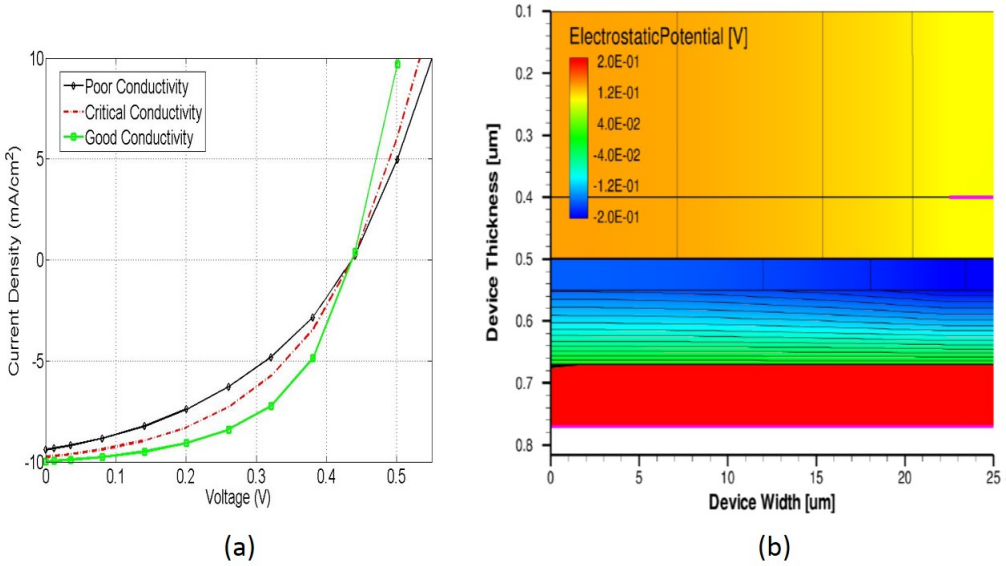

Figure 3.5: (a). Current-voltage (I-V) curves for organic solar cells with different anode metal resistivity; (b). Electrostatic potential degradation around anode due to large resistivity of PEDOT:PSS.

Fig. 3.5(b) illustrates the electrostatic potential degradation around the anode due to the large resistivity of PEDOT:PSS. The anode width for a typical photovoltaic device is $a = 5\mu$m. From Eq. 3.7, by setting $\text{I}_{\text{ph}} = 10\text{mA/cm}^2$ for a standard organic solar cell, we get the critical spacing between neighboring anode metal grids, which is shown in Table 3.2. For a silver anode layer with thickness equal to 5 nm, the critical anode spacing is 5400 μm. If we want the anode spacing to be larger than 100 μm and anode thickness to

be 50 nm, the sheet resistance required for transparent polymers should be no larger than $2.3 \times 10^5 \Omega/\square$, which is much larger than the sheet resistance of ITO, but smaller than that of PEDOT-PH500.

Table 3.2: Metal thickness vs. critical anode spacing in anode layer

Material	Thickness [nm]	Critical anode spacing [μm]
Silver	5	5400
Gold	5	5300
Copper	5	6100
PEDOT-PH500	36	25
ITO	50	8300
Polymer with $\rho = 1\Omega \cdot \text{cm}$	50	100

3.5 Designing of Grating Structure in Cathode Layer

Grating design at the cathode backcontact exhibits enhancement of light absorption in the P3HT:PCBM layer compared to the bare device. In Fig. 3.6, we investigate how much enhancement can be achieved by utilizing the nano-grating structure. Fig. 3.6(a) shows the field profiles generated in the bare (non-metallic) architecture under TM-polarized illumination. The field intensity in the volume of the active material is slightly higher compared to other layers. Fig. 3.6(b) presents the electric field map of the nano-grating architecture under TM-polarized AM1.5G solar radiation. It is clear that the peak optical carrier generation rate increases by a factor of 10 at the presence of cathode gratings. The peak and overall enhancement is listed in Table 3.3.

Fig. 3.7 compares the light absorption enhancement under different grating periods at λ = 630 nm. It is clear that increasing the incident angle enhances the optical charge carrier generation rate, due to the fact that the effective light travel length in P3HT:PCBM active layer is increased by a factor of $1/\cos(\theta)$. Moreover, the common enhancement peak at $P_{grating}$=300 nm indicates the optimized grating structure.

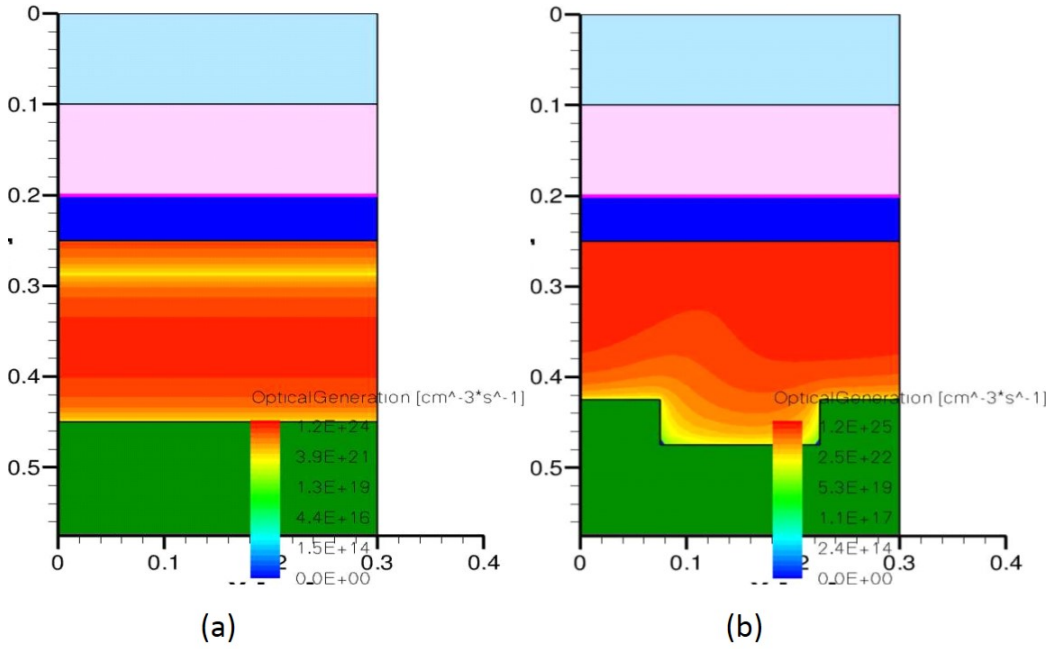

Figure 3.6: Grating structure added to cathode. Metal back reflector with grating structure can enhance light absorption by coupling light into plane of active device area.

Table 3.3: Optical Charge Carrier Generation in Organic Photovoltaic Device with Bare vs. Nanograted Cathode Layer

Cathode Type	Peak Generation Rate $[cm^{-3}s^{-1}]$	Enhancement	Integrated Generation $[s^{-1}]$	Enhancement
Bare	1.2×10^{24}	–	2.4×10^{11}	–
Nano-Grating	1.2×10^{25}	10	2.9×10^{11}	21%

3.6 Device Simulation - Impact from Trap States Density

To further increase energy conversion efficiency of organic solar cell, charge carriers generated by light absorption need to be collected by the electrodes more efficiently. To achieve this, the carrier recombination lifetime (τ) and mobility (μ) of P3HT:PCBM must be maximized [39]. Deep energetic traps in the distribution of electron and hole states will not only

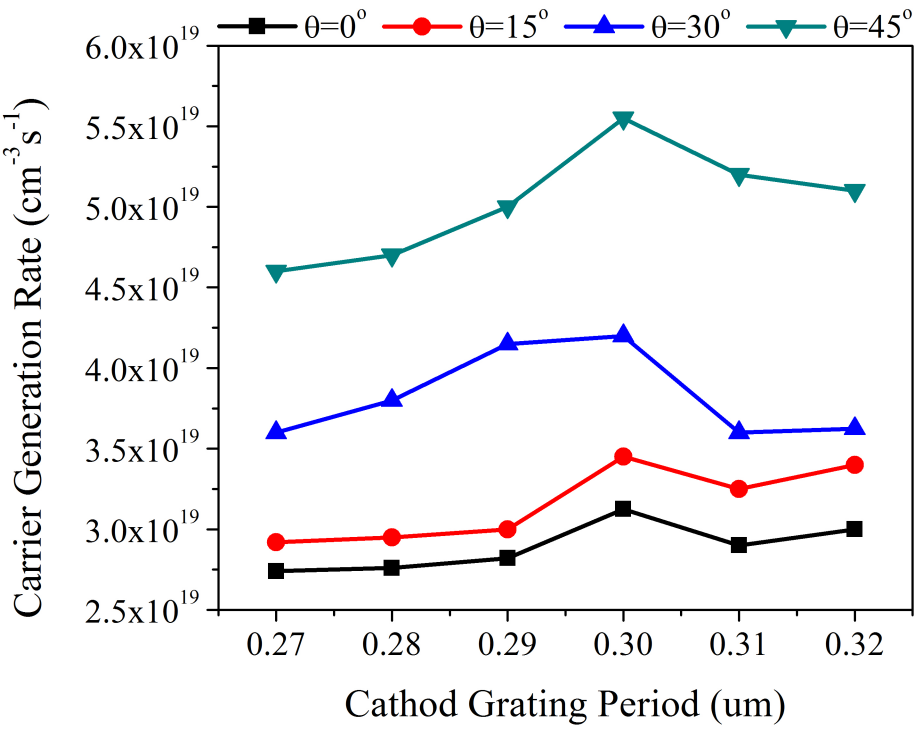

Figure 3.7: Light absorption enhancement in presence of cathode grating structure as a function of grating period. Can optimize period of grating to enhance absorption in shoulder of absorption spectrum. Carrier generation for illumination by solar spectrum shows optimum period near 300nm which increases absorption for wavelengths near 630nm.

reduce the mobility [40, 41, 42, 43, 44], but also cause charge recombination in organic photovoltaic devices [45, 46, 47, 48, 49]. Thus, understanding the role of trap states is the key in improving the performance of OPV. We conduct 2-D device simulation using Sentaurus Device Simulator, the materials' parameters are listed in Table 3.4.

Fig. 3.8 illustrates the impact of trap states density on the performance of organic solar cell. It is clear that higher density of trap states corresponds to less optimized thickness of P3HT:PCBM layer thickness, thus decreasing the maximum power density. However, maximum power density does not change dramatically when the density of states is below 10^{13}cm^{-3}.

Table 3.4: Device Simulation Parameters for Investigating the Impact from Trap States Density

Parameter Name	Parameter Symbol	Parameter Value
ITO thickness	t_{ITO}	100 nm
PEDOT:PSS thickness	t_{PEDOT}	50 nm
P3HT:PCBM active layer thickness	t_{active}	40 - 240 nm
aluminum back-reflector thickness	t_{back}	100 nm
P3HT:PCBM electron affinity	χ	3.9 eV
P3HT:PCBM bandgap	E_g	5.1 eV
P3HT:PCBM relative permittivity	ϵ_r	3.8
P3HT:PCBM effective electron trap density	N_e^{trap}	10^{12} - 10^{17} [cm^{-3}]
P3HT:PCBM effective hole trap density	N_h^{trap}	10^{12} - 10^{17} [cm^{-3}]
P3HT:PCBM electron mobility	μ_e	3×10^{-5} [$cm^2/(V \cdot s)$]
P3HT:PCBM hole mobility	μ_h	1×10^{-6} [$cm^2/(V \cdot s)$]

As another comparison, we use 100 nm ITO and different thickness of silver with electrical parameters calculated by Eq. 3.5 as the transparent anode layer. From the device simulation results in Fig. 3.9(a), thinner silver layer gives better device performance, but only when the thickness reduces to less than 5 nm can we get the device performance to be equivalent to 100 nm ITO, which is consistent with the results in Fig. 3.3. The reason is that Eq. 3.1 is valid only under the assumption that materials in both sides are infinitely thick dielectric materials ($h_1 \to \infty, h_3 \to \infty, k_1 = k_3 = 0$). In solar cells, however, PEDOT has finite thickness and absorption coefficient. Also when the thickness of metal layer goes to nanometer range, the surface-plasmon effect is dramatic, which increases the absorption in the lossy metal layer. By turning on the surface plasmon mode, we get the reduced optical transmissivity shown in Fig. 5 (b), confirming that only 3 nm silver layer is equivalent to 100 nm ITO.

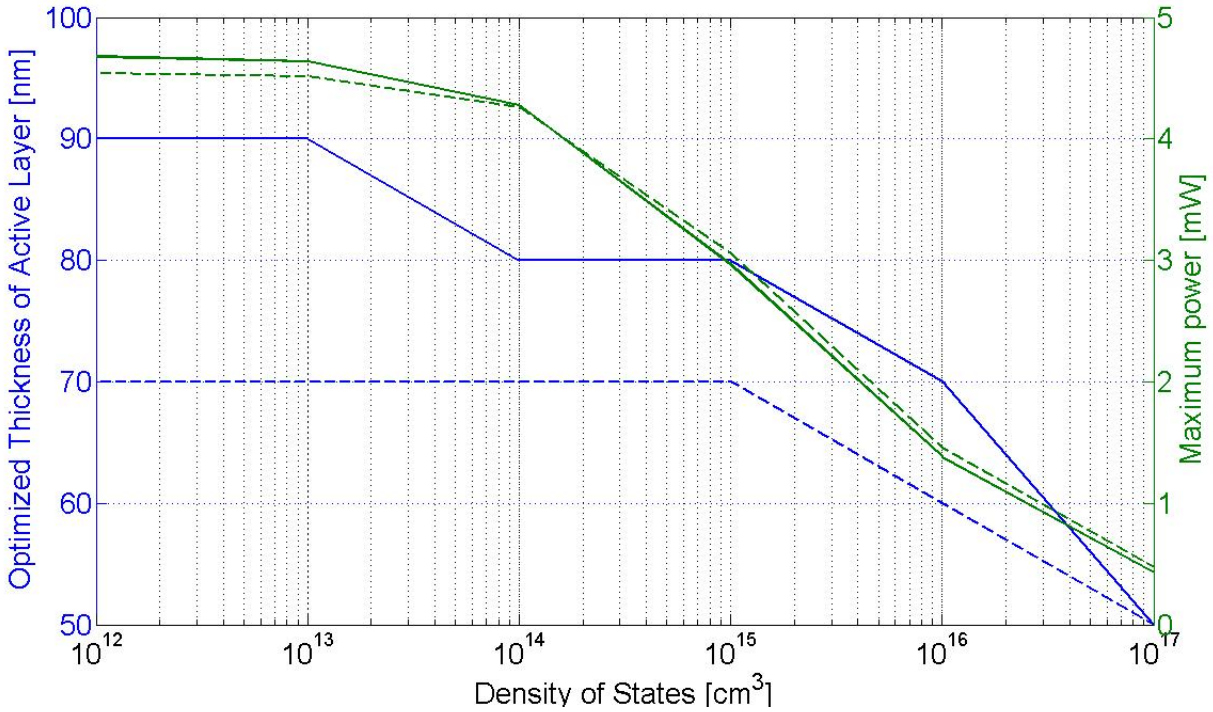

Figure 3.8: Optimal P3HT:PCBM layer thickness and resulting peak power as a function of trap states density

3.7 Summary

The relation between electrical resistivity and optical transmissivity of ultra-thin metals has been studied by considering the electron mean-free-path. We develop a simple model to consider the resistivity enhancement due to the impact from electron mean-free-path for ultra-thin metals. By using Sentaurus Device simulator, we explore optimized thickness of active layer and its relation with the optical generation peaks inside active layer. Also, from the electrical device point of view, we calculate the critical resistivity of anode metal layer. The device simulation results show that silver layers thinner than 5 nm perform comparably to 100 nm ITO and suggest the possibility of replacing ITO with ultra-thin silver. Finally, we explore the light enhancement due to the presence of nano-grating structure at cathode backcontact. Our simulation conclude that nano-gratings with 300 nm in width and 60

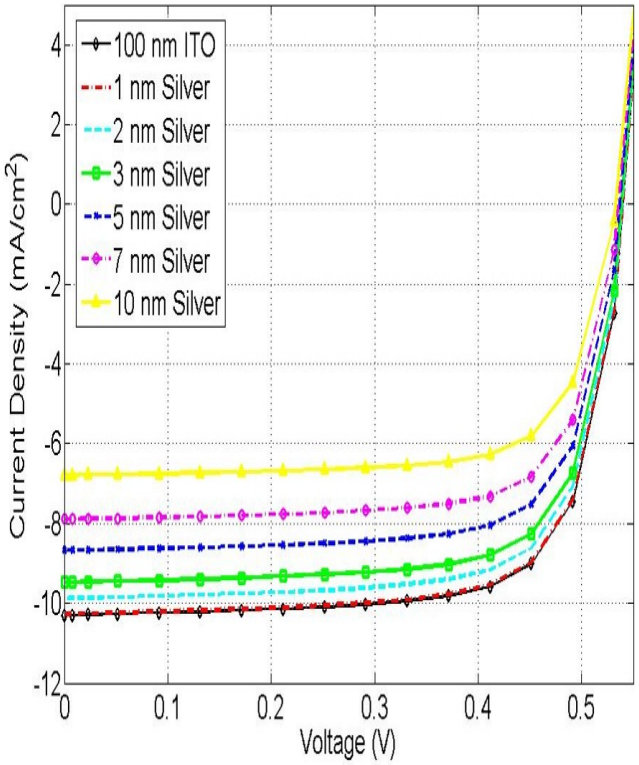

Figure 3.9: I-V characterization of 100 nm ITO vs. ultra-thin silver as anode material.

nm in height can increase the total charge carrier generation by a factor of 21%. The presented method can be applied to a large variety of flexible nanostructured devices in future applications.

Chapter 4

MODELING OF PHASE SEPARATION PHENOMENON AND SCREENING EFFECT AT NANOGAP

The post thermal annealing process after the spin-on process of poly(3-hexylthiophene): [6,6]-phenyl-C61-butyric acid methyl ester (P3HT:PCBM) is essential in establishing charge carrier channels for organic light-absorbing materials. The phase separation process during the post-annealing treatment is of great research interest. This chapter discusses the modeling of phase separation process by utilizing Cahn-Hilliard equation. By using Fast Fourier Transform (FFT) and LU decomposition methods, we can simulate the phase formation and evolution as a function of time and material-specific parameters. On the other hand, the charge carrier mobility in disordered organic semiconductors depends negatively on the square root of external electric field due to the screening effect. We conducted simulation as comparison with experimental measurements of the charge transport characteristics of P3HT:PCBM between lateral nanogap electrodes. Computer simulation shows the negative mobility trend with decreasing nanogap spacing to be a result of the accumulation of space charges between nanogaps which reduce the impact from external electric field[1].

4.1 Overview

Photovoltaic devices based on molecular and polymeric materials offer the prospect of developing an inexpensive renewable energy source [51]. However, poor charge transport in disordered organic semiconductors, inadequate match of absorber spectrum to the solar spectrum, and low environmental stability present continuing challenges for the development of organic photovoltaics (OPVs) [52, 53, 54, 55, 56]. With power conversion efficiencies of $\approx 8\%$ [57, 58], bulk heterojunction (BHJ) organic solar cells [59], comprised of a blend of a donor polymer and a fullerene small molecule, are currently the most efficient OPV devices.

[1]This chapter is adapted from a paper submitted to *ACS Nano*. [50].

New donor and acceptor materials and control of the active layer morphology have primarily contributed to the continued enhancement of OPV device efficiency over the past decade [57].

Presently there have been attempts to redesign the standard planar device architecture using structured electrodes to optimize the processes in OPVs: photon absorption, exciton separation, charge carrier transport and collection. Lateral homojunction devices, buried heterojunction devices, wire electrodes and nano-patterned electrodes have all been explored as alternatives to planar device geometries, which in most cases, show efficiency enhancements over planar control devices [60, 61, 62]. One intention behind nano-patterned electrodes is to reduce inter-electrode spacing down to the length scales comparable to phase-separation of the donor and acceptor phases (≈10-30 nm) to promote charge carrier collection [63]. In addition, when the interelectrode distance approaches the same length scale as the BHJ blend phase separation, the positional disorder of the BHJ blend is hypothetically minimized so the overall charge carrier mobility should in theory increase. Positional disorder in organic semiconductors is a measure of the degree of intersite coupling between electronic states, so reflects disorder of charge transport pathways in BHJ blends and in rapidly cooled organic semiconductor films [64]. This disorder-mobility dependence in nanogap geometries has been modeled in poly(3-hexylthiophene):[6,6]-phenyl-C61-butyric acid methyl ester (P3HT:PCBM) diodes, resulting in the prediction that the charge carrier mobility should increase ten-fold when scaling from 60 nm to 20 nm lateral diodes [65]. Moreover, theoretical device models have predicted PCEs as high as 18% in complex lateral nanogap devices [66].

Underlying this modeled efficiency increase is the possibility of enhanced charge carrier transport within the organic semiconductors. Recent work by the Sirringhaus group has correlated a low degree of energetic disorder with high charge carrier mobility in thin film transistors (TFTs) [67], which have been extensively employed to study charge transport properties of different conjugated systems [68]. Furthermore, Coehoorn (2007) predicted that energetic disorder in guest-host systems can result in a pronounced dependence of mobility on the charge carrier density [69]. Gregg [70] and co-workers have investigated the influence of charged defects on transport in organic photovoltaics as dopants in non-

conjugated polymers [71] despite their well-known adverse influence on the photochemical stability of solar cells based on conjugated polymers like P3HT.

Although significant progress has been made in understanding the fundamental limitations of transport in large area planar BHJ OPVs [72], a detailed understanding of the scaling of mobility and the corresponding role of disorder in BHJ blends at the nanoscale has not been as well studied experimentally. The present work attempts to verify model predictions by direct measurement of charge transport properties in lateral and planar P3HT:PCBM blend diodes as a function of inter-electrode distance using charge extraction by a linearly increasing voltage (CELIV) [73], which can be used later to derive appropriate measures of energetic and positional disorder within the context of a Gaussian disorder model of charge transport [40, 74].

4.2 Gaussian Disorder Model and Screening Effect at Nanogap

4.2.1 Poole-Frenkel and Gaussian Disorder Model

The mechanisms of charge transport in organic semiconductors are not clear. One famous mobility model is Poole-Frenkel trapping model [75], which can be written as [16]:

$$\mu = \mu_0 exp\left(\gamma\sqrt{E}\right) \tag{4.1}$$

where μ_0 and γ are parameters which depend on the physics of the considered system, and E is the electric field.

Poole-Frenkel mobility has been extensively studied for modeling charge transport in not only organic light-emitting diodes with disordered semiconductors [76, 77, 78], but also in organic field effect transistors [79, 80, 81].

In disordered organic semiconductors, charge transport occurs mainly by hopping between nearby localized states which are induced by disorder. In a transistor, the physical effect of the source-drain electrical field is then to effectively reduce the hopping barrier. Assuming also a Coulomb potential type for hopping barrier, the hopping probability and the mobility, will have a dependence on electrical field which follows a Poole-Frenkel law like Eq. 4.1 with zero-field mobility μ_0 given by:

$$\mu_0 = \mu_i exp\left(-\frac{\Delta}{k_B T}\right) \tag{4.2}$$

where μ_i is the intrinsic mobility at zero hopping barrier and Δ is the zero-field hopping barrier, also known as low field activation energy. Thus, Eq. 4.1 can be rewritten as:

$$\mu = \mu_i exp\left(-\frac{\beta\sqrt{E} - \Delta}{k_B T_{eff}}\right) \tag{4.3}$$

where $\frac{1}{\mathrm{T_{eff}}} = \frac{1}{\mathrm{T}} - \frac{1}{\mathrm{T_0}}$ is the effective temperature to better fit with experimental results [82]. Clearly, the log of mobility μ is proportional to the electric field (E), $\ln\mu \propto \exp\left(\sqrt{\mathrm{E}}\right)$ and inversely proportional to temperature (T), $\ln\mu \propto \mathrm{T}^{-1}$. While the Poole-Frenkel model is simple and applicable in many systems, its generalization does not capture effects such as negative electric field dependent mobility or explain Poole-Frenkel behavior in trap-free systems [40]. This is because the Poole-Frenkel model is lack of several physical considerations, such as the energy distribution of charge transport sites (disorder energy).

As a result, the Gaussian Disorder Model (GDM) is introduced [40]. The GDM model assumes that electron-phonon coupling is sufficiently weak so that the polaronic effects can be neglected, and the hopping rates can be described by the Miller-Abrahams formalism [83]. The Monte-Carlo simulation suggests the charge carrier mobility is temperature- and field-dependent, and in the limit of high electric fields is given by [40]:

$$\mu_{GDM} = \mu_0 exp\left[-\left(\frac{2\sigma}{3k_B T}\right)^2\right] \times \begin{cases} exp\left[C\left(\left(\frac{\sigma}{k_B T}\right)^2 - \Sigma^2\right)\sqrt{E}\right], & \text{if } \Sigma \geq 1.5 \\ exp\left[C\left(\left(\frac{\sigma}{k_B T}\right)^2 - 2.5\right)\sqrt{E}\right], & \text{if } \Sigma < 1.5 \end{cases} \tag{4.4}$$

where μ_0 is the mobility in the limit $\mathrm{T} \to \infty$, with values between 10^{-6} and $10^{-5}\mathrm{m}^2/(\mathrm{V}\cdot\mathrm{s})$, C is a constant that depends on the site spacing, and Σ is the degree of positional disorder.

4.2.2 Device Simulation Setup

According to the actual device setup, we set up 2D device simulation including 50 nm $*$ 50 nm gold electrodes on both sides with a gap containing P3HT:PCBM with gap-spacing varying from 30 nm to 200 nm, followed by 300 nm SiO_2 and 1 μm silicon beneath the gap.

The P3HT:PCBM undercuts SiO_2 layer by 8nm, and covers the entire device by 20nm. We used periodic boundary conditions for left and right boundaries in order to realize the actual device, as illustrated in Fig. 4.1.

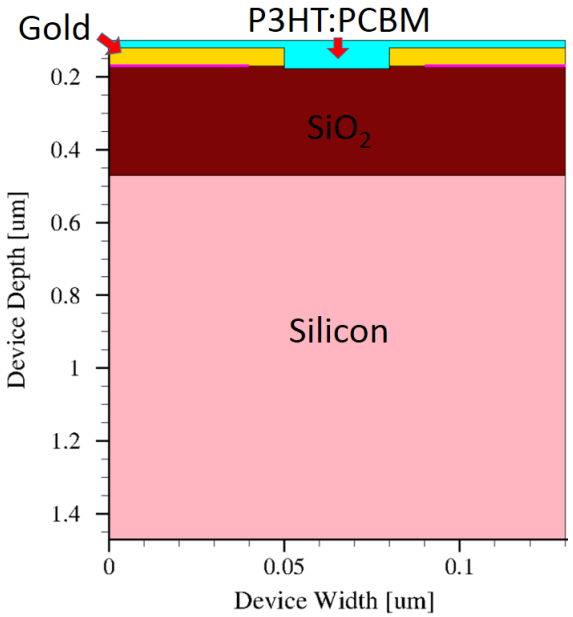

Figure 4.1: Structure of device simulation. The calculated structure contains 1 μm silicon substrate, covered by 300 nm SiO_2 with 50 nm gold electrodes on top. The channel is covered by P3HT:PCBM layer, with the width of channel varying from 30 nm to 200 nm.

While electron blocking layers can be easily added in planar diodes, it is experimentally complicated to add such layers in nanogap devices and/or fabricate dissimilar metal electrodes over measurable areas [84]. It is convenient to use a single, highly conducting electrode material such as gold (Au), which has a hole injection barrier between the Au Fermi level and the P3HT HOMO level of 0.5-1 eV. The energy barrier at the Au/P3HT interface has been attributed to the formation of electrostatically induced interfacial dipoles and molecular screening effects [85, 86, 87]. While there is some leakage in this configuration, the energy barrier is sufficient to induce rectification in P3HT:PCBM nanogap diodes as shown in the current-voltage characteristics in Fig. 4.2(d). These results corroborate Worne *et al.*'s observation that a depletion region forms in the HOMO level tail of P3HT at the

Au interface in Au/P3HT/Au FETs with a channel width of 120 nm [88]. At metal-organic interfaces in general, energy band alignment deviates from the Schottky-Mott model, and Fermi level alignment is approximated by a modified induced density of interface states model [89]. Fig. 4.2(e) shows a proposed band diagram in equilibrium and during CELIV for Au/P3HT:PCBM/Au diodes, where charge injection barriers for both electrons and holes are present in PCBM and P3HT, respectively.

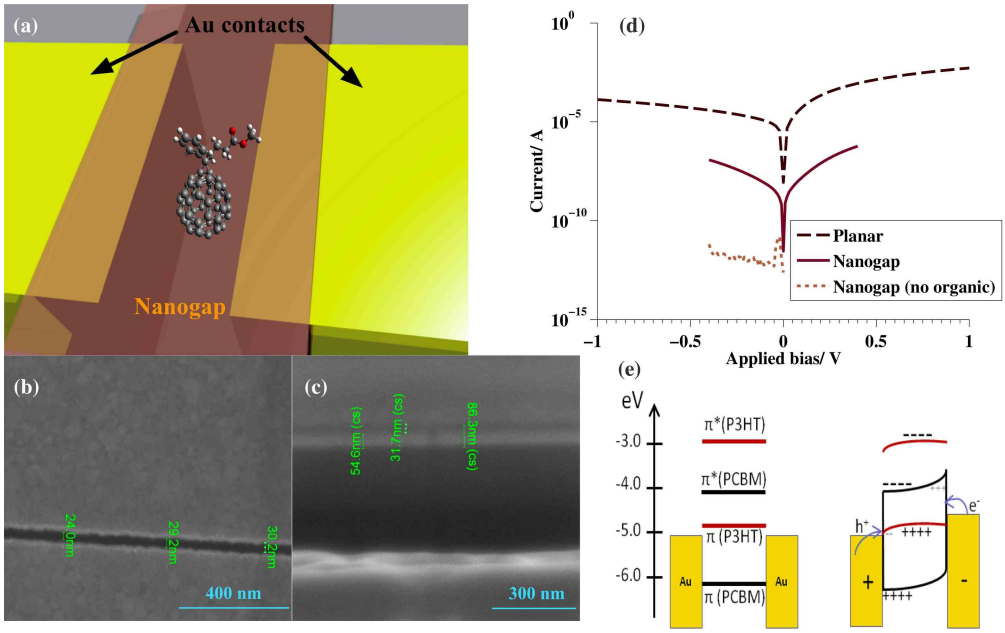

Figure 4.2: (a) Schematic of the lateral nanogap structure with a PCBM molecule depicted; (b) Scanning electron micrograph of the 30 nm gap width; (c) Focused Ion-Beam mill cross-section of the gap prior to the final ion milling step; (d) Device I-V characteristics for the planar and nanostructured device with and without the P3HT:PCBM layer; (e) Schematic of the energy level alignment at the Au-P3HT interface during CELIV measurements.

To better understand the trends in the scaling of mobility and to evaluate the effect of the presence of the gate oxide in the lateral structure, coupled electrostatic and carrier density calculations were carried out to obtain an estimate of the spatial variation of the internal electric field and the space charge density in the nanogap P3HT:PCBM diodes. Fig. 4.3(a) and (b) show the electric field and space charge in the 30 nm gap diode. The

electrostatic potential extends throughout the bulk of the 30 nm device with an average electric field value of 2×10^5V/cm. In comparison, this field strength in the 200 nm device is only present in the first 10 nm near the electrode.

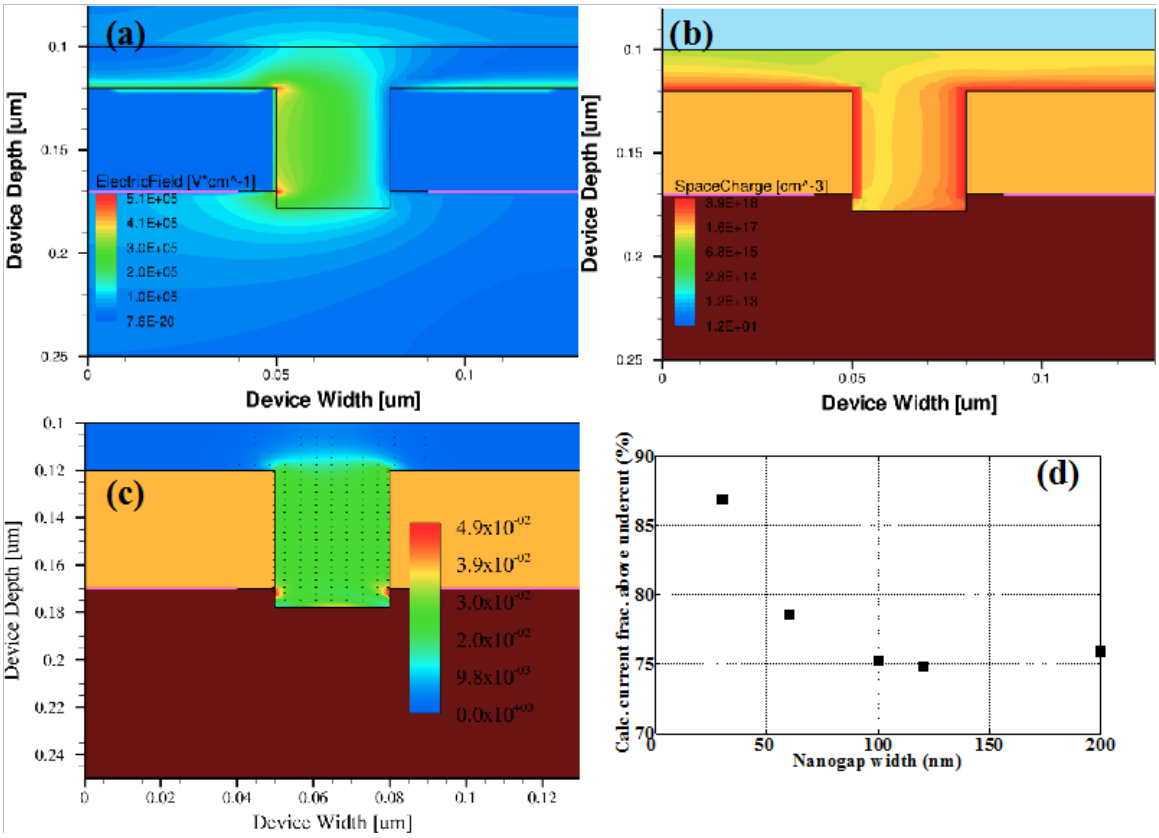

Figure 4.3: (a) Calculated electric field in the 30 nm nanogap; (b) space charge density; (c) current density; and (d) calculated fraction of current that flows above the undercut. Electric field, charge density and current results for gaps larger than 30 nm are included in Fig. 4.4.

The simulations of the 60-200 nm devices are shown in Fig. 4.4, with all the materials' parameters listed in Table 4.1.

As the electrostatic potential extends into the bulk of the organic semiconductor blend, the mobility is found to decrease with nanogap spacing. Concentrated electric fields at the electrode edges in the lateral device geometry appear to be the reason for a doubling of

Table 4.1: Device Simulation Parameters for Investigating the Impact from Nano-Gap

Parameter Name	Parameter Symbol	Parameter Value
ITO thickness	t_{ITO}	100 nm
PEDOT:PSS thickness	t_{PEDOT}	50 nm
P3HT:PCBM active layer thickness	t_{active}	40 - 240 nm
aluminum back-reflector thickness	t_{back}	100 nm
P3HT:PCBM electron affinity	χ	3.9 eV
P3HT:PCBM bandgap	E_g	5.1 eV
P3HT:PCBM relative permittivity	ϵ_r	3.8
P3HT:PCBM effective electron trap density	N_e^{trap}	10^{12} - 10^{17} [cm^{-3}]
P3HT:PCBM effective hole trap density	N_h^{trap}	10^{12} - 10^{17} [cm^{-3}]
P3HT:PCBM degree of position disorder	Σ	1.0 - 1.8
P3HT:PCBM electron mobility	μ_e	3×10^{-2} [$cm^2/(V \cdot s)$]
P3HT:PCBM hole mobility	μ_h	1×10^{-3} [$cm^2/(V \cdot s)$]

the charge carrier mobility and the two orders of magnitude greater electrical conductivity compared to planar devices for a given electric field strength (Fig. 4.5). The charge density simulation results (Fig. 4.3(b) and Fig. 4.5(c),(f),(i)) are consistent with the extracted charge carrier concentrations from the CELIV transient (Fig. 4.5) and indicate that a significant space charge density exists in the P3HT:PCBM blend on the order of $\approx 10^{18} cm^{-3}$.

4.3 Cahn-Hilliard Equation and Phase Separation during Annealing

The post thermal annealing process after the spin-on process of P3HT:PCBM is essential in establishing charge carrier channels for organic light-absorbing materials [90, 91, 92, 93]. Basically after the thermal annealing, P3HT and PCBM tend to form their own domains, leaving 1-2 nm P3HT:PCBM channels for light-generated excitons to dissociate due to the mismatch of HOMO/LUMO levels of P3HT and PCBM [94, 95, 96], as illustrated in Fig. 4.6.

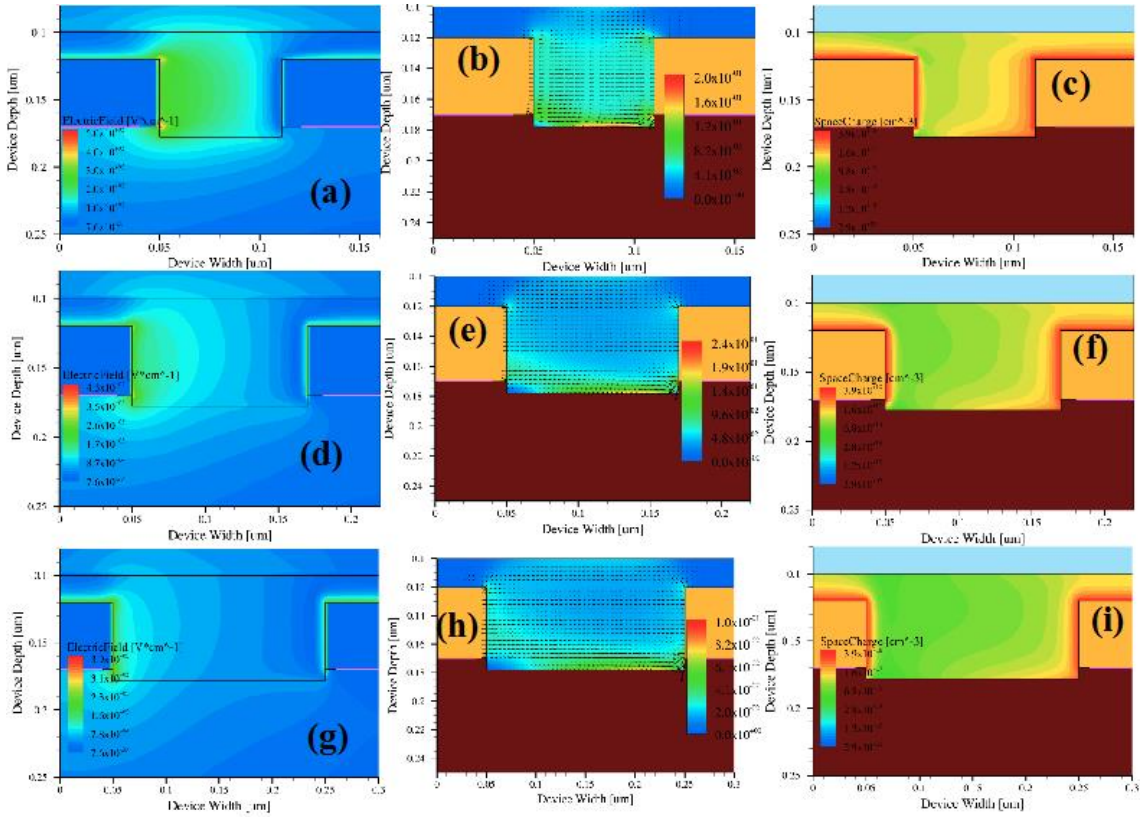

Figure 4.4: Calculation results for larger nanogaps: 60 nm ((a)-(c)), 120 nm ((d)-(f)) and 200 nm ((g)-(i)). The left column of the panel depicts the electric field distribution in the nanogap, the middle, the current, while the right column shows the space charge.

The Cahn-Hilliard equation, as shown in Eq. 4.5, is an equation of mathematical physics which describes the process of phase separation [97], by which the two components of a binary fluid spontaneously separate and form domains pure in each component:

$$\frac{\partial c}{\partial t} = D\nabla^2 \left(c^3 - c - \gamma\nabla^2 c\right) \tag{4.5}$$

where c is the concentration of the fluid with c = ±1 indicating domains, D is the diffusion coefficient, and $\sqrt{\gamma}$ gives the length of the transition regions between the domains.

It is also worthy of pointing out that by defining chemical potential $\mu = \mathrm{c}^3 - \mathrm{c} - \gamma\nabla^2\mathrm{c}$ and flux $\mathbf{j}(\mathrm{x}) = \mathrm{D}\nabla\mu$, the Cahn-Hilliard equation obeys the conservation law:

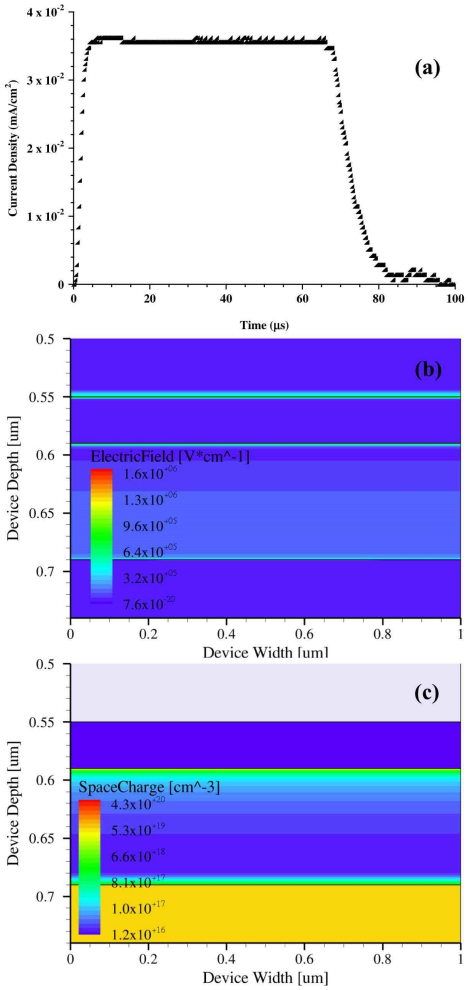

Figure 4.5: (a) CELIV data for planar devices. Higher current levels are manifested in the lower noise levels, compared to nanogap results. Calculated (b) electric field and (c) space charge for the planar devices.

$$\frac{\partial c}{\partial t} = \nabla \cdot \mathbf{j}(x) \tag{4.6}$$

In computational domain, we separate Cahn-Hilliard equation into two parts:

$$\begin{cases} \frac{\partial \phi}{\partial t} = \nabla \cdot \left(\frac{\gamma \lambda}{\epsilon^2} \psi \right) \\ \psi = -\nabla \cdot \left(\epsilon^2 \nabla \phi \right) + \left(\phi^2 - 1 \right) \phi \end{cases} \tag{4.7}$$

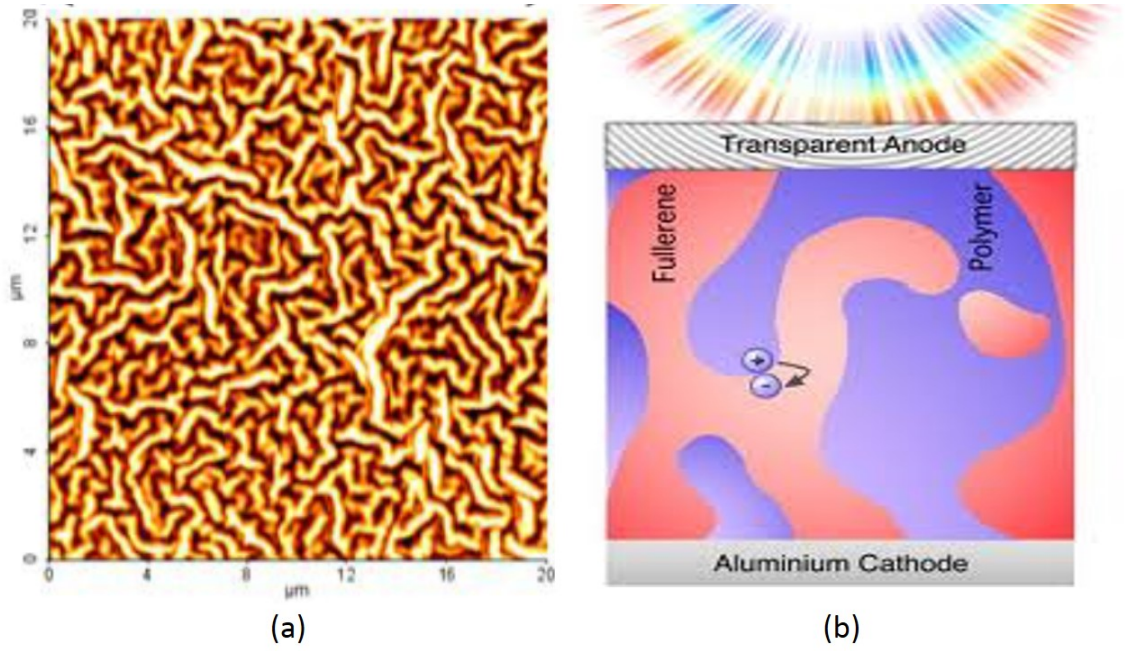

Figure 4.6: Phase separation phenomenon of P3HT:PCBM layer during post-annealing process. (a) is the conductive AFM measurement of electronic conductivity of P3HT:PCBM after 60 min annealing, while (b) illustrates the exciton dissociation at the P3HT/PCBM interface.

with $\sigma = \frac{2\sqrt{(2)}}{3}\frac{\lambda}{\epsilon}$ is the surface tension coefficient. The boundary condition is set to be:

$$\begin{cases} \mathbf{n} \cdot \left(\epsilon^2 \nabla\phi\right) = \epsilon^2 tan\left(\frac{\pi}{2} - \theta_w\right) \left|\nabla\phi - \left(\mathbf{n} \cdot \phi\right)\mathbf{n}\right| \\ \mathbf{n} \cdot \left(\frac{\gamma\lambda}{\epsilon^2}\psi\right) = 0 \end{cases} \tag{4.8}$$

Fig. 4.7 illustrates the time evolution of phase separation process, as calculated by Eq. 4.7 - 4.8. As shown in Fig. 4.7(a), the starting point is a perfectly-mixed state of P3HT and PCBM, with the ratio of P3HT to PCBM being 1:1. The thickness of P3HT:PCBM blend is 70 nm, and we choose the simulation width to be 70 nm as well. After 10 minutes, there is obvious change in the material concentration in the simulation domain. The red-colored region illustrates higher concentration of P3HT, while the dark-blue region is PCBM-favorable region. It is also interesting to realize that the $\approx$ 1-2 nm thickness of P3HT:PCBM interface region, as colored in yellowish-green, has a zigzag connection chan-

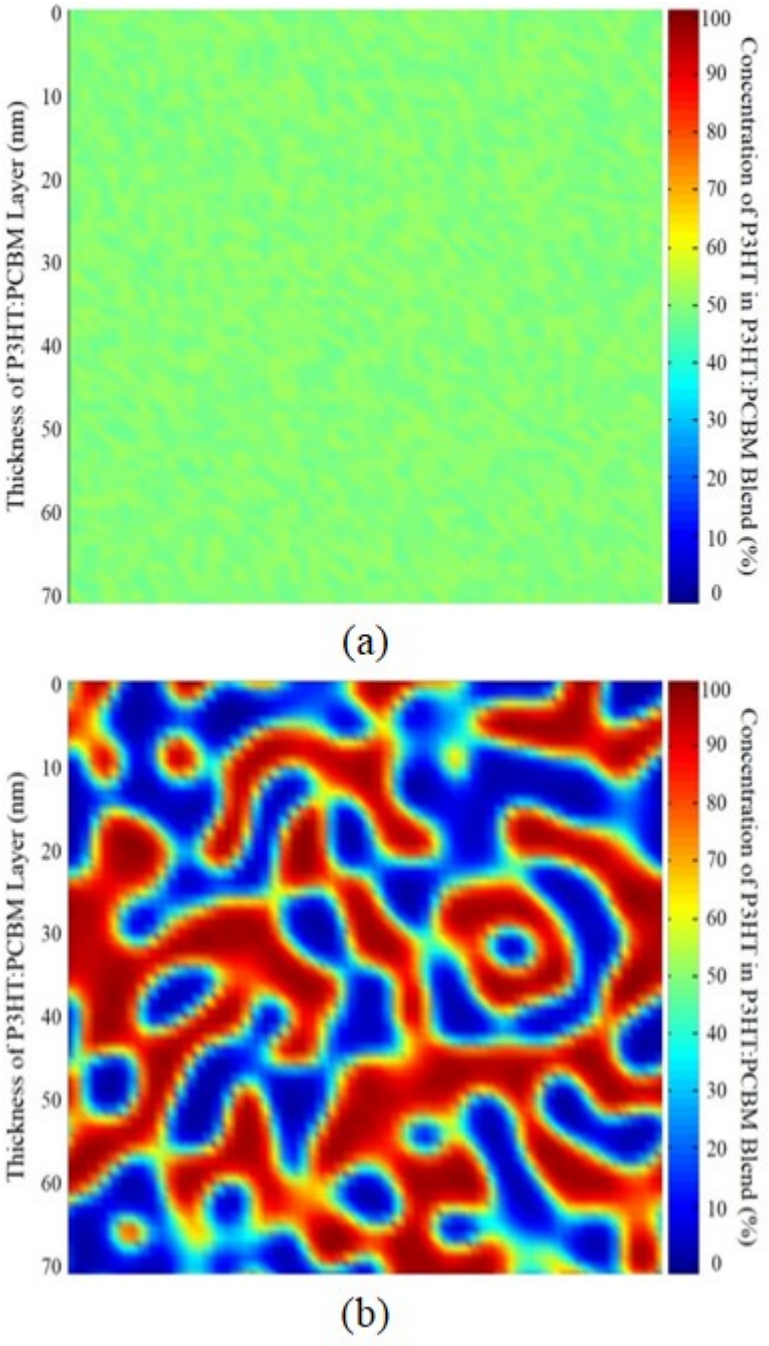

Figure 4.7: Simulation of phase separation phenomenon of P3HT:PCBM layer during post-annealing process. The red-colored region illustrates P3HT-rich region, while blue-colored region is PCBM-rich region.

nel from bottom to top. Since excitons dissociates at the P3HT:PCBM interface due to the mismatch of electron affinity and bandgap of P3HT and PCBM materials, electrons/holes that enter the interface region have to diffuse a distance much longer than the thickness of organic light-absorbing material (P3HT:PCBM) before get collected by the electrodes on top/bottom layer. What is worse, the interface region is not always connected from top to bottom. One example is the red-dot island at left-bottom region of Fig. 4.7(b). Thus, those electrons/holes that enter the interface region without connection to top/ bottom electrodes will be trapped in the local islands and the energies will be lost.

4.4 Summary

The phase separation phenomenon during post thermal annealing process of spin-coated P3HT:PCBM thin film has been numerically modeled via Cahn-Hilliard equation. The 1-2 nm interface regions that serve as center at which photon-generated excitons dissociate into electrons and holes have a longer length in connection between top and bottom electrodes. First-time CELIV measurements in nanogap devices and device simulations are used to explain the decreasing trend in mobility with nanogap spacing. Experimental results and simulations corroborate to show that the smallest nanogap devices exhibit reduced charge carrier mobility caused by screening of the internal electric field by the space charge generated in the device. This suggests that the electric field dependence of mobility within the context of the Gaussian disorder model likely remains negative, in agreement with the observed trends in charge carrier mobility in the nanogap devices and previous published results [98].

Chapter 5

OPTICS AND DEVICE MODELING OF SURFACE PLASMONIC EFFECT USING SILVER NANOPRISMS

We investigate silver nanoparticle enhanced organic solar cells (OPVs) by coupling three-dimensional electromagnetic and electronic device simulations. For active layer thickness of less than 50nm, an array of optimized silver nanoprisms with 12 nm edge length (covered by 1 nm dielectric material), 15 nm thickness, and 17 nm period length can enhance the power conversion efficiency (PCE) by more than 25% when embedded in a bulk heterojunction polymer blend. For thicker layers, optical losses associated with the particles outweigh the increased absorption and reduce the PCE. Additionally, we find that the nanoparticles work function determines the current-voltage behavior of plasmonic devices. By carefully tuning the work function of silver nanoparticle, we simulate the current-voltage curve with a fill-factor increased from 30% to 58%, which is high enough to work properly with the benefits of short-circuit current enhancement up to 21%[1].

5.1 Overview

Despite significant advances and reported power conversion efficiencies of more than 10% ([100], Fig. 5.1), important challenges remain towards the realization of a competitive low-cost energy platform based on thin-film organic photovoltaics (OPVs) [101]. Recently, OPVs employing metal nanostructures such as nanostructured metal back-reflectors [102] and metal nanoparticles [103] have been implemented as potential alternatives to conventional OPV structures due to better light management capability and, consequently, higher short-circuit currents, leading to improved power conversion efficiency [104].

The absorption enhancement in OPVs based on the excitation of metal nanoparticle mediated localized surface plasmon resonances is typically rationalized in terms of electro-

[1]This chapter is adapted from a paper published in *Appl. Phys. Lett.* [99].

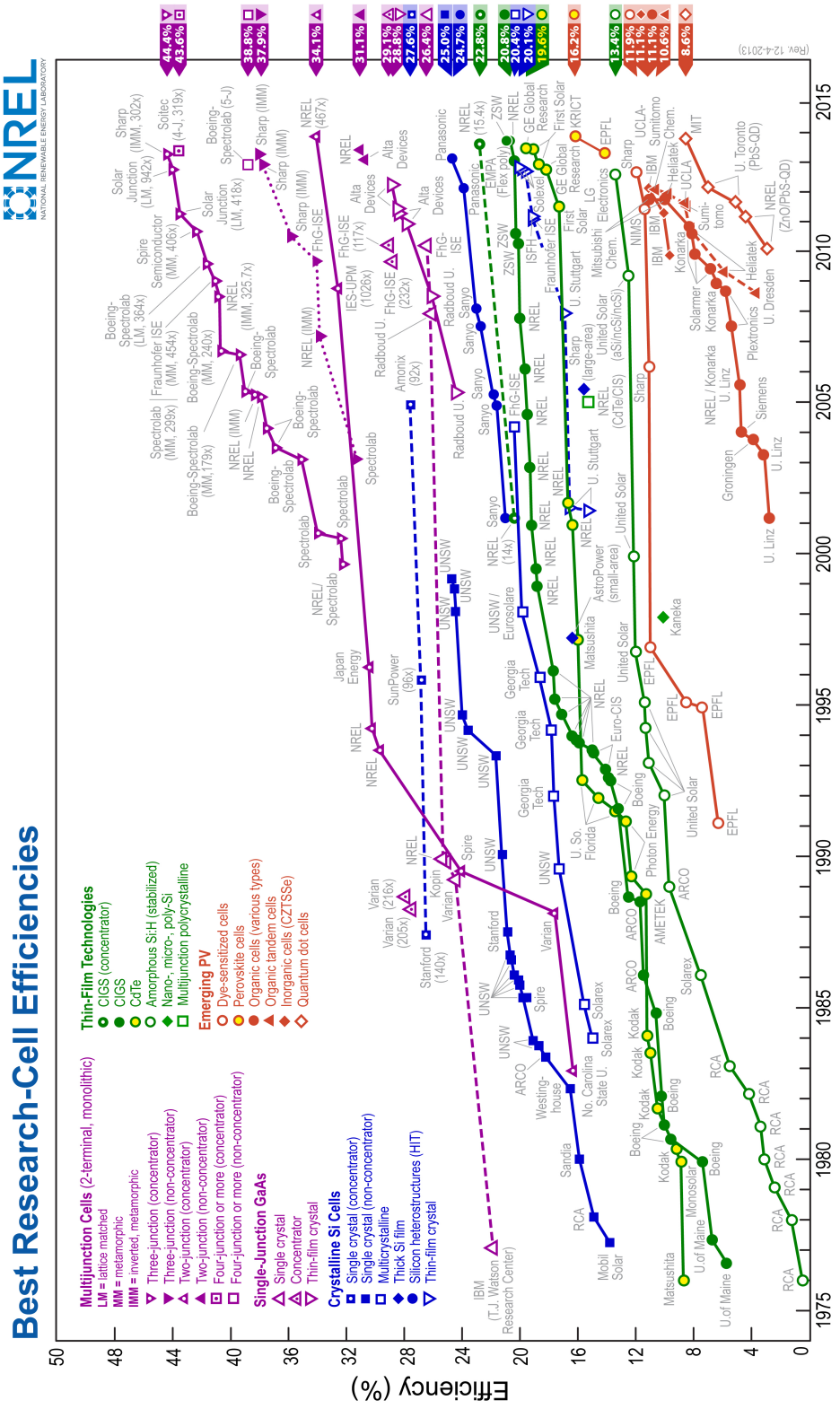

Figure 5.1: Best efficiency of various types of solar cells fabricated in research laboratories. The red-dotted line indicates the best performance for organic solar cells is as high as 11.1%, as reported by Mitsubishi Chem.

magnetic (EM) near-field and far-field (scattering) enhancement, which in the ideal case should result in increased photocurrent density [15]. However, both detrimental as well as favorable changes in open-circuit voltage (V_{OC}) [105], fill factor (FF) [106], and charge carrier mobility [107] have been observed. The origin of this behavior is not clear but may be associated with morphological changes in the case of FF [106] while electronic interactions or chemical reactions at the metal/polymer interface may explain changes in V_{OC} [105]. Charge transport through a metal nanoparticle network is thought to be in the origin of improved charge carrier mobility [107, 108]. Hence, a theoretical analysis is vital for the understanding and engineering of plasmon-enhanced OPVs.

Previous attempts to theoretically assess plasmon enhancements in OPVs have almost exclusively relied on quantifying the improvement due to the optical enhancement only [109, 110], missing for instance the impact of the metal particles on carrier transport and recombination. In order to describe the advantages and limitations of metal nanoparticle decorated OPVs we combined three-dimensional electromagnetic and device modeling and analyzed the plasmonic effects of silver nanoprisms on the device characteristics of regular poly-3-hexylthiophene:phenyl-C61-butyric acid methyl ester (P3HT:PCBM) devices, a well-studied model system (combined electromagnetic and electronic device simulations have been presented recently for inorganic thin-film solar cells [111, 112]). Silver nanoprisms are of particular interest because of their localized surface plasmon resonance (LSPR) tunability, high conductivity, chemical stability, and high EM field enhancement at the tips ($> 10^3$), i.e., much higher than in the case of spherical nanoparticles [113, 114].

5.2 Optics Optimization of AgNP Structure

We used a commercial Maxwell equations solver (Lumerical®) [115] based on the finite-difference time-domain (FDTD) method to compare the absorption enhancement in the active layer for different sizes, shapes, and particle densities of silver nanoprisms that are used as optical antennas to more effectively couple sunlight into the P3HT:PCBM layer. By extending a carrier transport model to accommodate P3HT:PCBM specific material parameters, and using the electromagnetic field data from the FDTD optimization, we conducted device simulations (Sentaurus Device software from Synopsys®) [116] for predicting the

current-voltage (I-V) and quantum efficiency characteristics of regular OPV structures with and without an optimized array of silver nanoprisms.

Based on the FDTD method, we numerically optimized the absorption enhancement that is induced by placing triangular silver nanoprisms (insulated with a 1 nm dielectric shell (n=1.5) to inhibit trap site formation for charge carriers [108]) inside a P3HT:PCBM (1:1) blend layer (Fig. 5.2(a)). Data for the complex refractive index of the blend are taken from Monestier *et al.* [117]. The dielectric function for PEDOT:PSS and ITO is taken from Hoppe *et al.* [118]. We use experimentally measured permittivity data under high vacuum from the literature to describe the silver metal nanoparticle, aluminum metal electrode, and glass [119]. For parameterization of the material data, a multi-coefficient model as provided by the software is used. We implement periodic boundary conditions in x and y direction. Perfectly matched layer (PML) boundary conditions are used at the top and bottom of the simulation volume. A mesh size of 0.5-1 nm is used in the vicinity of the metal nanoparticle.

Using the E-field data, we calculated the volume integrated optical absorption of the active layer (V is the volume of the active layer):

$$Ł(\omega) = \overline{\omega} \cdot Im(\epsilon) \int |E|^2 \, \mathrm{d}V \tag{5.1}$$

The absorption enhancement (AE) then results as the ratio of the optical absorption for a film with and without metal nanoparticles. We excluded the absorption of the metal particles from our AE calculations by employing a refractive index filter [115]. Then the spectrum-integrated absorption enhancement (IAE) using the AM1.5G solar spectrum is defined as follows:

$$IAE = \frac{\int L^{NP}(\lambda) I_{AM1.5}(\lambda) \mathrm{d}\lambda}{\int L^{bare}(\lambda) I_{AM1.5}(\lambda) \mathrm{d}\lambda} \tag{5.2}$$

where L^{NP} and L^{bare} are the optical absorption in the blend with and without nanoparticles, respectively.

Using the particle swarm optimization (PSO) algorithm provided by the Lumerical software [115, 120], we optimized the particle dimensions of the AgNPs as well as the particle period/density within the device structure shown in Fig. 5.2(a) to give maximum spectrum-

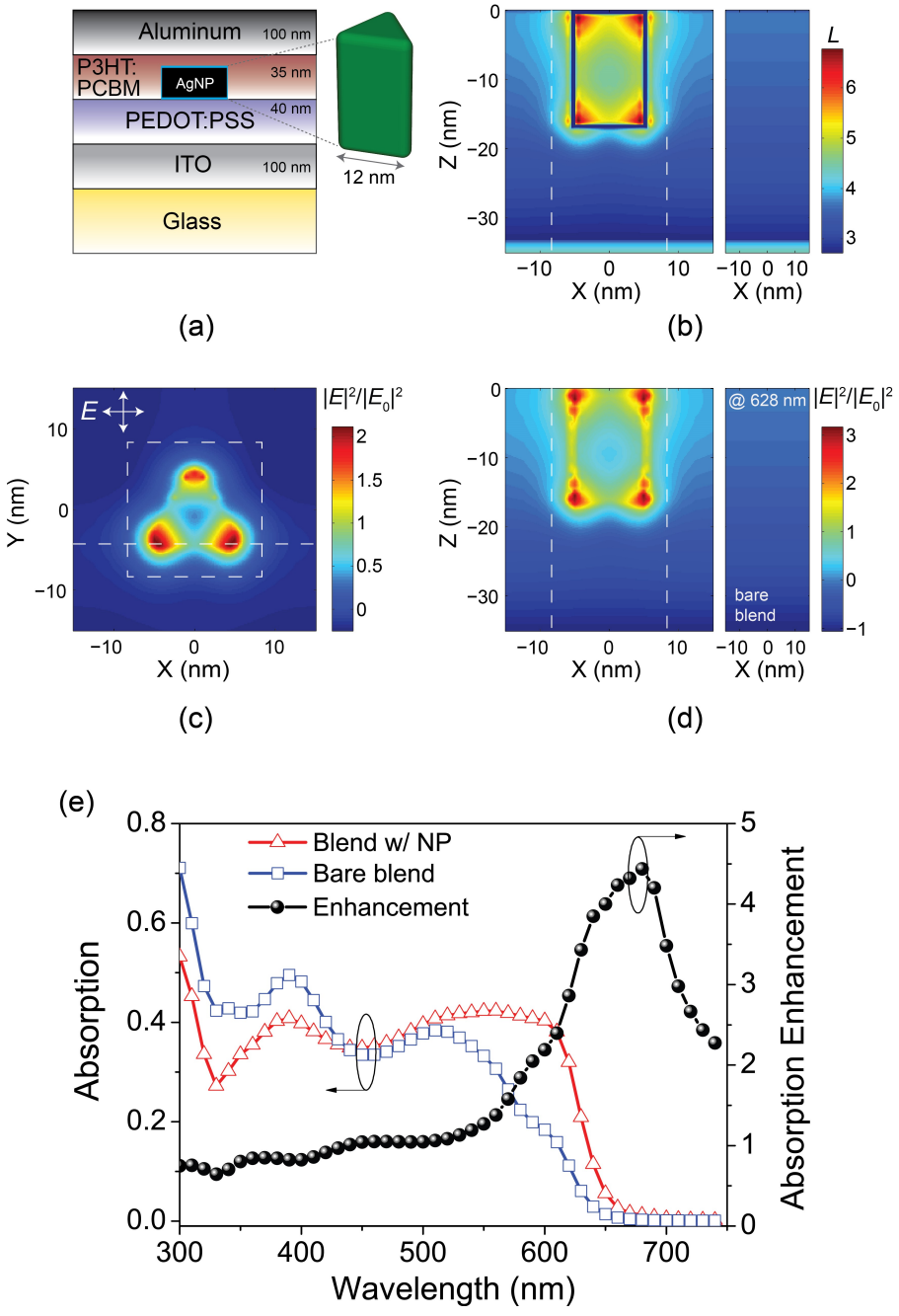

Figure 5.2: (a) Simulated structure of an organic solar cell containing optimized silver nanoprisms (AgNPs) covered by a 1 nm thick dielectric shell in the P3HT:PCBM blend layer; (b) Cross section of absorbed power in the P3HT:PCBM blend and AgNP region along the dashed horizontal line in (c); (c) Top view of the electric field component on a log scale normalized by the incoming light field ($|E|^2/|E_0|^2$) at the plasmon resonance of the AgNP for unpolarized light. The field distribution is taken at a plane 1 nm away from the particle surface; (d) Cross section of $|E|^2/|E_0|^2$ in the P3HT:PCBM blend with AgNPs. The dashed lines around the AgNP define the period length that lead to the best absorption enhancement. (e) Comparison of the fraction of light absorbed with and without optimized silver nanoprisms and absorption enhancement in a 35 nm P3HT:PCBM active layer device. The E-field calculations in (b)-(d) were performed at 628 nm.

integrated absorption enhancement (IAE). The particle swarm algorithm consisted of 40 generations, each featuring 20 simulations (800 simulations overall). Based on previous experimental work and experience, the range of possible particle dimensions and periods was limited to: thickness: 5-15 nm, edge length: 5-50 nm, period: 150-particle edge length. The active layer thickness was set to 35 nm to minimize the effects from the short ($\approx$ 5-10 nm) exciton diffusion length [121], the low charge carrier mobility ($\approx 10^{-4}\mathrm{cm}^2/(\mathrm{V}\cdot\mathrm{s})$), and to benefit from a large enhancement effect (Fig. 5.4(c)).

Fig. 5.2(b)-(d) compare the absorbed power and the normalized local electric field $|\mathrm{E}|^2/|\mathrm{E}_0|^2$, respectively, at the maximum of the AE curve (Fig. 5.2(e)) for a blend film with and without an optimized AgNP array. The confinement of the E-field is particularly strong around the edges and tips of the triangular shaped particle where the E-field enhancement is >200 (Fig. 5.2(c) and (d)). Because of the absorbing surrounding medium, the E-field enhancement decays quickly and prevails only up to a thickness of 20 nm (Fig. 5.2(c)). Consistently, the regions of high absorption in the blend coincide with the regions of high $|\mathrm{E}|^2$ values (Fig. 5.2(b) and (d)) around the particle.

For a realistic assessment of the possible enhancement in OPV performance, a silver nanoprisms array is embedded into the blend film of a regular device geometry consisting of the following layers: glass, ITO (100 nm), poly(3,4-ethylene dioxythiophene):poly(styrene sulfonate) (PEDOT:PSS) (40 nm), AgNP, P3HT:PCBM (35 nm), and aluminum (100 nm). The maximum IAE for this structure is achieved with AgNPs with 12 nm edge length (covered by 1 nm dielectric material), 15 nm thickness, and 17 nm period length (Fig. 5.2(b)), resulting in an integrated absorption enhancement of 27% for unpolarized light (Fig. 5.2(e)). Note that the aspect ratio, i.e., edge length/height, of the optimized particle shape is small ($\approx$ 0.7), while typically colloidal silver nanoprisms have aspect ratios >2 [114]. This rather unusual particle shape leads to an optimum spectral overlap between the $\pi - \pi^*$ absorption band of the P3HT polymer and the plasmon resonance of the metal nanoparticle and, consequently, maximum plasmonic near- and far-field enhancement in the device. The in-plane dipole resonance of the optimized particle is at $\approx$580 nm when embedded in the blend, and the absorption enhancement extends from $\approx$450 to 740 nm (Fig. 5.2(e)). Below 450 nm the absorption is more efficient without metal nanoparticles

because of the losses associated with the reflectivity of the particle array. Note that we do not account for the difference in polymer blend volume between the plasmonic and the reference cell, which allows us to conclude that our predictions are more on the low end of possible enhancements.

5.3 Device Simulation and Impact from Silver Workfunction

The result of the particle swarm optimization via Lumerical is used as the input for Sentaurus Electromagnetic Wave Solver (EMW) [122]. The E-field data from EMW is then fed into Sentaurus Device simulation [116, 123]. For the electronic device simulation, the Poisson equation (with trap states):

$$\nabla^2\Phi = -\frac{q\left(p - n + N_d^+ - N_a^-\right) + \rho_{trap}}{\epsilon_0\epsilon_r} \tag{5.3}$$

is coupled with the electron and hole continuity equations:

$$\begin{cases} \frac{\partial n}{\partial t} = \frac{1}{q}\nabla\cdot\mathbf{J}_n + G - R_{net} \\ \frac{\partial p}{\partial t} = -\frac{1}{q}\nabla\cdot\mathbf{J}_p + G - R_{net} \end{cases} \tag{5.4}$$

for inorganic semiconductor modeling [124], where Φ is the electrostatic potential, n and p are the electron and hole densities, $\mathrm{N_d^+}$ and $\mathrm{N_a^-}$ are the concentrations of ionized donors and acceptors, ρ_{trap} is the charge density contributed by traps, ϵ is the electrical permittivity, $\mathrm{G} = \eta\mathrm{W}/\mathrm{E_{ph}}$ is the singlet exciton generation rate with η being the quantum yield. The power density $\mathrm{W} = -\nabla\cdot\overline{\mathbf{S}}^2$ with the time-averaged Poynting vector $\mathrm{S} = \frac{1}{2}\mathrm{R}(\mathbf{E}\times\overline{\mathbf{H}})$ and the photon energies $\mathrm{E_{ph}}$ are provided by the EM simulations and form the link between optical and device calculations. The electron and hold drift-diffusion currents can be expressed as [111]:

$$\begin{cases} \mathbf{J}_n = qD_n\nabla n - n\mu_n\left(q\nabla\Phi + \nabla\chi + k_BT\nabla lnN_c\right) \\ \mathbf{J}_p = -qD_p\nabla p - p\mu_p\left(q\nabla\Phi + \nabla\chi + \nabla E_g - k_BT\nabla lnN_v\right) \end{cases} \tag{5.5}$$

where χ is the electron affinity, $\mathrm{E_g}$ is the effective band gap, $\mathrm{N_c} = 2\left(\frac{\mathrm{m_c k_B T}}{2\pi\hbar^2}\right)$ and $\mathrm{N_v} = 2\left(\frac{\mathrm{m_v k_B T}}{2\pi\hbar^2}\right)$ are the effective conduction/valence band density of states in the P3HT:PCBM blend, $\mathrm{D_n} = \mu_\mathrm{n}\mathrm{k_B T/q}$ and $\mathrm{D_p} = \mu_\mathrm{p}\mathrm{k_B T/q}$ are the electron and hole diffusion coefficients,

with μ_{n} and μ_{p} being the electron and hole mobility, $\mathrm{k_B}$ the Boltzmann constant, and T=300K the operating temperature. We assume the presence of a Shockley-Read-Hall recombination rate:

$$R_{net} = \frac{np - n_{i,eff}^2}{\tau_p(n + n_1) + \tau_n(p + p_1)} \tag{5.6}$$

with $\mathrm{n_1 = n_{i,eff} exp\left(\frac{E_{trap}}{k_B T}\right)}$ and $\mathrm{p_1 = n_{i,eff} exp\left(-\frac{E_{trap}}{k_B T}\right)}$. For organic materials, the electrons and holes excited by incident light are initially tightly bound together through Coulomb forces, forming excitons [125]. Thus, we apply a singlet-exciton continuity equation to represent the behavior of excitons that can diffuse to the P3HT:PCBM interface and dissociate into electrons and holes:

$$\frac{\partial N_{ex}}{\partial t} = \nabla \cdot D_{ex} \nabla N_{ex} + G - R_{ex} - \frac{N_{ex} - N_{ex}^{eq}}{\tau} \tag{5.7}$$

where $\mathrm{N_{ex}}$ is the singlet exciton density, $\mathrm{D_{ex}}$ is the singlet exciton diffusion constant, $\mathrm{R_{ex}}$ is the net singlet exciton recombination rate, and τ is the singlet exciton lifetime.

Electronic device calculations involve Eq. 5.3-5.7 to simulate the electrical behavior of organic solar cells, while solving for electric field and electrostatic potential distribution inside the device to give device performance parameters such as short-circuit current ($\mathrm{J_{sc}}$), open-circuit voltage ($\mathrm{V_{oc}}$), maximum power density ($\mathrm{P_{max}}$), and fill-factor (FF), which are calculated as [112]:

$$\begin{cases} \mathbf{J}_{sc}(\lambda) = \frac{1}{V} \iiint_V \left|\mathbf{J}_n(\mathbf{x}, \lambda) + \mathbf{J}_p(\mathbf{x}, \lambda)\right| \mathrm{d}V \Rightarrow \mathbf{J}_{sc} = \int \mathbf{J}_{sc}(\lambda) \mathrm{d}\lambda \\ V_{oc} = \frac{k_B T}{q} ln\left(\frac{\mathbf{J}_{sc}}{\mathbf{J}_0} + 1\right) \\ P_{max} = max\left\{\mathbf{J}(V) \cdot V\right\} = max\left\{\mathbf{J}_0 \cdot V\left[exp\left(\frac{qV}{k_B T}\right) - 1\right] - \mathbf{J}_{sc} \cdot V\right\} \\ FF = \frac{P_{max}}{J_{sc} \cdot V_{oc}} \end{cases} \tag{5.8}$$

where V is the volume of the solar cell, $\mathbf{J}_{\mathrm{n}}$ and $\mathbf{J}_{\mathrm{p}}$ are the electron and hole drift-diffusion currents, respectively. The current-voltage (I-V) response of the solar cell is:

$$\mathbf{J}(V) = \mathbf{J}_0 \left[exp\left(\frac{qV}{k_B T}\right) - 1 \right] - \mathbf{J}_{sc} \tag{5.9}$$

where $\mathbf{J}_0$ is the reverse saturation current.

So the external (EQE) and internal quantum efficiency (IQE) are calculated by:

$$\begin{cases} EQE(\lambda) = \frac{\mathbf{J}_{sc}(\lambda)/q}{\mathbf{J}_{AM1.5}(\lambda)/E_{ph}} = \frac{\lambda}{qhc}\frac{\mathbf{J}_{sc}(\lambda)}{\mathbf{J}_{AM1.5}(\lambda)} \\ IQE(\lambda) = \frac{EQE(\lambda)}{Abs(\lambda)} \end{cases} \tag{5.10}$$

where $E_{ph} = hc/\lambda$ is the incident photon energy, $\mathbf{J}_{AM1.5}(\lambda)$ is the incident sunlight density, and $Abs(\lambda)$ is the absorption in the active layer at wavelength λ. All the materials' parameters used for device simulation are listed in Table 5.1.

Fig. 5.3 shows the calculated electron density as well as the exciton generation rate for the optimized AgNP structure. In analogy to the absorption shown in Fig. 5.2, charge generation is particularly strong in close proximity to the AgNP.

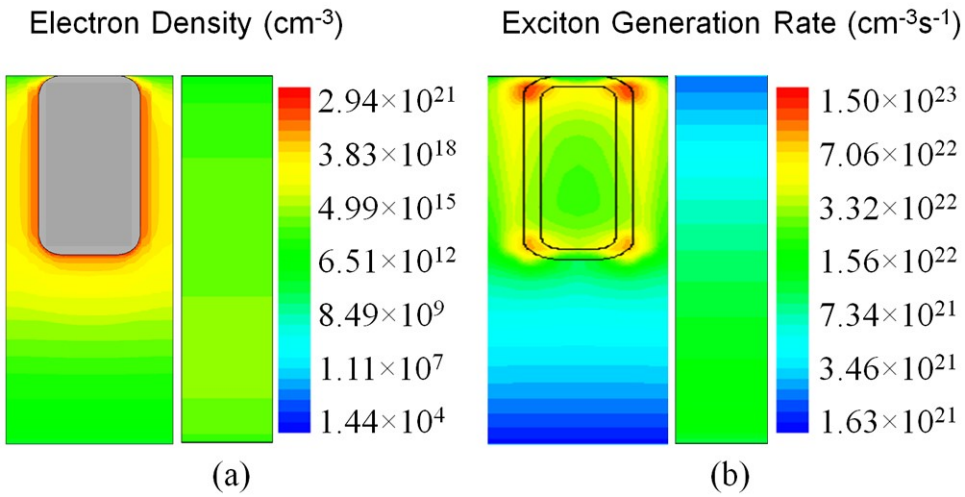

Figure 5.3: Cross sections of simulated (a) electron concentration and (b) exciton generation rate in the P3HT:PCBM blend under AM1.5G solar excitation for an organic solar cell with and without silver nanoprisms. For an OPV with AgNPs, the structure is along the dashed horizontal line of Fig. 5.2(c).

Calculated and experimental current-voltage (I-V) plots, together with external (EQE)

Table 5.1: Device Simulation Parameters for Investigating the Surface Plasmonic Effect

Parameter Name	Parameter Symbol	Parameter Value
ITO thickness	t_{ITO}	100 nm
PEDOT:PSS thickness	t_{PEDOT}	50 nm
P3HT:PCBM active layer thickness	t_{active}	40 - 240 nm
aluminum back-reflector thickness	t_{back}	100 nm
P3HT:PCBM electron affinity	χ	3.9 eV
P3HT:PCBM bandgap	E_g	5.1 eV
P3HT:PCBM relative permittivity	ϵ_r	3.8
P3HT:PCBM effective electron trap density	N_e^{trap}	10^{12} - 10^{17}cm^{-3}
P3HT:PCBM effective hole trap density	N_h^{trap}	10^{12} - 10^{17}cm^{-3}
P3HT:PCBM Langevin reduction parameter	α	1×10^{-4}
P3HT:PCBM Langevin reduction parameter	β	9×10^{-4}
P3HT:PCBM Gaussian width of LUMO level	σ_e	0.032 eV
P3HT:PCBM Gaussian width of HOMO level	σ_h	0.027 eV
P3HT:PCBM effective DoS in Gaussian LUMO level	N_e	3.6×10^{17}cm^{-3}
P3HT:PCBM effective DoS in Gaussian HOMO level	N_h	4.2×10^{19}cm^{-3}
P3HT:PCBM electron mobility	μ_e	3×10^{-5} [cm^2/(V $\cdot$ s)]
P3HT:PCBM hole mobility	μ_h	1×10^{-6} [cm^2/(V $\cdot$ s)]

and internal quantum efficiency (IQE) plots for a P3HT:PCBM device at 1 sun, with and without optimized silver nanoprisms, are illustrated in Fig. 5.4. We first fit our model parameters for an OPV without silver nanoprisms to match experimental I-V curves, including work functions of ITO, PEDOT:PSS, and aluminum, as well as the HOMO/LUMO levels and electron/hole mobilities of P3HT:PCBM (see Fig. 5.4(a) and inset). After the fitting process, we calculated the I-V and QE plots for an OPV device in the presence of silver nanoprisms. Fig. 5.4(a) demonstrates that including silver nanoprisms inside a 35 nm active layer increases the current density by ≈21% from 2.12 mA/cm^2 to 2.57 mA/cm^2 without noticeably affecting the open-circuit voltage. In this case, the overall PCE increases by 26% from 0.73% to 0.92%. For comparison, enhanced absorption efficiency in the order of 20% has been theoretically predicted [109] and photocurrent enhancement in the order of 13-16% experimentally reported [126, 127] for OPVs by exploiting light scattering from metal spheres [127], cubes [109] and rods [126].

Fig. 5.4(b) (inset) shows that the calculated EQE spectrum matches the experimental spectrum closely. Importantly, the EQE enhancement in the presence of silver nanoprisms extends from ≈500 to 740 nm, corroborating that the plasmon mediated absorption enhancement can be translated into excess photogenerated charge carriers. Noticeably, the enhancement in IQE follows a similar trend to the EQE, which we primarily attribute to the improved charge carrier generation rate that is observed in close proximity to the silver nanoparticles (Fig. 5.3).

Adding silver nanoprisms, however, only benefits the OPV device performance for very thin (<50 nm) P3HT:PCBM blends, as illustrated in Fig. 5.4(c). Importantly, the optical and electronic losses associated with silver nanoparticles degrade the performance of thicker devices, and the bare polymer absorption for films >50 nm outperforms the benefits associated with the presence of the silver nanoparticles.

To further understand the device performance, we studied the impact of the work function of the silver nanoprisms (χ_{Ag}) on the current-voltage relation. Fig. 5.5(a) shows the calculated I-V plots for different work functions of the silver nanoprisms, in which the anode voltage at the ITO is swept from 0 to 0.8 V. The S-shaped I-V behavior at high work functions ($\chi_{\mathrm{Ag}} > 4.7$ eV) is due to a strong dipole-induced electric field, as illustrated in

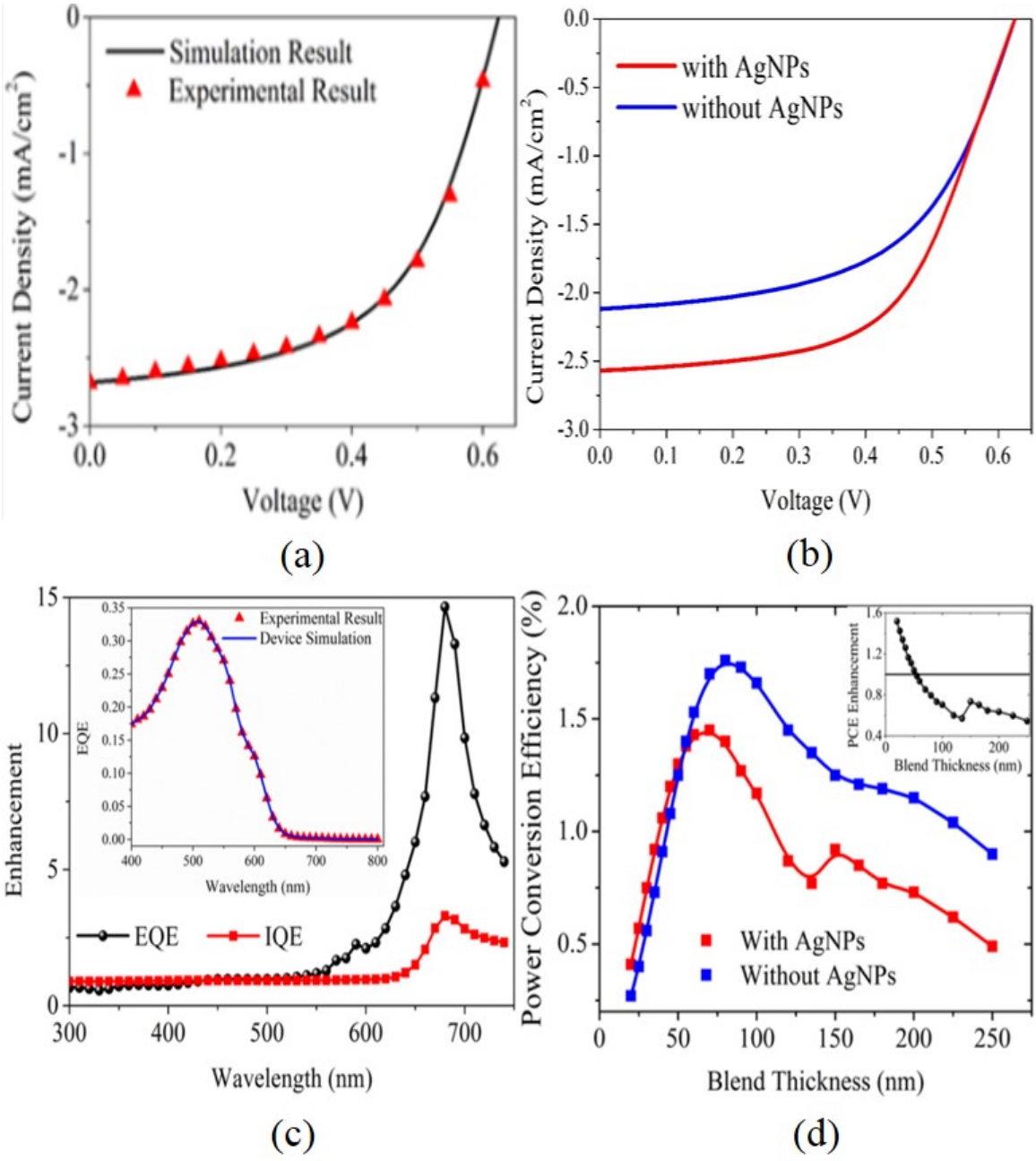

Figure 5.4: (a) fits to experimental I-V and EQE spectra for a reference device without nanoprisms (40-nm active layer thickness); (b) Calculated I-V plots; (c) external (EQE) and internal quantum efficiency (IQE) enhancements for a 35-nm active layer OPV with and without the presence of silver nanoprisms (work function $\chi_{\mathrm{Ag}} = 4.5$ eV). The insets in (c) show fits to experimental EQE spectra for a reference device without nanoprisms (40-nm active layer thickness); (d) represents the calculated power conversion efficiency (PCE) for OPVs with and without silver nanoprisms as a function of the active layer thickness. The inset in (d) shows the enhancement in PCE vs. active layer thickness. The lines in (d) are guides to the eye.

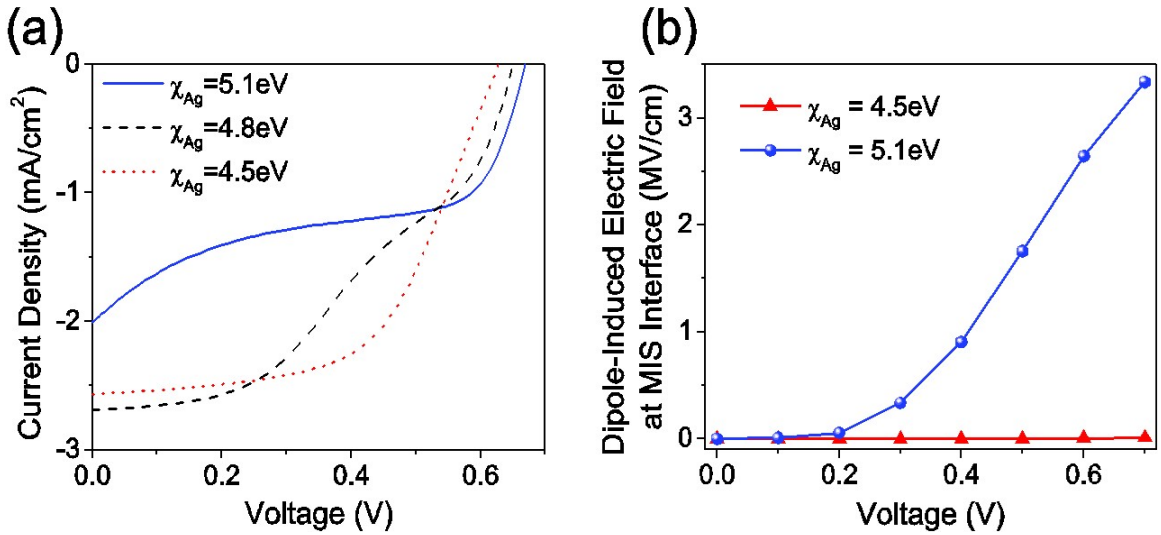

Figure 5.5: (a) Current-voltage plots for 35-nm plasmonic P3HT:PCBM OPVs for different work functions of the AgNPs; (b) Strength of the dipole-induced electric field at the metal-insulator-semiconductor interface for χ_{Ag} = 4.5 eV and 5.1 eV.

Fig. 5.5(b).

The AgNPs, the thin dielectric layer, and the P3HT:PCBM film form a classical metal-insulator-semiconductor (MIS) structure. At a low effective insulator barrier height ($q\Phi_T$), under small forward bias, the dominant current is the minority-carrier (electron) current, while under a high barrier height, the dominant current is the majority carrier (hole) tunneling current from the P3HT:PCBM valence band into the AgNP, which is 3 orders of magnitude larger [16]. The resulting accumulation of holes causes an extra dipole field at the MIS interface (Fig. 5.6) and reduces the current density substantially [128]. This phenomenon may explain reduced fill factors and V_{oc} previously observed in plasmonic OPV behavior [129]. By reducing the work function of the silver surface, one can effectively suppress charge accumulation at the MIS interface, thus improving the I-V behavior and, therefore, the overall OPV performance.

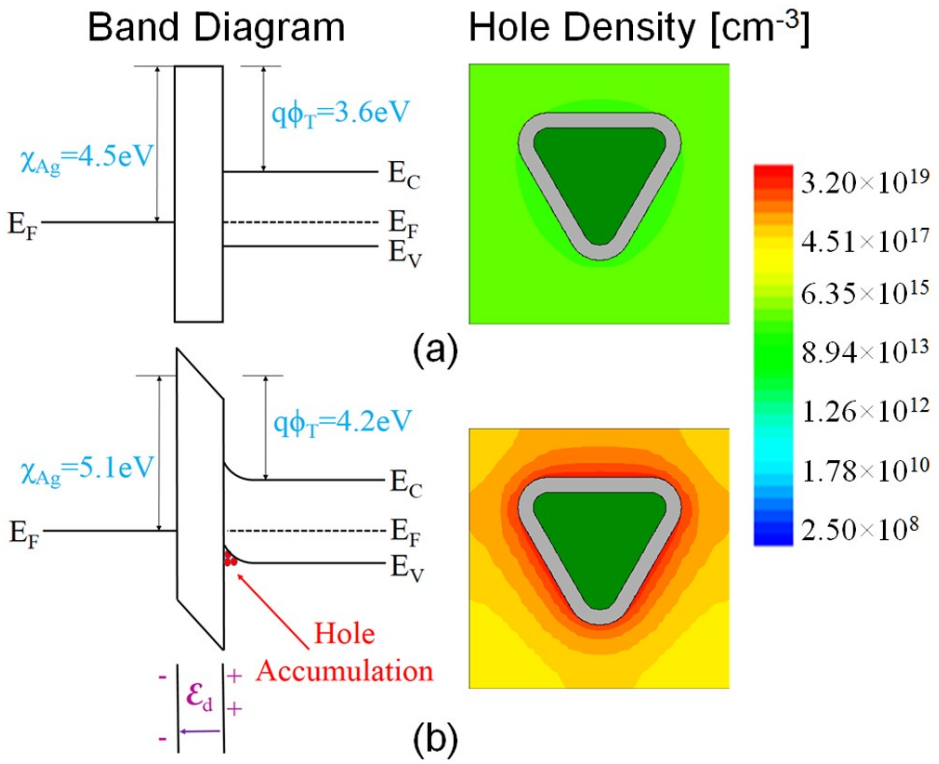

Figure 5.6: Scheme of the energy band diagram and concentration of holes in the P3HT:PCBM blend near AgNPs for (a) $\chi_{Ag} = 4.5$ eV and (b) $\chi_{Ag} = 5.1$ eV. The energy band diagram is extracted directly from the device calculations (C: conduction band, F: Fermi level, V: valence band).

5.4 Summary

In summary, we identified a trade-off between plasmon mediated optical enhancement and optical and electronic losses associated with low aspect ratio silver nanoprisms in plasmonic organic solar cells. In a regime of low polymer absorption (sub-50 nm thickness), plasmon enhancement dominates, leading to improvements in OPV device performance of up to 26%. For thicker active layers ($>$ 50 nm), the optical and electronic losses become relevant and the polymer absorption outperforms the optical antenna effect. These results may infer that previously observed enhancements in thicker active layer devices are partially due to non-optical effects. More generally, our calculations show that the fill factor and V_{oc} critically depend on the work function of the metal nanoparticle due to the occurrence of strong tunneling currents and charge accumulation. As such, the plasmon resonance, the work function, and the dielectric shell thickness need to be carefully tuned for the near-field and far-field enhancement effects to optimally benefit OPV performance. The simulation framework presented here may inform strategies for designing silver nanoparticles as optical antennas in ultra-thin OPVs and can be easily adapted for optimizing plasmonic enhancement in other device geometries and using other material combinations.

Chapter 6

HIGH-FIELD CHEMISTRY OF ATOMIC FORCE MICROSCOPY

Fabricating integrated multi-material structures with nanoscale accuracy is a challenging pursuit essential for advances in electronics and photonics. Atomic force microscopy (AFM) can precisely control the synthesis of nanostructures by triggering chemical reactions with the tip at determined substrate locations. Using a biased atomic force microscope tip, researchers have recently demonstrated the localized synthesis of germanium and silicon nanostructures from organometallic liquid precursors. Here, we attempt to understand the reactions occurring during this synthesis by establishing a reaction pathway for the AFM field-induced direct write. Reactions for both diphenylgermane and diphenylsilane precursors are triggered by field-emitted electrons that help to fragment the precursor molecules into the desired products. We conducted electronic device simulations to understand why the synthesis of germanium is more favorable than the synthesis of silicon nanostructures. By including the Fowler-Nordheim type of tunneling mechanism in presence of extremely large electric field concentration around the AFM tip, we match the negative ion density profile with experimentally measured nanostructure profile well. Furthermore, by investigating the peak ion density dependence on deposited thickness of nanostructures, we derived an equation that relates nanostructures′ deposition rate with the AFM tip direct writing speed. This simulation framework may serve as baseline for designing new semiconductor nanostructures via the direct write capability of atomic force microscopy[1].

6.1 Overview

The combination of multi-material top-down [132, 133, 134] and bottom-up [135, 136, 137, 138] nanostructures will likely play a key role in future electronic and photonic devices

[1]This chapter is adapted from two papers which were published in *Phys. Chem. Chem. Phys.* and *J. Mater. Chem. C* [130, 131].

[139]. In the bottom-up approach, nanostructures are shaped by confining the synthesis of the material of choice into a specified volume. For optimal device integration, the placement and the orientation of this confined synthesis needs to be precisely controlled [140]. Scanning probe microscopy, such as the atomic force microscopy (AFM), confine chemical reactions at the nanoscale through the delivery of specific stimuli [141] or reactants [142] to a small area of the sample surface. Macroscale reactions such as click chemistry [143], galvanic displacement [144], and Diels-Alder [145] coupling are confined to produced patterns with well-defined chemistry [145, 146]. Nanoscale thermochemistry with heated probes creates 2D and 3D patterns in reduced graphene [147], polymeric resists [148, 149], and macromolecular resists [150]. Using a DC voltage, nanoscale patterning of ferroelectric domains in organic substrates has been demonstrated [151]. In the presence of a water meniscus, field-induced electrochemistry with a biased tip results in the oxidation or the reduction of conducting substrates [152, 153, 154, 155] and organic monolayers [156, 157]. When the water is substituted with an organic or inorganic precursor, the high electric field [158] induced by the biased AFM probe and the resulting field emitted electrons broaden the available reactions. These reactions include the activation of self-assembled monolayers [159, 160, 161], the cross-linking of polymers [162], the polymerization of sulfur [163], and the localized synthesis of carbon nanostructures [164, 165, 166, 167, 168]. Recently, the AFM localized synthesis of germanium and silicon nanostructures has been demonstrated from diphenylgermane (DPG) and diphenylsilane (DPS) liquid precursors [169, 170]. While the mechanism for AFM induced electrochemistry is well established [171], the mechanism for these field-induced chemical reactions has been discussed only recently for carbon deposition [172, 173]. Few initial insights have been proposed for the AFM field-induced direct write of germanium nanostructures [130]. In this paper, we describe experiments and simulations to further understand the reaction mechanism of diphenylgermane and diphenylsilane for the AFM field-induced direct write of semiconductor nanostructures.

6.2 Electronic Structure of DPG/DPS Molecules

In AFM field-induced direct write, a biased AFM tip traces desired shapes along the silicon substrate in presence of DPG or DPS (Fig. 6.1(a) (b)). In this fashion, germanium and

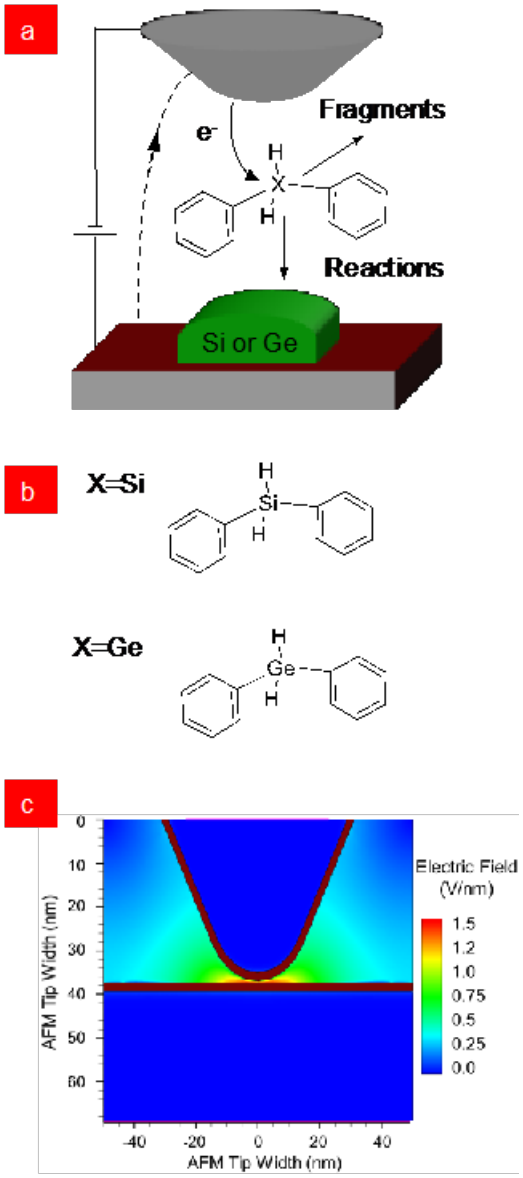

Figure 6.1: AFM Direct Write Schematic of the probe sample geometry and deposition process for AFM direct-write. A moderate sample bias (≈12V) induces a large electric field (>1 V/nm) (a). Electrons tunnel from the tip into the precursor molecule, where X = Ge or Si (b), and cause the fragmentation of the precursor and deposition of the desired product. (c). Electric field simulation for the AFM direct write process.

silicon nanostructures are written on the silicon substrate. The formation of germanium and silicon nanostructures suggests that the two precursors DPG and DPS likely undergo a similar reaction pathway. The rate of germanium and silicon nanostructure deposition is different and indicates that the kinetics of field-induced chemical reactions are precursor dependent. Here, we utilize DPG and DPS as model precursors to probe the mechanisms of germanium and silicon AFM field-induced direct write.

To better understand AFM field-induced direct write, we first consider the environment in the tip-sample proximity. In this area, even a moderate 10 V bias induces an electric field with peaks above 1 V/nm (Fig. 6.1(c)). This high field causes the emission of electrons from the AFM tip via Fowler-Nordheim tunneling (Fig. 6.2(c) Step 1). From reaction kinetics, we propose that some of the field emitted electrons pass directly to the substrate without interacting with the precursor molecules (Fig. 6.2(c) Step 2). However, electrons also drop into the LUMO of the precursor molecule and form a temporary negative ion (TNI) [130] (Fig. 6.2(c) Step 3), which upon further fragmentation will result in the germanium or silicon nanostructures. The TNI or subsequent charged fragments are attracted by the electric field gradient towards the tip-sample interface. This phenomenon is consistent with the results from STM chemical vapor deposition using gaseous precursors [174]. The electric field also influences the shape of the HOMO of the precursor molecules (Fig. 6.3). In the absence of an electric field, the electron density of the HOMO is distributed across both phenyl groups and the inorganic species. With an applied electric field of 4 V/nm, the electron density becomes confined primarily to a single phenyl group.

6.3 Device Simulation and Tunneling Model

The onset of Fowler-Nordheim tunneling into the precursor is related to the position of the energy levels of the precursor molecule. In our system, the precursor molecules form a liquid. We treat this liquid as a molecular liquid with an associated valence band and conduction band (Fig. 6.5(a)). This treatment is supported by the red shift observed in the UV-VIS data for the DPG and DPS neat with respect to the DPG and DPS dissolved in acetonitrile. This red shift, suggests that the $\pi-$electrons from the phenyl groups of the precursors are partially delocalized throughout the liquid. There is no published data for

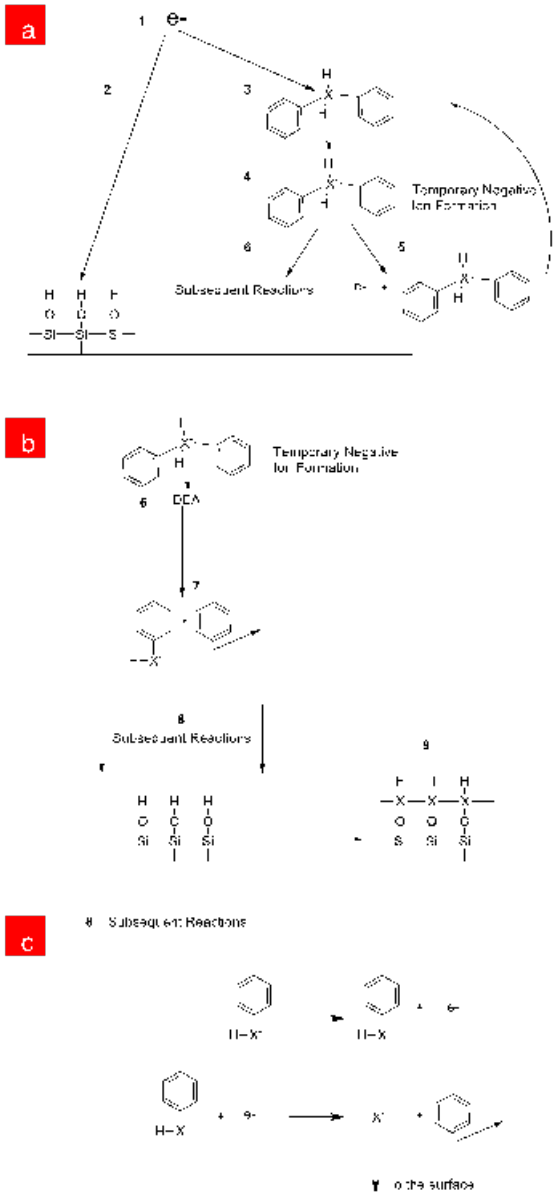

Figure 6.2: Generalized diagram of DPX breakdown pathways in the tip-sample gap. Electrons are field-emitted from the AFM tip (a1) and either continue into the Si wafer (a2) or are captured by a DPX molecule (a3), forming a TNI (a4). The TNI undergoes autodetachment of the electron (b5) or fragment via one of several dissociative electron attachment pathways (b6,7). Once the TNI has undergone fragmentation, it will undergo further reactions (b,c8), ultimately leading to the nanostructure formation (b9).

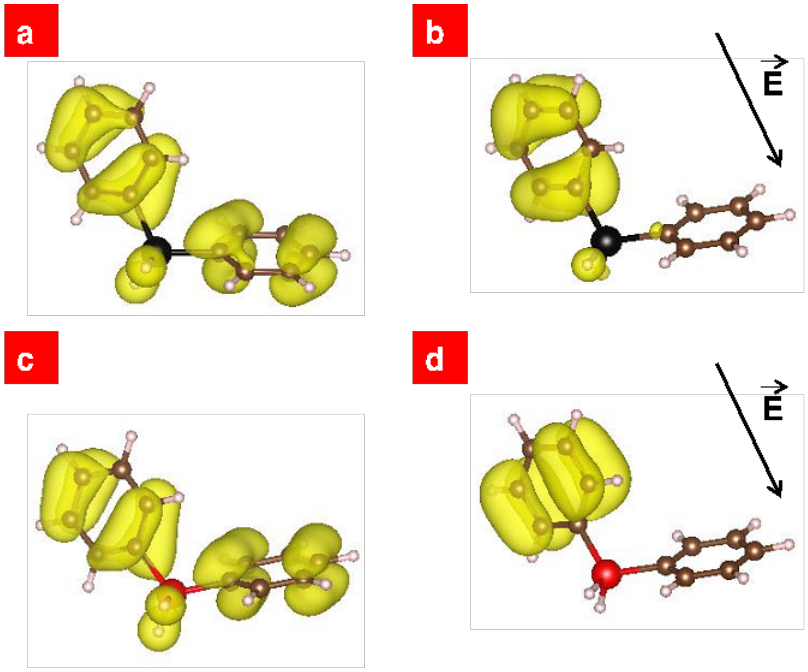

Figure 6.3: Molecular Orbital Charge Simulation. VASP simulations of the HOMO with cell size 2.5 nm x 2.5 nm x 2.5 nm for DPG and DPS (a,c) with no external electric field and with an external electric field of 4 V/nm (b,d DPG and DPS respectively). The direction of the electric field is indicated by the black arrow.

the precise position of the valence band and the conduction band of DPG and DPS. We estimate the band structure of DPG and DPS (Fig. 6.5(b)) by combining the published data for the ionization potential (IP) and the experimentally determined optical band gap of the DPG and DPS liquids (SI, Fig1). These data yields the values for the electron affinity (EA), which is the energy of the bottom of the conducting band. The literature value of the gas phase ionization potential (IP) for DPS is 9.23 eV [175]. Data for the IP of DPG does not exist in the literature. However, the IP of the similar compounds triphenylgermane and triphenylsilane are equal [175]. It is thus reasonable to estimate the IP of DPG to be comparable to the IP of DPS. From UV-Vis spectroscopy (SI, Fig.1), the optical band gap for DPG and DPS are = 4.2±0.2 eV and 4.3±0.3 eV, respectively. The data for DPG is in agreement with what was previously published [176]. Using the optical band gap data in

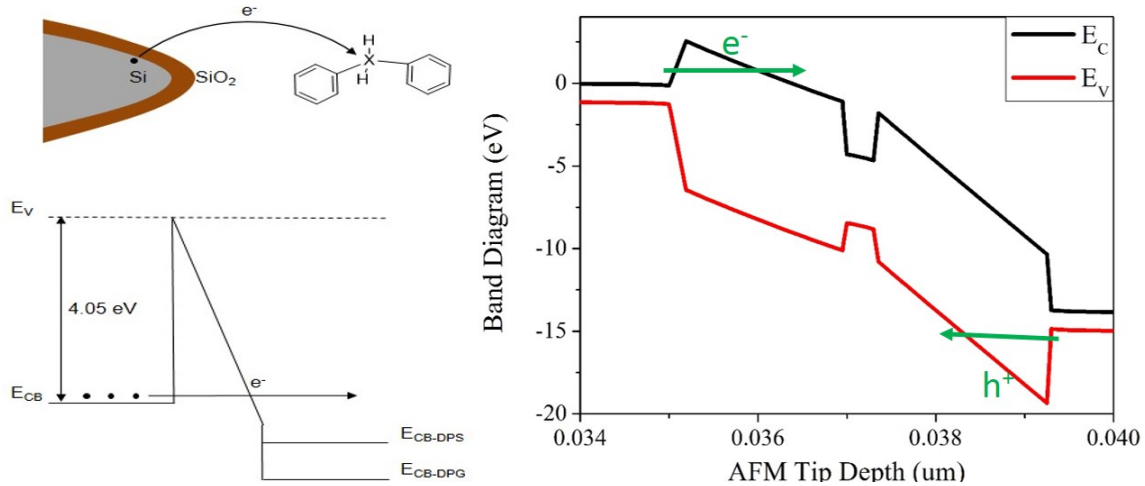

Figure 6.4: (a). Fowler-Nordheim tunneling process schematic. The applied electric field lowers the barrier for an electron in the Si to tunnel through the potential barrier of the oxide. In our proposed model, the field-emitted electron tunnels into the LUMO of the DPX molecule. Because the LUMO of DPG is lower in energy than that of DPS, the onset voltage for tunneling is expected to be lower.

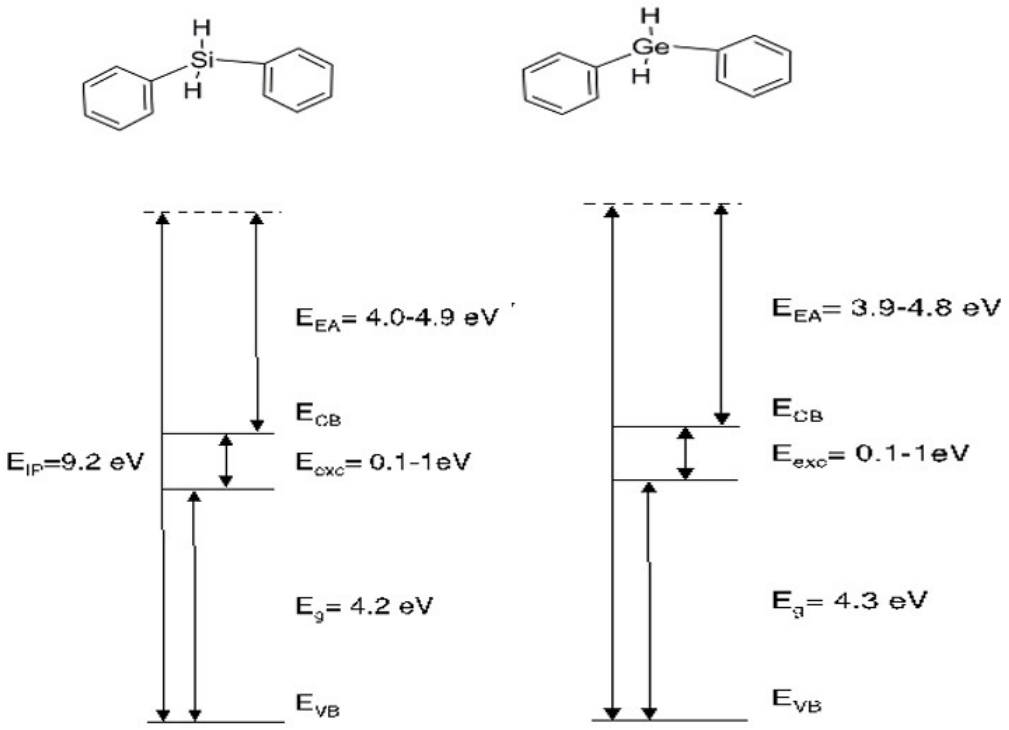

Figure 6.5: (b) Band diagram for diphenylsilane (right) and diphenylgermane (left). The HOMO-LUMO gap was determined using UV-Vis spectroscopy. From a combination of literature and experimental values, we have determined the ionization potential (IP) and electron affinity (EA) of each molecule.

conjunction with an exciton binding energy correction (0.1-1 eV) [177] and the literature IP value, the EA are determined to be 3.9-4.8±0.3 eV for DPS and 4.0-4.9±0.2 eV for DPG. All the materials' parameters used in the device simulation are listed in Table 6.1.

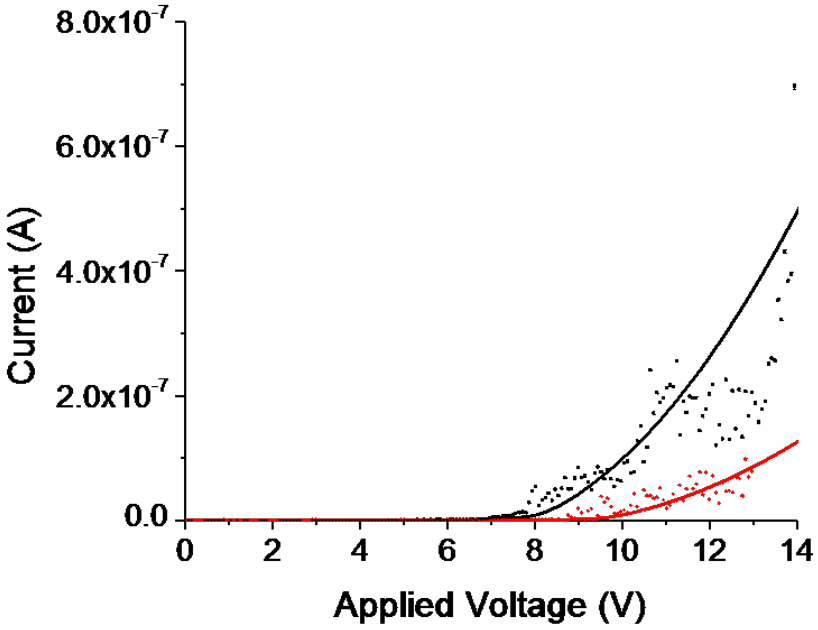

Figure 6.6: DPG and DPS I-V Characteristics. Current versus applied voltage (measured positive on the sample) obtained via an averaged IV sweep with a stationary tip for diphenylgermane (black) and diphenylsilane (red) on an HMDS-treated surface. Current measurements were taken using a condensed meniscus of inorganic vapor at voltages near the onset voltage for DPG and DPS writing. Simulation of current between sample and tip including non-local tunneling model using a structure matched to experimental conditions (solid line).

To test the tunneling step and the predicted difference in onset voltage for DPG and DPS, we measure the current across the tip-sample interface with a stationary tip and a function of applied voltage (Fig. 6.6). From this data, the onset voltage for diphenylgermane is estimated as 7±2 V, while the onset voltage for diphenylsilane molecule is 9±2 V. The difference in onset voltages indicates that higher energy may be need for TNI formation with the DPS molecule. The observed difference in onset voltages is larger than that predicted by

Table 6.1: Device Simulation Parameters for AFM Direct Write

Parameter Name	Parameter Symbol	Parameter Value
Silicon relative permittivity	ϵ_r^{Si}	11.7
Silicon electron affinity	χ^{Si}	4.05 eV
Silicon bandgap	E_g^{Si}	1.16964 eV
Silicon effective DoS in Gaussian LUMO level	N_e	$2.89 \times 10^{19} cm^{-3}$
Silicon effective DoS in Gaussian HOMO level	N_h	$3.14 \times 10^{19} cm^{-3}$
Silicon electron mobility	μ_e^{Si}	1.417×10^3 $[cm^2/(V \cdot s)]$
Silicon hole mobility	μ_h^{Si}	4.705×10^3 $[cm^2/(V \cdot s)]$
Silicon barrier tunneling effective mass	m_t^{Si}	0.5 m_0
Silicon barrier tunneling Richardson constant	g_e	2.1
Silicon barrier tunneling Richardson constant	g_h	0.66
SiO_2 relative permittivity	$\epsilon_r^{SiO_2}$	3.9
SiO_2 electron affinity	χ^{SiO_2}	0.9 eV
SiO_2 bandgap	$E_g^{SiO_2}$	9 eV
SiO_2 barrier tunneling effective mass	m_t^e	0.5 m_0
SiO_2 barrier tunneling effective mass	m_t^h	3 m_0
DPG electron affinity	χ^{DPG}	4.3 eV
DPG bandgap	E_g^{DPG}	4.3 eV
DPS electron affinity	χ^{DPS}	4.4 eV
DPS bandgap	E_g^{DPS}	4.2 eV

the difference in electron affinity between DPG and DPS. On the other hand, the mobility of negatively charged precursor molecules also impacts the onset voltage for DPG and DPS dramatically. A smaller value of mobility results in a higher external voltage required for the precursor molecules to move between the AFM tip and the silicon substrate. Simulations match experimental data when the calculated energy levels are used with a factor of 4 difference in negative charge carrier mobility by $\left(4 \times 10^{-6}\text{vs.}1 \times 10^{-6}\text{m}^2/(\text{V} \cdot \text{s})\right)$ for DPG and DPS respectively. Further investigation for the reasons behind this difference in negative charge carrier mobility is required.

The next step in the proposed reaction pathway is the fragmentation of the temporary negative TNI into other reactants. TNIs decay by auto-emission of the captured electron (Fig. 6.2(c) Step 5) and dissociative electron attachment (DEA) (Fig. 6.2(c) Step 6) [162]. Similar to the direct tunneling from the AFM tip into the substrate, auto-emission does not result in deposition. The auto-emitted electron either tunnels through the substrate oxide into the substrate Si or interacts with another precursor molecule. After auto-emission, the DPG or the DPS molecule returns to the reaction feedstock where it can undergo further reactions with field emitted electrons. In dissociative electron attachment, the TNI decays into a negatively charged and one or several neutral fragments (Fig. 6.2(c) Step 7) [162, 178]. It is difficult to precisely measure how long it takes the TNI to decay into the fragments that react to form the nanostructures. Writing on different substrates provides insights. Growth of features is not observed on metal surfaces with voltages in the range used for writing (0-20 V). At first, this observation is surprising because a more conducting substrate results in higher current and an expected higher nanostructure growth rate. However, on the more conducting metal surface, the auto-emission pathway and the electron tunneling into the substrate is favored, which does not result in nanostructure growth. On silicon, the surface native oxide layer ($\approx$ 2nm) reduces electron transfer into the substrate and the auto-emission rate. This lower auto-emission rate increases the TNI lifetime and the chances for the TNI to dissociate into the reactive fragments that form the nanostructures.

To further understand the nanostructure writing process for different precursors, we have produced features with different bias voltages (Fig. 6.7(a)-(k)). To minimize the effects of the growth material accumulating under the tip, we translate the tip at a constant rate (1

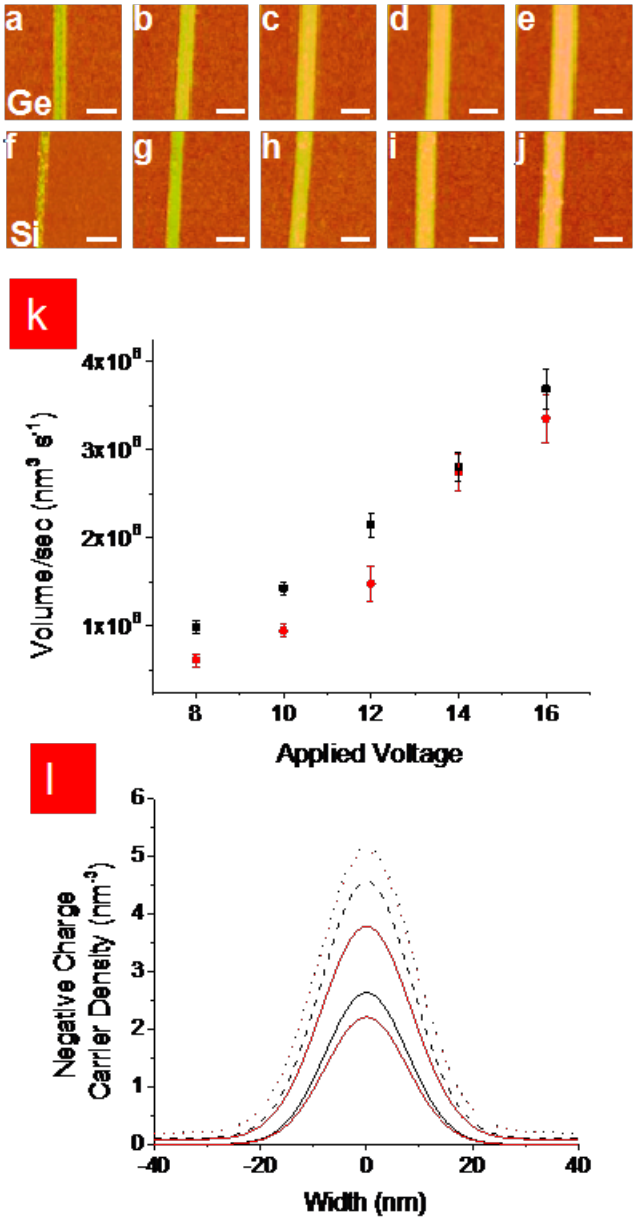

Figure 6.7: AFM Direct Write Comparison for DPG and DPS. Comparison of lines fabricated from DPG and DPS (top and bottom) at applied voltages of 8 (a,f), 10 (b,g) , 12 (c,h), 14 (d,i), and 16 V (e, j) from L to R (a). Lines deposited at a write speed of 1 μm/s. Scale bar = 250 nm, height scale from brown to bright yellow = 10 nm. To minimize tip convolution effects, the images were recorded in air in tapping mode with a new tip (r$\approx$10 nm). Comparison of volume of lines fabricated from DPG (black squares) and DPS (red circles) (k). Comparison of width and negative charge carrier density for DPG (black) and DPS (red) at 10V (solid), 12V (dashed) and 14V (dotted)(l).

μm/s) while writing lines on the sample. To minimize tip convolution effects, the images were recorded in air in tapping mode with a new tip (r $\approx$ 10nm). This writing study was performed at voltages within the threshold range, but below voltages that contribute to irregular features and small explosive discharges [179, 180]. As expected, for each precursor, the heights and widths of the lines increase with applied voltage. Deposited volume was calculated from height, width, and write speed as a function of voltage bias for the two precursors. For voltages near the onset writing voltages, small differences between the deposited volumes are observed. Above $\approx$12V, the deposited volume of the precursors becomes comparable, indicating that for higher applied voltages, the breakdown pathway becomes similar. Continuum simulations of the charge carrier density versus nanostructure width were performed (Fig. 6.7(l)). These simulations indicate the width of the structures increasing with increasing voltage. With higher external voltage, a larger range of liquid region is subject to the extremely large electric field, which enables more electrons with high energy to tunneling from AFM tip into the DPG/DPS liquid.

6.4 Analytical Model for Nanostructure Deposition Height vs. AFM Direct-Writing Speed

The negative charge carrier density profile shown in Fig. 6.7(i) can be fitted with Gaussian function quite nicely. Take the DPS deposition profile at 10 V in Fig. 6.7(i) as an example, the charge carrier density can be fitted as:

$$n = e^{0.795-0.0084x^2} \approx 2.21 \cdot e^{-\frac{x^2}{2\times 7.7^2}} \tag{6.1}$$

where n is the negative charge carrier density measured in nm^{-3}, and x is the lateral width measured in nm.

Since the nanostructure deposition rate is proportional to the negative charge carrier density, we can write the nanostructure deposition rate as a 2-D Gaussian density function (in x- and y- direction) in general:

$$r(x,y) = A \cdot e^{-\frac{(x-x_0)^2+(y-y_0)^2}{2\sigma^2}} \tag{6.2}$$

where σ is the deposition rate spread in space that can be determined experimentally.

One nice property of Gaussian density function is that if you integrated in y-direction, the remaining function is still a 1-D Gaussian function in the x-direction:

$$\begin{aligned} r(x) &= \int_{-\infty}^{\infty} r(x,y)\mathrm{d}y \\ &= \int_{-\infty}^{\infty} A \cdot e^{-\frac{(x-x_0)^2+(y-y_0)^2}{2\sigma^2}}\mathrm{d}y \\ &= A_1 \cdot e^{-\frac{(x-x_0)^2}{2\sigma^2}} \end{aligned}$$

For a moving AFM tip with speed v along the x-axis, the nanostructure deposition rate r at position x_0 is proportional to:

$$r(v) \propto e^{-\frac{(x_0-vt)^2}{2\sigma^2}} \tag{6.3}$$

To determine the dependence of maximal deposition rate on the thickness of Si/Ge nanostructure beneath the AFM tip, we conducted 2D device simulation. Fig. 6.8 illustrates the relation between the peak values of negative ion density and the height of already-deposited Si/Ge nanostructures beneath the AFM tip during direct write. We can fit the calculated results using exponential equation:

$$n(D) = k_1 e^{-k_2 D(t)} \tag{6.4}$$

where D(t) is the thickness of nanostructures below the AFM tip, $k_1 \approx 2.23 \times 10^{21}\mathrm{cm}^{-3}$ and $k_2 \approx 2.27$ are two fitting parameters.

Again, since the nanostructure deposition rate is proportional to the negative charge carrier density, the nanostructure deposition rate is then proportional to:

$$r(D) \propto c_1 e^{-k_2 D(t)} \tag{6.5}$$

where D(t) is the thickness of nanostructures below the AFM tip at the time t when the AFM tip is just above.

Comparing Eq. 6.3 with Eq. 6.5, we can write the nanostructure deposition rate r as a function of instantaneous nanostructure height D(t) and AFM tip writing speed v:

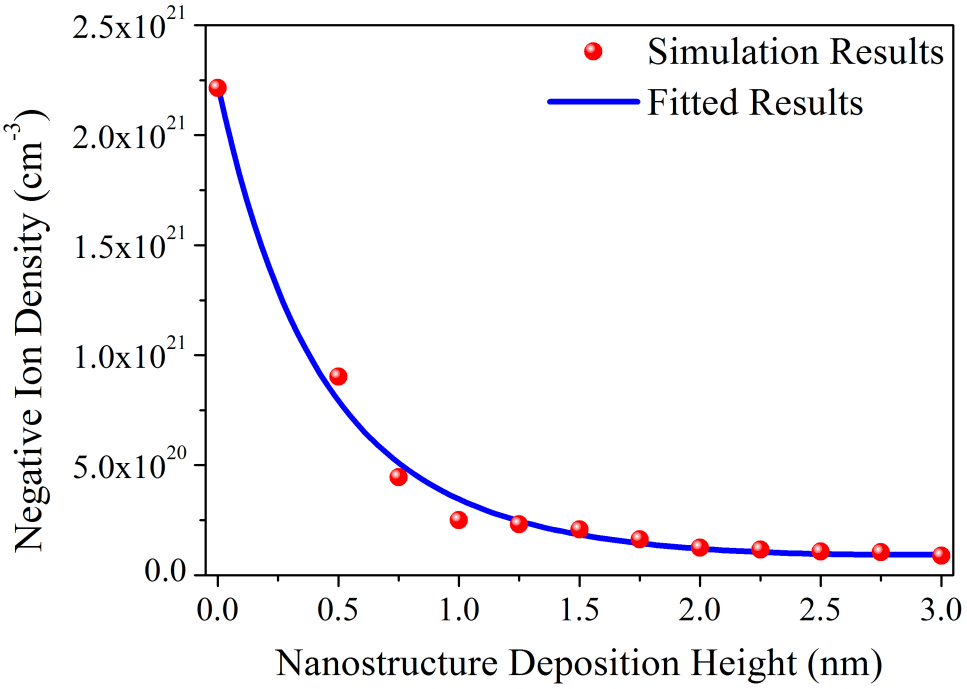

Figure 6.8: Negative charge carrier density vs. thickness of nanostructure (Si or Ge) beneath the AFM tip.

$$r(D(t), v) = c_1 e^{-k_2 D(t)} e^{-\frac{(x_0 - vt)^2}{2\sigma^2}} \tag{6.6}$$

Without loss of generality, we set $x_0 = 0$. So the nanostructure deposition rate r is then:

$$r(D(t), v) = c_1 e^{-k_2 D(t)} e^{-\frac{(vt)^2}{2\sigma^2}} \tag{6.7}$$

The instantaneously deposited nanostructure height, d[D(t)], is then:

$$\mathrm{d}[D(t)] = r(D(t), v)\mathrm{d}t = c_1 e^{-k_2 D(t)} e^{-\frac{(vt)^2}{2\sigma^2}} \mathrm{d}t \rightarrow e^{-k_2 D(t)} \mathrm{d}[D(t)] = c_1 e^{-\frac{(vt)^2}{2\sigma^2}} \mathrm{d}t \tag{6.8}$$

We then integrate the left and right parts of Eq. 6.8:

$$\int_0^D e^{-k_2 D(t)} \mathrm{d}[D(t)] = \int_0^\infty c_1 e^{-\frac{(vt)^2}{2\sigma^2}} \mathrm{d}t \rightarrow \frac{1}{k_2}\left(e^{k_2 D} - 1\right) = \frac{c_1 \sigma}{v}\sqrt{\frac{\pi}{2}} = \frac{K\sigma}{v} \tag{6.9}$$

Thus, the final expression for the nanostructure deposition height, D, can be expressed as a function of AFM direct writing speed, v:

$$D = \frac{1}{k_2} ln\left(\frac{K\sigma}{v} + 1\right) \tag{6.10}$$

The advantage of this simple expression of nanostructure deposition height D in Eq. 6.10 is that k_2 and σ can be measured either from simulation or experiments, leaving only one parameter, K, to fit. For the case of DPS direct writing at 10V, D = 2.017 nm, σ = 7.7 nm, k_2 = 2.27, v = 1.0 μm/s, so the fitting parameter K = 1.24×10^4 s^{-1}.

For a static AFM tip, Eq. 6.10 diverges. However, if we re-investigate Eq. 6.7 from the beginning, at v=0, we have:

$$r(D(t), v) = c_1 e^{-k_2 D(t)} e^{-\frac{(vt)^2}{2\sigma^2}}|_{v=0} = c_1 e^{-k_2 D(t)} \tag{6.11}$$

So Eq. 6.8 becomes:

$$\mathrm{d}[D(t)] = r(D(t), v = 0)\mathrm{d}t = c_1 e^{-k_2 D(t)} \mathrm{d}t \rightarrow e^{-k_2 D(t)} \mathrm{d}[D(t)] = c_1 \mathrm{d}t \tag{6.12}$$

We can then integrate both sides of Eq. 6.12 over a finite amount of time:

$$\int_0^D e^{-k_2 D(t)} \mathrm{d}[D(t)] = \int_0^T c_1 \mathrm{d}t \rightarrow \frac{1}{k_2}\left(e^{k_2 D} - 1\right) = c_1 T \tag{6.13}$$

Thus, the final expression for the nanostructure deposition height, D, can be expressed as a function of deposition period, T:

$$D = \frac{1}{k_2} ln(c_1 k_2 T + 1) = \frac{1}{k_2} ln(KT + 1) \tag{6.14}$$

Based on Eq. 6.5 and 6.14, we conducted device simulation to compare the measured Si/Ge nanostructures deposition rate with the integrated density of temporary negative ion density from simulation as a function of applied voltage. As shown from Fig. 6.9, in which

the integrated density of temporary negative ion density from simulation is normalized according to measured Si/Ge nanostructures deposition rate at 10 V, the simulated deposition rate at 12 V and 14 V can be matched with experiments quite well. Note in particular that the model predicts the observed reduction of the deposition rate ratio between DPG and DPS at high tip voltage.

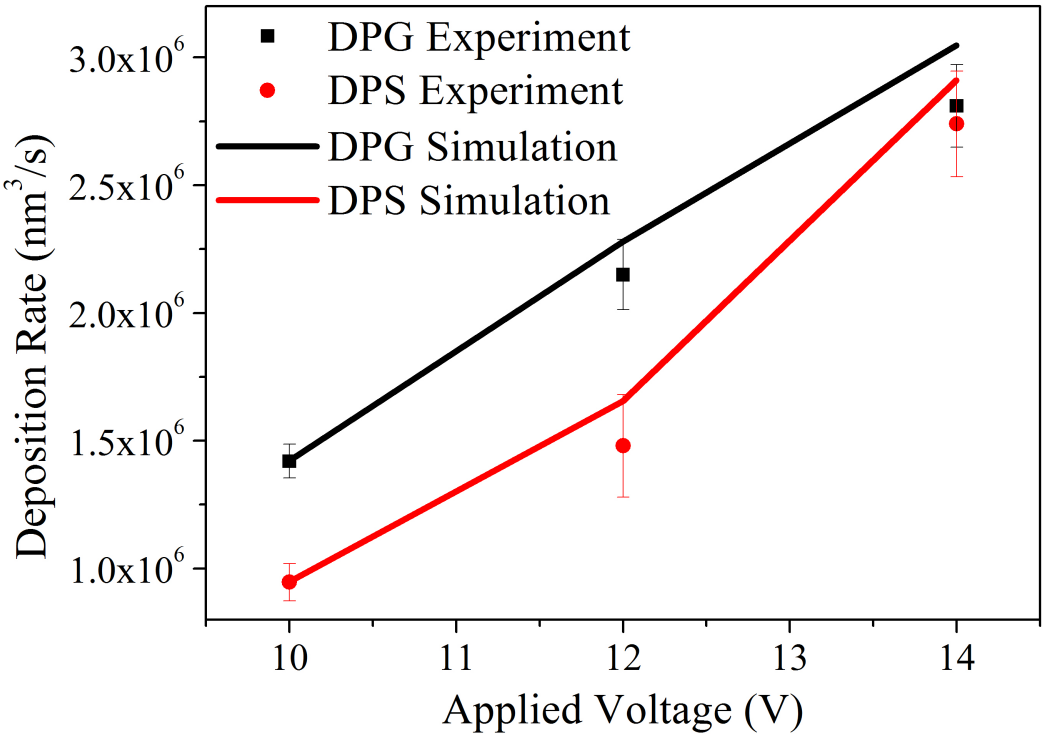

Figure 6.9: Comparison of Si/Ge nanostructure deposition rate as a function of applied voltage between experiments and simulation results. Simulation results are normalized based on the experimental results at 10 V.

6.5 Summary

In conclusion, we have established a reaction pathway for the AFM field-induced direct write of germanium and silicon nanostructures, and used as a basis for predictive models

of nanoscale material deposition. In this pathway, an electron is field-emitted from the AFM tip, tunnels into diphenylgermane or diphenylsilane precursor molecules, and forms a temporary negative ion. The temporary negative ion fragments via dissociative electron attachment to yield charged radicals which accumulate near substrate where they deposit to form germanium or silicon nanostructures. Differences in molecular energy levels and bonds strengths between diphenylgermane and diphenylsilane influence the reaction kinetics. In general, germanium nanostructures grow faster and at lower voltages than silicon nanostructures in similar conditions, which can be explained by the differences in electron affinity and bandgap of diphenylgermane and diphenylsilane molecules. We use Sentaurus Device simulator to build a device model that can capture the Fowler-Nordheim tunneling nature of the negative temporary ions in presence of huge electric fields. We also derive a simple but useful expression of the nanostructure's deposition depth dependence on the AFM tip writing speed. This work provides the basis to develop new processes and precursors for AFM field-induced direct write. These precursors can expand the variety of available nanostructure to other materials of interest such as compound semiconductors (III-V, II-VI) for optoelectronics applications and metals for substrates with enhanced optical properties.

Chapter 7

SUMMARY AND FUTURE WORK

In this dissertation, we described how multiphysics calculations can be used to develop physical models to better understand organic solar cells and atomic force microscope direct write. This chapter gives brief summaries of the main contributions in this dissertation, as well as suggestions for future work and a final conclusion.

7.1 Optics and Device Models

In Chapter 2, we first discussed the commonly used optics solvers such as transfer-matrix method (TMM), ray-tracing (RT), and finite-difference time-domain (FDTD) method. TMM and RT are relatively fast from the computational cost point of view, but can only deal with stratified (layered) medium or object size much larger than wavelength, respectively. The FDTD method solves the fundamental Maxwell′s equations thus has the capability to deal with any shapes and materials, but is computationally very expensive.

For device models, Poisson equation with electron/hole continuity equations are generally used for modeling electronic behavior of inorganic semiconductor devices. For devices with polymer materials, however, singlet exciton generation/dissociation equation and Poole-Frenkel mobility model also need to be included.

7.2 Main Contributions of Organic Solar Cell Study

(1) Developed continuum models to analyze incident photons and photo-generated charge carriers distribution within different layers of organic solar cell devices.

(2) Applied the FDTD simulation to optimize the design of triangular silver nano-prisms in the P3HT:PCBM absorber layer.

(3) Coupled optics and device simulation to predict solar cell performance such as short-circuit current (J_{SC}), open-circuit voltage (V_{OC}), maximum power density (P_{max}), and

fill-factor (FF) for various design of organic solar cells.

In Chapter 3, we explore the optimized active layer thickness and choices of using ultra-thin metals to replace ITO as transparent anode layer, with the aim of coupling light strongly into P3HT:PCBM layer while simultaneously reducing cost. Device simulation shows that silver layers thinner than 5 nm perform comparably to 100 nm ITO. We also explore the light enhancement due to the presence of nano-grating structure at cathode backcontact.

In Chapter 4, we conducted simulation as comparison with experimental measurements of the charge transport characteristics of P3HT:PCBM material between lateral nanogap electrodes. By using Gaussian-disorder mobility model which suggests a temperature- and field-dependent mobility in P3HT:PCBM material, we showed negative mobility trend with decreasing nanogap spacing to be a result of the accumulation of space charges between nanogaps which reduce the impact from external electric field.

In Chapter 5, we investigated silver nano-prism enhanced organic solar cells by coupling three-dimensional electromagnetic and electronic device simulations. For active layer thickness of less than 50 nm, an optimized silver nano-prism can enhance the power conversion efficiency (PCE) by more than 25% when embedded in P3HT:PCBM bulk heterojunction polymer blend. For thicker layers, optical losses due to the presence of nanoparticles still reduce the total PCE. By carefully tuning the work function of silver nano-prism, we reduce the tunneling current from organic semiconductor into silver nanoparticle, thus enhancing the short-circuit current up to 21%.

7.3 Main Contributions of Atomic Microscope Direct Write

(1) Proposed a reaction pathway (temporary negative ion) for the AFM field-induced direct write.

(2) Conducted electronic device simulation to illustrate Fowler-Nordheim type of tunneling mechanism in presence of extremely large electric field concentration around the AFM tip.

(3) Derived a simple equation to relate nanostructures′ deposition rate with the AFM tip moving speed.

(4) Compared Si/Ge nanostructure deposition rates as a function of applied voltage.

In Chapter 6, we established a reaction pathway for the AFM field-induced direct write of germanium and silicon nanostructures. The temporary negative ions (TNI′s) accumulate beneath the AFM tip and deposit onto silicon substrate to form Ge/Si nanostructures. We used Sentaurus device simulator to build a device model that illustrates the Fowler-Nordheim tunneling mechanism which only occurs in presence of huge electric field. Based on the device simulation results of the deposition thickness dependence of TNIs′ density around AFM tip, we derived a simple but useful expression that relates the nanostructures′ deposition thickness with the AFM tip writing speed. We also compared Si/Ge deposition rates based on different applied voltages, which match with experimental results well. This modeling framework serves as basis to develop new precursors for AFM direct write.

7.4 Suggestions for Future Work

7.4.1 Utilizing Plasmonic Enhancement to Improve Organic Solar Cells' Efficiency

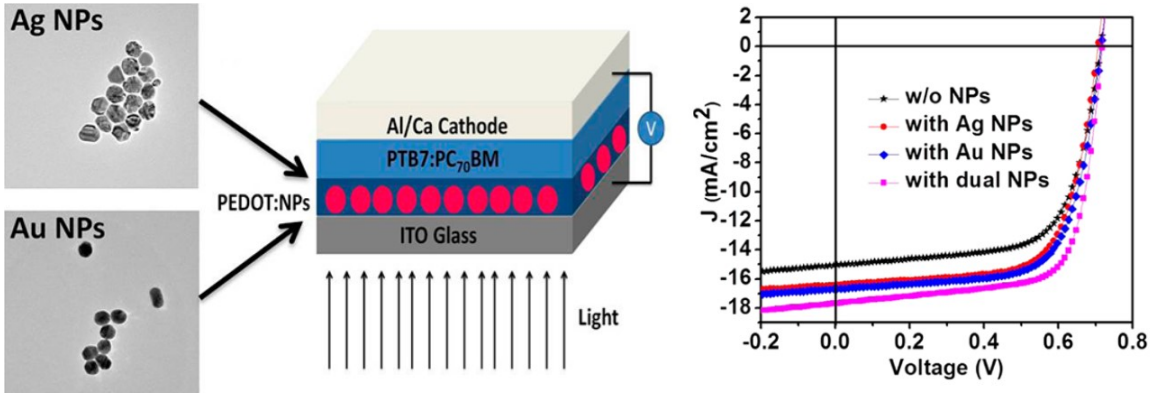

Figure 7.1: Enhancing organic solar cells performance via utilizing double-layered metal nano-rods.

(1) The nano-grating structure at metal backcontact needs to be optimized based on different choices of materials and device geometry.

(2) The coupled optics and device simulation results in Chapter 5 show the benefit from the usage of silver nano-prisms with the aim of enhancing P3HT:PCBM organic solar cells

is positive only at ultra-thin (film thickness $<$ 50 nm) OPV. For thicker light absorber films, adding the metal nanoparticles actually hurts the power conversion efficiency. It is of research interest to explore choices of materials and novel design of metal nanoparticles to build a plasmonic organic solar cell that benefits from the presence of metal nanoparticles. L. Lu et al from University of Chicago explored the enhancement of short-circuit current based on double-layered metal nano-rods for organic solar cells with PTB7 : $PC_{70}BM$ as light absorbing material [181]. It would serve as experimental basis for utilizing my simulation framework to optimize the structure and material choices of nano-rods (Fig. 7.1).

7.4.2 Model Calibration of Atomic Force Microscopy Direct Write

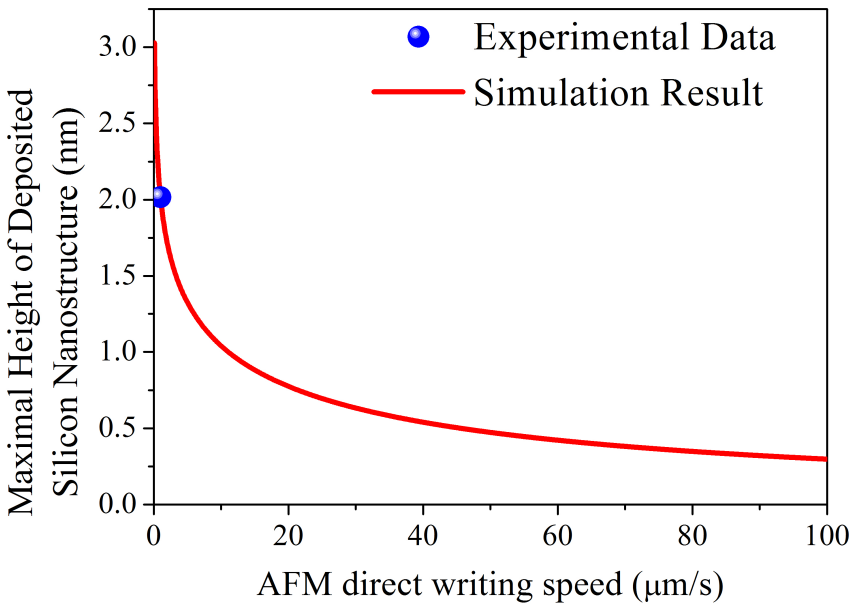

Figure 7.2: Silicon nanostructure deposition thickness as a function of AFM tip moving speed. The applied voltage is 10 V, and the AFM write speed is 1μm/s.

Fig. 7.2 illustrates the silicon nanostructure deposition thickness as a function of AFM tip writing speed based on the analytical model derived in Chapter 6. However, it needs to

be calibrated with experiments with different AFM write speed and applied voltage.

7.5 Final Conclusion

We have demonstrated the capability of TCAD multiphysics simulation tools to study the optics and device performance of two different semiconductor devices by utilizing a variety of modeling techniques (i.e., TMM, FDTD, and continuum device modeling approaches). TCAD tools are useful for determining the photon/charge carrier distribution in the organic photovoltaics and calculating the maximum power conversion efficiency under conditions which experiments are difficult to achieve. Device modeling together with analytical derivation are also useful for predicting the Si/Ge nanostructures deposition shape and thickness under various voltages and writing speeds. For the semiconductor industry, these tools have the potential of reducing the manufacturing costs and achieving better accuracy, thus providing guidance for new technology research and design.

BIBLIOGRAPHY

[1] S. Karg, W. Riess, V. Dyakonov, and M. Schwoerer *Snth. Metals.*, vol. 54, pp. 427–433, 1993.

[2] C. Tang *Appl. Phys. Lett.*, vol. 48, pp. 183–185, 1986.

[3] J. J. M. Halls, C. A. Walsh, N. C. Greenham, E. A. M. R. H. Friend, S. C. Moratti, and A. B. Holmes *Nature.*, vol. 376, pp. 498–500, 2002.

[4] N. R. E. Laboratory, "Solar cell efficiency chart," 2013.

[5] M. A. Green, K. Emery, Y. Hishikawa, and W. Warta *Prog. Photovolt: Res. Appl.*, vol. 19, pp. 84–92, 2011.

[6] F. J. Haug, T. Soederstroem, O. Cubero, V. Terrazzoni-Daudrix, and C. Ballif *J. Appl. Phys.*, vol. 104, p. 064509, 2008.

[7] F. C. Chen and Y. K. Lin *Appl. Phys. Lett.*, vol. 92, p. 023307, 2008.

[8] W. L. Ma, C. Y. Yang, X. Gong, W. H. Lee, and A. J. Heeger *Adv. Funct. Mater.*, vol. 15, pp. 1617–1622, 2005.

[9] L. M. Liu, W. E. Stanchina, and G. Y. Li *IEEE Nanotechnology Materials and Devices Conf. (NMDC 09)*, pp. 13–18, 2009.

[10] Y. M. Liu, T. Zentgraf, G. Bartal, and X. Zhang *Nano. Lett.*, vol. 10, pp. 1991–1997, 2010.

[11] J. F. Torrado, J. Gonzalez-Diaz, M. Gonzalez, A. Garcia-Martin, and G. Armelles *Opt. Express.*, vol. 18, pp. 15635–15642, 2010.

[12] M. D. Arnold and R. J. Blaikie *IEEE Nanoscience and Nanotechnology Conf. (ICONN 06)*, pp. 548–551, 2006.

[13] K. Okamoto, I. Niki, A. Shvartser, Y. Narukawa, T. Mukai, and A. Scherer *Nature Mater.*, vol. 3, pp. 601–605, 2004.

[14] S. Pillai, K. R. Catchpole, T. Trupke, and M. A. Green *J. Appl. Phys.*, vol. 101, p. 093105, 2007.

[15] H. A. Atwater and A. Polman *Nature Mater.*, vol. 9, p. 205, 2010.

[16] S. M. Sze and K. K. Ng, *Physics of Semiconductor Devices.* New York: Wiley-Interscience, 3rd ed.

[17] R. Tsu and L. Esaki *Appl. Phys. Lett.*, vol. 22, pp. 562 – 564, 1973.

[18] A. Gehring, *Simulation of Tunneling in Semiconductor Devices.* 2003.

[19] L. Savioja, "Modeling techniques for virtual acoustics," 1999.

[20] M. Born and E. Wolf, *Principles of Optics.* Cambridge University Press, 7th ed.

[21] O. Ozolins, V. Bobrovs, J. Porins, and G. Ivanovs, *Current Trends in Short- and Long-period Fiber Gratings.* 2013.

[22] A. Taflove and S. C. Hagness, *Computational Electrodynamics: The Finite-Difference Time-Domain Method.* Artech House Publishers, 3rd ed., 2005.

[23] S. Selberherr, *Analysis and Simulation of Semiconductor Devices.* Springer, 1984.

[24] U. Lindefelt *J. Appl. Phys.*, vol. 76, pp. 942–957, 1994.

[25] W. H. Lee, S. Y. Chuang, H. L. Chen, W. F. Su, and C. H. Lin *Thin solid films.*, vol. 518, pp. 7450–7454, 2010.

[26] F. Padinger, R. S. Rittberger, and N. S. Sariciftci *Adv. Funct. Mater.*, vol. 13, p. 85, 2003.

[27] W. Ma, C. Yang, X. Gong, K. Lee, and A. J. Heeger *Adv. Funct. Mater.*, vol. 15, p. 1617, 2006.

[28] R. Kroon, M. Lenes, J. C. Hummelen, P. W. M. Blom, and B. Boer *Polym. Rev.*, vol. 48, pp. 531–582, 2008.

[29] G. Li, V. Shrothiya, J. S. Huang, Y. Yao, T. Moriarty, K. Emery, and Y. Yang *Nature Mater.*, vol. 4, pp. 864–868, 2005.

[30] D. Zhang, K. M. Ryu, X. L. Liu, E. Polikarpov, J. Ly, M. E. Tompson, and C. W. Zhou *Nano Lett.*, vol. 6, pp. 1880–1886, 2006.

[31] H. Y. Chen, J. H. Hou, S. Q. Zhang, Y. Y. Liang, G. W. Yang, Y. Yang, L. P. Yu, Y. Wu, and G. Li *Nature Photon.*, vol. 3, pp. 649–653, 2009.

[32] W. Jiang and S. T. Dunham *Mater. Res. Soc. Symp. Proc.*, vol. 1270, pp. HH14–58, 2010.

[33] L. J. A. Koster, V. D. Mihailetchi, and P. W. M. Blom *Appl. Phys. Lett.*, vol. 88, p. 093511, 2006.

[34] H. Hoppe and N. S. Sariciftci *J. Mater. Chem.*, vol. 16, pp. 45–61, 2006.

[35] S. R. Scully, P. B. Armstrong, C. Edder, J. J. J. Frechet, and M. D. McGehee *Adv. Mater.*, vol. 19, pp. 2961–2966, 2009.

[36] J. Piris, T. E. Dykstra, A. A. Bakulin, P. H. M. Loosdrecht, W. Knulst, M. T. Trinh, J. M. Schins, and L. D. A. Siebbeles *J. Phys. Chem. C.*, vol. 113, pp. 14500–14506, 2009.

[37] V. J. Logeeswaran, P. K. Nobuhiko, P. Kobayashi, M. Saiflslam, W. Wu, P. Chaturvedi, N. X. Fang, S. Y. Wang, and R. S. Williams *Nano Lett.*, vol. 9, pp. 178–182, 2009.

[38] W. Zhang, B. Zhao, Z. He, X. Zhao, H. Wang, S. Yang, H. Wu, and Y. Cao *Energy Environ. Sci.*, vol. 6, pp. 1956–1964, 2013.

[39] H. Azimi, A. Senes, M. C. Scharber, K. Hingerl, and C. J. Brabec *Adv. Energy Mater.*, vol. 16, pp. 1162–1168, 2011.

[40] H. Bassler *Phys. Stat. Sol. (B)*, vol. 175, pp. 15–56, 1993.

[41] B. Bohnenbuck, E. von Hauff, J. Parisi, C. Deibel, and V. Dyakonov *J. Appl. Phys.*, vol. 99, p. 024506, 2006.

[42] Y. Roichman and N. Tessler *Appl. Phys. Lett.*, vol. 80, pp. 1948–1950, 2002.

[43] F. F. Stelzl and U. Wurfel *Phys. Rev. B.*, vol. 86, p. 075315, 2012.

[44] N. Tessler and Y. Roichman *Org. Electron.*, vol. 56, pp. 200–210, 2005.

[45] W. Shockley and W. T. Read *Phys. Rev.*, vol. 87, pp. 835–842, 1952.

[46] M. Kuik, H. T. Nicolai, M. Lenes, G.-J. A. H. Wetzelaer, M. Lu, and P. W. M. Blom *Appl. Phys. Lett.*, vol. 98, p. 093301, 2011.

[47] T. Kirchartz, B. E. Pieters, J. Kirkpatrick, U. Rau, and J. Nelson *Phys. Rev. B.*, vol. 83, p. 115209, 2011.

[48] R. C. I. MacKenzie, C. G. Shuttle, M. L. Chabinyc, and J. Nelson *Adv. Energy Mater.*, vol. 2, pp. 662–669, 2012.

[49] A. Foertig, J. Rauh, V. Dyakonov, and C. Deibel *Phys. Rev. B.*, vol. 86, p. 115302, 2012.

[50] T. A. Youngbull, M. Singh, W. Jiang, S. T. Dunham, S. A. Jenekhe, G. E. Jabbour, and C. K. Luscombe *ACS Nano.*, 2012.

[51] A. W. Hains, Z. Liang, M. A. Woodhouse, and B. A. Gregg *Chem. Rev.*, vol. 110, pp. 6689–6735, 2010.

[52] D. Cohen *New Scient.*, vol. 23, pp. 34–41, 2007.

[53] A. Feltrin and A. Freundlich *Renew. Energ.*, vol. 33, pp. 180–185, 2008.

[54] S. E. Shaheen, R. Radspinner, N. Peyghambarian, and G. E. Jabbour *Appl. Phys. Lett.*, vol. 79, p. 2996, 2001.

[55] J. K. Mapel, M. Singh, M. A. Baldo, and K. Celebi *Appl. Phys. Lett.*, vol. 90, p. 121102, 2007.

[56] M. Singh, H. M. Haverinen, P. Dhagat, and G. E. Jabbour *Adv. Mater.*, vol. 22, pp. 673–685, 2010.

[57] H. Y. Chen, J. Hou, S. Zhang, Y. Liang, G. Yang, Y. Yang, L. Yu, Y. Wu, and G. Li *Nature Photon.*, vol. 3, pp. 649–653, 2009.

[58] K. Technologies *World*, 2010.

[59] C. J. Brabec, N. S. Sariciftci, and J. C. Hummelen *Adv. Funct. Mater.*, vol. 11, p. 1526, 2001.

[60] M. Niggemann, M. Glatthaar, A. Gombert, A. Hinsch, and V. Wittwer *Thin Solid Films*, vol. 619, pp. 451–452, 2004.

[61] D. H. Wang, D. G. Choi, K. J. Lee, J. H. Jeong, S. H. Jeon, O. O. Park, and J. H. Park *Org. Electron.*, vol. 11, pp. 285–290, 2010.

[62] X. Yang, J. Loos, S. C. Veenstra, W. J. H. Verhees, M. M. Wienk, J. M. Kroon, M. A. J. Michels, and R. A. J. Janssen *Nano. Lett.*, vol. 5, pp. 579–583, 2005.

[63] M. D. McGehee *MRS Bulletin*, vol. 34, p. 95100, 2009.

[64] L. Chen, G. Dong, L. Duan, J. Qiao, D. Zhang, L. Wang, and Y. Qiu *J. Phys. Chem. C.*, vol. 114, pp. 9056–9061, 2010.

[65] W. Ma, A. Gopinathan, and A. J. Heeger *Adv. Mater.*, vol. 19, p. 36563659, 2007.

[66] C. Kim and J. Kim *Opt. Express.*, vol. 16, pp. 19987–19994, 2008.

[67] M. Caironi, M. Bird, D. Fazzi, Z. Chen, R. D. Pietro, C. Newman, A. Facchetti, and H. Sirringhaus *Adv. Funct. Mater.*, 2011.

[68] H. Sirringhaus, M. Bird, and N. Zhao *Adv. Mater.*, vol. 22, pp. 3893–3898, 2010.

[69] R. Coehoorn *Phys. Rev. B.*, vol. 75, pp. 1–10, 2007.

[70] B. A. Gregg *Soft Matter*, vol. 5, p. 2985, 2009.

[71] M. Woodhouse, C. L. Perkins, M. T. Rawls, R. a. Cormier, Z. Liang, A. M. Nardes, and B. A. Gregg *J. Phys. Chem. C.*, vol. 114, pp. 6784–6790, 2010.

[72] G. Dennler, M. C. Scharber, and C. J. Brabec *Adv. Mater.*, vol. 21, pp. 1–6, 2009.

[73] G. Juska, K. Arlauskas, M. Viliunas, and J. Kocka *Phys. Rev. Lett.*, vol. 84, pp. 4946–4949, 2000.

[74] J. M. Frost, M. A. Faist, and J. Nelson *Adv. Mater.*, vol. 22, pp. 4881–4884, 2010.

[75] M. Jaiswal and R. Menon *Polym. Int.*, vol. 55, pp. 1371–1384, 2006.

[76] D. H. Dunlap, P. E. Parris, and V. M. Kenkre *Phys. Rev. Lett.*, vol. 77, p. 542545, 1996.

[77] L. B. Schein, A. Peled, and D. Glatz *J. Appl. Phys.*, vol. 66, pp. 686–692, 1989.

[78] S. V. Novikov, D. H. Dunlap, V. M. Kenkre, P. E. Parris, and A. V. Vannikov *Phys. Rev. Lett.*, vol. 81, p. 44724475, 1998.

[79] L. Wang, D. Fine, D. Basu, and A. Dodabalapur *J. Appl. Phys.*, vol. 101, p. 3443, 2007.

[80] B. H. Hamadani, C. A. Richter, D. J. Gundlach, R. J. Kline, I. McCulloch, and M. Heeney *J. Appl. Phys.*, vol. 102, pp. 1–7, 2007.

[81] B. H. Hamadani and D. Natelson *J. Appl. Phys.*, vol. 95, p. 12271232, 2007.

[82] W. D. Gill *J. Appl. Phys.*, vol. 43, pp. 5033–5040, 1972.

[83] P. M. Borsenberger, L. Pautmeier, and H. Bassler *J. Chem. Phys.*, vol. 94, p. 5447, 1991.

[84] T. Li, W. Hu, and D. Zhu *Adv. Mater.*, vol. 22, pp. 286–300, 2010.

[85] C. Tengstedt, W. Osikowicz, W. R. Salaneck, I. D. Parker, C. H. Hsu, and M. Fahlman *Appl. Phys. Lett.*, vol. 88, pp. 1–3, 2006.

[86] Y. Shen, A. R. Hosseini, M. H. Wong, and G. G. Malliaras *ChemPhysChem.*, vol. 5, pp. 16–25, 2004.

[87] S. Braun, W. R. Salaneck, and M. Fahlman *Adv. Mater.*, vol. 21, pp. 1450–1472, 2009.

[88] J. H. Worne, R. Giridharagopal, K. F. Kelly, and D. Natelson *Nano Res.*, vol. 1, pp. 341–350, 2008.

[89] F. Flores, J. Ortega, and H. Vazquez *Phys. Chem. Chem. Phys.*, vol. 11, pp. 8658–8675, 2009.

[90] P. Vanlaeke, A. Swinnen, I. Haeldermans, G. Vanhoyland, T. Aernouts, D. Cheyns, C. Deibel, J. DHaen, P. Heremans, J. Poortmans, and J. V. Manca *Sol. Energ. Mat. Sol.*, vol. 90, p. 21502158, 2006.

[91] T. J. Savenije, J. Kroeze, X. Yang, and J. Loos *Adv. Funct. Mater.*, vol. 15, p. 12601266, 2004.

[92] R. A. Marsh, J. M. Hodgkiss, S. Albert-Seifried, and R. H. Friend *Nano. Lett.*, vol. 10, p. 923930, 2010.

[93] T. J. Savenijea, J. E. Kroezeb, X. Yang, and J. Loos *Thin Solid Films.*, vol. 511.

[94] F. Laquai, Y. S. Park, J. J. Kim, and T. Basche *Macromol. Rapid Commun.*, vol. 30, p. 12031231, 2009.

[95] M. Pope and C. E. Swenberg, *Electronic Processes in Organic Crystals and Polymers.* Oxford: Oxford University Press, 1999.

[96] D. Hertel and H. Bassler in *Organic Light Emitting Devices* (K. Mullen and U. Scherf, eds.), Weinheim: Wiley-VCH, 2006.

[97] J. W. Cahn and J. E. Hilliard *J. Chem. Phys.*, vol. 28, p. 258, 1958.

[98] A. J. Mozer and N. S. Sariciftci *Chem. Phys. Lett.*, vol. 389, pp. 438–442, 2004.

[99] W. Jiang, M. Salvador, and S. T. Dunham *Appl. Phys. Lett.*, vol. 103, p. 183303, 2013.

[100] J. B. You, L. T. Dou, K. Yoshimura, T. Kato, K. Ohya, T. Moriarty, K. Emery, C. C. Chen, J. Gao, G. Li, and Y. Yang *Nature Commun.*, vol. 4, p. 1446, 2013.

[101] M. A. Green, K. Emery, Y. Hishikawa, W. Warta, and E. D. Dunlop *Prog. Photovoltaics*, vol. 21, pp. 1–11, 2013.

[102] B. Niesen, B. P. Rand, P. V. Dorpe, D. Cheyns, L. M. Tong, A. Dmitriev, and P. Heremans *Adv. Energy Mater.*, vol. 3, p. 145, 2013.

[103] H. Choi, J. P. Lee, S. J. Ko, J. W. Jung, H. Park, S. Yoo, O. Park, J. R. Jeong, S. Park, and J. Y. Kim *Nano. Lett.*, vol. 13, p. 2204, 2013.

[104] E. Stratakis and E. Kymakis *Mater. Today*, vol. 16, p. 133, 2013.

[105] A. J. Morfa, K. L. Rowlen, T. H. Reilly, M. J. Romero, and J. van de Lagemaat *Appl. Phys. Lett.*, vol. 92, p. 013504, 2008.

[106] J. L. Wu, F. C. Chen, Y. S. Hsiao, F. C. Chien, P. L. Chen, C. H. Kuo, M. H. Huang, and C. S. Hsu *ACS Nano*, vol. 5, p. 959, 2011.

[107] M. Xue, L. Li, B. J. T. de Villers, H. J. Shen, J. F. Zhu, Z. B. Yu, A. Z. Stieg, Q. B. Pei, B. J. Schwartz, and K. L. Wang *Appl. Phys. Lett.*, vol. 98, p. 253302, 2011.

[108] M. Salvador, B. A. MacLeod, A. Hess, A. P. Kulkarni, K. Munechika, J. I. L. Chen, and D. S. Ginger *ACS Nano*, vol. 6, p. 10024, 2012.

[109] R. B. Dunbar, T. Pfadler, and L. Schmidt-Mende *Opt. Express*, vol. 20, p. A177, 2012.

[110] J. F. Zhu, M. Xue, H. J. Shen, Z. Wu, S. Kim, J. J. Ho, A. Hassani-Afshar, B. Q. Zeng, and K. L. Wang *Appl. Phys. Lett.*, vol. 98, p. 151110, 2011.

[111] X. F. Li, N. P. Hylton, V. Giannini, K. H. Lee, N. J. Ekins-Daukes, and S. A. Maier *Opt. Express*, vol. 19, p. A888, 2011.

[112] X. F. Li, N. P. Hylton, V. Giannini, K. H. Lee, N. J. Ekins-Daukes, and S. A. Maier *Prog. Photovoltaics*, vol. 21, pp. 109–120, 2013.

[113] E. Hao and G. C. Schatz *J. Chem. Phys.*, vol. 120, p. 357, 2004.

[114] J. E. Millstone, S. J. Hurst, G. S. Metraux, J. I. Cutler, and C. A. Mirkin *Small*, vol. 5, p. 646, 2009.

[115] www.lumerical.com, *Lumerical FDTD Solutions Manual*.

[116] S. Inc., *Sentaurus Device User Guide*. Mountain View, CA, h-2013.03 ed.

[117] F. Monestier, J.-J. Simon, P. Torchio, L. Escoubas, F. Flory, S. Bailly, R. de Bettignies, S. Guillerez, and C. Defranoux *Sol. Energy Mater. Sol. Cells.*, vol. 91, pp. 405–410, 2007.

[118] H. Hoppe, N. S. Sariciftci, and D. Meissner *Mol. Cryst. Liq. Cryst.*, vol. 385, pp. 113–119, 2010.

[119] E. D. Palik, *Handbook of Optical Constants of Solids*, vol. 1. Orlando: Academic Press, 1985.

[120] J. Robinson and Y. Rahmat-Samii *IEEE Trans. Antennas. Propag.*, vol. 52, pp. 397–407, 2004.

[121] P. E. Shaw, A. Ruseckas, and I. D. W. Samuel *Adv. Mater.*, vol. 20, p. 3516, 2008.

[122] S. Inc., *Sentaurus Device Electromagnetic Wave Solver User Guide*. Mountain View, CA, h-2013.03 ed.

[123] W. Jiang and S. T. Dunham *Proceedings of the 37th IEEE on Photovoltaic Specialists Conference (PVSC)*, pp. 889–893, 2011.

[124] M. Lu, U. Das, S. Bowden, S. Hegedus, and R. Birkmire *Proceedings of the 34th IEEE on Photovoltaic Specialists Conference (PVSC)*, p. 1475, 2009.

[125] P. W. M. Blom, V. D. Mihailetchi, L. J. A. Koster, and D. E. Markov *Adv. Mater.*, vol. 19, p. 1551, 2007.

[126] V. Jankovic, Y. Yang, J. B. You, L. T. Dou, Y. S. Liu, P. Cheung, and J. P. Chang *ACS Nano*, vol. 7, p. 3815, 2013.

[127] D. H. Wang, D. Y. Kim, K. W. Choi, J. H. Seo, S. H. Im, J. H. Park, O. O. Park, and A. J. Heeger *Angew. Chem., Int. Ed.*, vol. 50, p. 5519, 2011.

[128] A. Kumar, S. Sista, and Y. Yang *J. Appl. Phys.*, vol. 105, p. 094512, 2009.

[129] K. Topp, H. Borchert, F. Johnen, A. V. Tune, M. Knipper, E. von Hauff, J. Parisi, and K. Al-Shamery *J. Phys. Chem. A*, vol. 114, p. 3981, 2010.

[130] S. Vasko, W. Jiang, R. Chen, R. Hanlen, J. Torrey, S. Dunham, and M. Rolandi *Phys. Chem. Chem. Phys.*, vol. 13, pp. 4842–4845, 2011.

[131] S. Vasko, W. Jiang, H. Lai, M. Sadilek, S. Dunham, and M. Rolandi *J. Mater. Chem. C.*, vol. 1, pp. 282–289, 2012.

[132] H. Ko, K. Takei, R. Kapadia, S. Chuang, H. Fang, P. W. Leu, K. Ganapathi, E. Plis, H. S. Kim, S. Y. Chen, M. Madsen, A. C. Ford, Y. L. Chueh, S. Krishna, S. Salahuddin, and A. Javey *Nature.*, vol. 468, pp. 286–289, 2010.

[133] J. Yoon, S. Jo, I. S. Chun, I. Jung, H. S. Kim, M. Meitl, E. Menard, X. Li, J. J. Coleman, U. Paik, and J. A. Rogers *Nature.*, vol. 465, pp. 329–333, 2010.

[134] M. Paniccia, R. M. Rao, and W. M. Yee *J. Vac. Sci. Technol., B.*, vol. 16, pp. 3625–3630, 1998.

[135] R. Chen, T. T. Tran, K. W. Ng, L. C. Chuang, F. G. Sedgwick, and C. C. Hasnian *Nature Photon.*, vol. 5, pp. 1–6, 2011.

[136] A. B. Greytak, L. J. Lauhon, M. S. Gudiksen, and C. M. Lieber *Appl. Phys. Lett.*, vol. 84, pp. 4176–4178, 2004.

[137] Y. Wu, J. Xiang, C. Yang, W. Lu, and C. M. Lieber *Nature.*, vol. 430, pp. 61–65, 2004.

[138] T. Kuykendall, P. J. Pauzauskie, Y. Zhang, J. Goldberger, D. Sirbuly, D. Denlinger, and P. Yang *Nature Mater.*, vol. 3, pp. 524–528, 2004.

[139] R. Soref *IEEE J. Sel. Top. Quant. Electron.*, vol. 12, pp. 1678–1687, 2006.

[140] B. Tian, P. Xie, T. J. Kempa, D. C. Bell, and C. M. Lieber *Nat. Nanotechnol.*, vol. 4, pp. 824–829, 2009.

[141] R. Garcia, R. V. Martinez, and J. Martinez *Chem. Soc. Rev.*, vol. 35, pp. 29–38, 2006.

[142] D. S. Ginger and H. Z. C. A. Mirkin *Angew. Chem. Int. Ed.*, vol. 43, pp. 30–45, 2004.

[143] W. F. Paxton, J. M. Spruell, and J. F. Stoddart *J. Am. Chem. Soc.*, vol. 131, pp. 6692–6694, 2009.

[144] L. A. Porter, H. C. Choi, J. M. Schmeltzer, A. E. Ribber, L. C. C. Elliott, and J. M. Buriak *Nano. Lett.*, vol. 2, pp. 1369–1372, 2002.

[145] B. Gotsman, U. Duerig, J. Frommer, and C. J. Hawker *Adv. Funct. Mater.*, vol. 16, pp. 1499–1505, 2006.

[146] D. A. Long, K. Unal, R. C. Pratt, M. Malkoch, and J. Frommer *Adv. Mater.*, vol. 19, pp. 4471–4473, 2007.

[147] Z. Wei, D. Wang, S. Kim, S. Y. Kim, Y. Hu, M. K. Yakes, A. R. Laracuente, Z. Dai, S. R. Marder, C. Berger, W. P. King, W. A. de Heer, P. E. Sheehan, and E. Riedo *Science.*, vol. 328, pp. 1373–1376, 2010.

[148] O. Fenwick, L. Bozec, D. Credgington, A. Hammiche, G. M. Lazzerini, Y. R. Silberberg, and F. Cacialli *Nat. Nanotechnol.*, vol. 4, pp. 664–668, 2009.

[149] A. W. Knoll, D. Pires, O. Coulembier, P. Dubois, J. L. Hedrick, J. Frommer, and U. Duerig *Adv. Mater.*, vol. 22, pp. 3361–3365, 2010.

[150] D. Pires, J. L. Hedrick, A. D. Silva, J. Frommer, B. Gotsmann, H. Wolf, M. Despont, U. Duerig, and A. W. Knoll *Science.*, vol. 328, pp. 732–735, 2010.

[151] C. Rankin, C. H. Chou, D. Conklin, and D. A. Bonnell *ACS Nano.*, vol. 1, p. 234238, 2007.

[152] M. Rolandi, C. F. Quate, and H. Dai *Adv. Mater.*, vol. 14, p. 191194, 2002.

[153] P. Avouris, T. Hertel, and R. Martel *Appl. Phys. Lett.*, vol. 71, pp. 285–287, 1997.

[154] C. Cen, S. Thiel, J. Mannhart, and J. Levy *Science.*, vol. 323, pp. 1026–1030, 2009.

[155] M. J. Schmitz, C. R. Kinser, N. E. Cortes, and M. C. Hersam *Small.*, vol. 3, pp. 2053–2056, 2007.

[156] R. Maoz, E. Frydman, S. R. Cohen, and J. Sagiv *Adv. Mater.*, vol. 12, p. 725731, 2000.

[157] D. A. Unruh, C. Mauldin, S. J. Pastine, M. Rolandi, and J. M. J. Frchet *J. Am. Chem. Soc.*, vol. 132, p. 68906891, 2010.

[158] H. J. Kreuzer *Surf. Interface Anal.*, vol. 36, pp. 372–379, 2004.

[159] Z. M. Fresco, I. Suez, S. A. Backer, and J. M. J. Frchet *J. Am. Chem. Soc.*, vol. 126, pp. 8374–8375, 2004.

[160] Z. M. Fresco and J. M. J. Frchet *J. Am. Chem. Soc.*, vol. 127, pp. 8302–8303, 2005.

[161] S. A. Backer, I. Suez, Z. M. Fresco, M. Rolandi, and J. M. J. Frchet *Langmuir.*, vol. 23, pp. 2297–2299, 2007.

[162] X. N. Xie, M. Deng, H. Xu, S. W. Yang, D. C. Qi, X. Y. Gao, H. J. Chung, C. H. Sow, V. B. Tan, and A. T. Wee *J. Am. Chem. Soc.*, vol. 128, pp. 2738–2744, 2006.

[163] J. Germain, M. Rolandi, S. A. Backer, and J. M. J. Frchet *Adv. Mater.*, vol. 20, pp. 4526–4529, 2008.

[164] I. Suez, S. A. Backer, and J. M. J. Frchet *Nano. Lett.*, vol. 5, pp. 321–324, 2005.

[165] I. Suez, M. Rolandi, S. A. Backer, A. Scholl, A. Doran, D. Okawa, A. Zettl, and J. M. J. Frchet *Adv. Mater.*, vol. 19, p. 35703573, 2007.

[166] R. V. Martinez, N. S. Losilla, J. Martinez, Y. Huttel, and R. Garcia *Nano. Lett.*, vol. 7, pp. 1846–1850, 2007.

[167] M. Rolandi, I. Suez, A. Scholl, and J. M. J. Frchet *Angew. Chem. Int. Ed.*, vol. 46, pp. 7477–7480, 2007.

[168] R. Garcia, N. S. Losilla, J. Martnez, R. V. Martinez, F. J. Palomares, Y. Huttel, M. Calvaresi, and F. Zerbetto *Appl. Phys. Lett.*, vol. 96, p. 143110, 2010.

[169] J. D. Torrey, S. E. Vasko, A. Kapetanovic, Z. Zhu, A. Scholl, and M. Rolandi *Adv. Mater.*, vol. 22, pp. 4639–4642, 2010.

[170] S. E. Vasko, A. Kapetanovic, V. Talla, M. Brasino, J. D. Torrey, A. Scholl, and M. Rolandi *Nano. Lett.*, vol. 11, pp. 2386–2389, 2011.

[171] E. S. Snow, G. G. Jernigan, and P. M. Campbell *Appl. Phys. Lett.*, vol. 76, pp. 1782–1784, 2000.

[172] M. Calvaresi, R. V. Martinez, N. S. Losilla, J. Martinez, R. Garcia, and F. Zerbetto *J. Phys. Chem. Lett.*, vol. 1, pp. 3256–3260, 2010.

[173] J. Lee, D. C. Sorescu, and X. Deng *J. Am. Chem. Soc.*, vol. 133, pp. 10066–10069, 2011.

[174] G. Distefano, S. Fignataro, L. Szepes, and J. Borossay *J. Organomet. Chem.*, vol. 104, pp. 173–178, 1976.

[175] L. Lang, *Absorption Spectra in the Ultraviolet and Visible Region*, vol. 9. Academic Press.

[176] X. Zhu and A. Kahn *MRS Bull.*, vol. 35, pp. 443–448, 2010.

[177] T. Oster, A. Kunh, and E. Illenberger *Int. J. Mass Spectrom. Ion Processes.*, vol. 89, pp. 1–72, 1989.

[178] H. Lai, W. Jiang, S. E. Vasko, S. T. Dunham, and M. Rolandi. group discussion, 2012.

[179] I. Lyubinetsky, S. Mezhenny, W. J. Choyke, and J. T. Yates *J. Vac. Sci. Technol., A.*, vol. 17, pp. 1445–1450, 1999.

[180] J. W. Fleming and C. N. Banwell *J. Mol. Spectrosc.*, vol. 31, pp. 318–340, 1969.

[181] L. Lu, Z. Luo, T. Xu, and L. Yu *Nano. Lett.*, vol. 13, pp. 59–64, 2013.

[182] A. G. Zabrodskii, "Band structure and carrier concentration," 2012.

[183] H. Rauscher, F. Behrendt, and R. J. Behm *J. Vac. Sci. Technol., B.*, vol. 15, pp. 1373–1377, 1997.

Appendix A

SENTAURUS SIMULATOR SCRIPTS

Researchers seldom publish their codes in their paper or thesis. It is extremely hard for other people to replicate their work. I hereby publish my scripts written for the projects I have done. Feel free to use part of my codes to start your research after a careful investigation of the physical mechanism behind your targeting device.

A.1 Scripts for OPV simulation

A.1.1 Sentaurus Electromagnetic Wave Solver Scripts for Calculating 3D Triangular Silver Nano-Prisms

```
#-----------------------------------------
# Organic Solar Cell Optical Simulation
# Use EMW-plus kernel

# Author: Wenjun Jiang
# All rights reserved
#-----------------------------------------

#setdep @previous@

Globals {
  GridFile        = "n@previous@_msh.tdr"
  ParameterFile        = "@parameter@"
  InspectFile        = "@plot@"
  LogFile        = "@log@"
```

```
  NumberOfThreads    = @threads@
  TotalTimeSteps    = 20000000
  OverSampling        = 1.2
}

ComplexRefractiveIndex {
  WavelengthDep        = {Real,Imag}
}

DispersiveMedia {
  Material        = {"@back_metal@"}
  Model            = SingleDipoleDrude
  ModelParameters    = ComputeFromComplexRefractiveIndex
  DeltaK        = 0.01
}

#if "@_metalNP_h@" == "0"
  ## do nothing
#else
  DispersiveMedia {
    Material        = {"@MetalNP@"}
    Model        = SingleDipoleDrude
    ModelParameters    = ComputeFromComplexRefractiveIndex
    DeltaK        = 0.01
  }
#endif

Boundary {
  Type            = periodicOblique
  Sides            = {X,Y}
```

```
}

# Use CPML ABC for any solar cell structure considering surface plasmonic effects
Boundary {
  Type            = CPML
  Sides            = {Z}
  SigmaMax        = 10000000.0
  OrderSigma        = 3
  AlphaMax        = 0.0
  OrderAlpha        = 1
  KappaMax        = 10.0
  OrderKappa        = 3
  Thickness        = 25
}

PlaneWaveExcitation {

  # Excitation plane needs to be approximately in the center of the gas layer
    BoxCorner1        = (0, 0, @<0-wavelength>@)
    BoxCorner2        = (@width@, @width@, @<0-wavelength>@)

  # Define incident light angle and polarization
    Theta        = 0
    Phi            = 0
    # Psi=90 for TE mode, Psi=0 for TM mode, Mix TE and TM mode together to better fit
    # the unpolarized sunlight (I tried different values, 45 is the best)
      Psi        = @Psi@

  # Define incident light frequency and intensity
    Wavelength        = @<wavelength*1.0e+3>@    # in [nm]
```

```
    Intensity        = @Intensity@        # in [W/cm2]

  # Rise and periods
    Nrise        = 30  # number of signal periods until full power, 30 is optimized

}

Plot {
  Name            = "n@node@_Eabs"
  Quantity        = {AbsElectricField}
  FinalPlot        = yes
}

Plot {
  Name           = "n@node@_xcut"
  Quantity        = {AbsElectricField}
  BoxCorner1        = (@<width/2.0>@, 0, @<_t_glass/1.0e+3>@)
  BoxCorner2=(@<width/2.0>@, @width@, @<(_t_glass+_t_anode+_t_pedot+_t_active)/1.0e+3>@)
  Domain        = Surface
  Sides            = {X}
  FinalPlot        = yes
}

Extractor {
  Quantity        = {AbsorbedPhotonDensity, OpticalGeneration, PowerFluxDensity}
  Name            = "n@node@_extract"
  Type            = dfgeo
  DfgeoFile        = "n@node|sde@_ele_msh.tdr"
}
```

```
Sensor {
  Name            = "OptGen"
  Quantity        = OpticalGeneration
  Region        = {"active"}
  Mode            = {Integrate, Average}
}

#if "@_metalNP_h@" == "0"
  ## do nothing
#else
  Sensor {
    Name        = "OptGen"
    Quantity        = OpticalGeneration
    Region        = {"Metal_Nano_Prism"}
    Mode        = {Integrate, Average}
  }
#endif

Sensor {
  Name            = "TplusA"
  Quantity        = PowerFluxDensity
  # Collection of absorption and transmission.
  # Plane needs to be lower than excitation plane but still in the gas layer
    BoxCorner1        = (0, 0, @<0-wavelength/2.0>@)
    BoxCorner2        = (@width@, @width@, @<0-wavelength/2.0>@)
  Mode            = {Integrate}
}

Sensor {
```

```
  Name            = "Reflected"
  Quantity        = PowerFluxDensity
  # Reflection plane needs to be at the very top of the gas layer
    BoxCorner1        = (0, 0, @<0-wavelength*2.0>@)
    BoxCorner2        = (@width@, @width@, @<0-wavelength*2.0>@)
  Mode            = {Integrate}
}

Sensor {
  Name            = "Transmitted"
  Quantity        = PowerFluxDensity
  # Transmission plane needs to be at the very bottom of the active layer
    BoxCorner1  = (0, 0, @<(_t_glass+_t_anode+_t_pedot+_t_active)/1.0e+3>@)
    BoxCorner2  = (@width@, @width@, @<(_t_glass+_t_anode+_t_pedot+_t_active)/1.0e+3>@)
  Mode            = {Integrate}
}

Sensor {
  Name            = "GI"
  Quantity        = PowerFluxDensity
  # Interface between Glass and ITO layers
    BoxCorner1        = (0, 0, @<_t_glass/1.0e+3>@)
    BoxCorner2        = (@width@, @width@, @<_t_glass/1.0e+3>@)
  Mode            = {Integrate}
}

Sensor {
  Name            = "IP"
  Quantity        = PowerFluxDensity
  # Interface between ITO and PEDOT layers
```

```
    BoxCorner1        = (0, 0, @<(_t_glass+_t_anode)/1.0e+3>@)
    BoxCorner2        = (@width@, @width@, @<(_t_glass+_t_anode)/1.0e+3>@)
  Mode            = {Integrate}
}

Sensor {
  Name            = "PA"
  Quantity        = PowerFluxDensity
  # Interface between PEDOT and Active layers
    BoxCorner1        = (0, 0, @<(_t_glass+_t_anode+_t_pedot)/1.0e+3>@)
    BoxCorner2        = (@width@, @width@, @<(_t_glass+_t_anode+_t_pedot)/1.0e+3>@)
  Mode            = {Integrate}
}

Sensor {
  Name            = "Backmetal"
  Quantity        = AbsorbedPowerDensity
  # Absorption of Backmetal region needs to be from the very top
  # to the very bottom of the backmetal layer
    BoxCorner1  = (0, 0, @<(_t_glass+_t_anode+_t_pedot+_t_active)/1.0e+3>@)
    BoxCorner2  = (@width@, @width@, @<(_t_glass+_t_anode+_t_pedot+_t_active+_t_backmetal)/1.0e
  Mode            = {Integrate}
}

Sensor {
  Name            = "Absorbed"
  Quantity        = AbsorbedPowerDensity
  Region        = {"active"}
  Mode            = {Integrate}
}
```

```
#if "@_metalNP_h@" == "0"
  ## do nothing
#else
  Sensor {
    Name        = "Absorbed"
    Quantity        = AbsorbedPowerDensity
    Region        = {"Metal_Nano_Prism"}
    Mode        = {Integrate}
  }
#endif

#if "@_metalNP_h@" == "0"
  ## do nothing
#else
  Sensor {
    Name        = "Absorbed"
    Quantity        = AbsorbedPowerDensity
    Region        = {"Thin_Prism"}
    Mode        = {Integrate}
  }
#endif

Sensor {
  Name            = "PEDOT"
  Quantity        = AbsorbedPowerDensity
  # Absorption of PEDOT region needs to be from the very top
  # to the very bottom of the ITO layer
    BoxCorner1        = (0, 0, @<(_t_glass+_t_anode)/1.0e+3>@)
    BoxCorner2        = (@width@, @width@, @<(_t_glass+_t_anode+_t_pedot)/1.0e+3>@)
```

```
  Mode            = {Integrate}
}

Sensor {
  Name            = "ITO"
  Quantity        = AbsorbedPowerDensity
  # Absorption of ITO region needs to be from the very top
  # to the very bottom of the ITO layer
    BoxCorner1        = (0, 0, @<_t_glass/1.0e+3>@)
    BoxCorner2        = (@width@, @width@,
                                @<(_t_glass+_t_anode)/1.0e+3>@)
  Mode            = {Integrate}
}

Sensor {
  Name            = "Glass"
  Quantity        = AbsorbedPowerDensity
  # Absorption of Glass region needs to be from the very top
  # to the very bottom of the glass layer
    BoxCorner1        = (0, 0, 0)
    BoxCorner2        = (@width@, @width@, @<_t_glass/1.0e+3>@)
  Mode            = {Integrate}
}

Detector {
  Tolerance        = @Stop@
}
```

A.1.2 Sentaurus Device Simulator for Calculating 3D Triangular Silver Nano-Prisms' EQE Values

```
#-------------------------------------
# Organic Solar Cell EQE Simulation
# Author: Wenjun Jiang
# All rights reserved
#-------------------------------------

Electrode {
  { Name="anode"    Voltage = 0.0 }
  { Name="cathode"    Voltage = 0.0 }
}



File {
  Grid                =    "n@node|sde@_ele_msh.tdr"
  OpticalGenerationInput    =    "n@previous@_tcl.tdr"
  Parameter             =    "@parameter@"
  Output            =    "n@node@"
  Plot                =    "n@node@"
  Current             =    "n@node@"
}




Math {
  -CheckUndefinedModels
  Digits            =    10
```

```
  StackSize             =    100000000    *100MB
  Extrapolate
  Iterations             =    40
  RhsFactor             =    1e40
  RhsMin             =    1e-20
  Traps(
    Damping             =    100
  )
  Notdamped             =    100
  RelErrcontrol
  Method             =    ILS(set=1)
  ExitOnFailure
  Number_of_threads         =    @threads@
  Number_of_Solver_Threads    =    @threads@
  #if "@_metalNP_h@" == "0"
    #- do nothing
  #else
    NonLocal "NLM" (
      Barrier(
        Region             =    "Thin_Prism"
      )
      Length             =    18e-7    *cm
      Permeation             =    18e-7    *cm
    )
  #endif
}


** Schottky Barriers
  Physics(MaterialInterface = "PEDOT/P3HTPCBM")            { Schottky }
```

```
  Physics(MaterialInterface = "@back_metal@/P3HTPCBM")        { Schottky }


Physics {
  Recombination (
    SRH
  )
  EffectiveIntrinsicDensity(
    NoBandGapNarrowing
  )

  #if "@_metalNP_h@" == "0"
    #- do nothing
  #else
    **- Barrier Tunneling

      #if [string match electron "@Barrier_Tunneling@"]
        eBarrierTunneling "NLM"

      #elseif [string match hole "@Barrier_Tunneling@"]
        hBarrierTunneling "NLM"
      #elseif [string match e_h "@Barrier_Tunneling@"]
        eBarrierTunneling "NLM"
        hBarrierTunneling "NLM"
      #else
        #- do nothing
      #endif
  #endif

**- Optics Simulation Added
```

```
  Optics(
    OpticalGeneration(
      QuantumYield(
        StepFunction(
          EffectiveBandgap
        )
      )
      ReadFromFile(
        Scaling            =    0.0
      )
    )
  )
}


Physics (region="active") {
  Mobility (
    eHighFieldSaturation (
      PFMob
      Eparallel
    )
  )
  EffectiveMass (
    GaussianDOS
  )
  Traps(
    (Donor Exponential fromCondBand Conc=1e+12 EnergyMid=0 EnergySig=0.5
      eXsection=1e-14 hXsection=1e-14
    )
    (Acceptor Exponential fromValBand Conc=1e+12 EnergyMid=0 EnergySig=0.5
```

```
      eXsection=1e-14 hXsection=1e-14
    )
  )

}


Plot {

 *-- Density & Currents
  eDensity hDensity
  eCurrent/Vector hCurrent/Vector TotalCurrent/vector

  eMobility hMobility
  eVelocity hVelocity
  eQuasiFermi hQuasiFermi

 *-- Temperature
  eTemperature hTemperature Temperature

 *-- Fileds & Charges
  ElectricField/vector Potential SpaceCharge

 *-- Doping profiles
  DopingConcentration DonorConcentration AcceptorConcentration

 *-- Generation & Recombination
  SRH  Auger  Band2Band
  eAvalancheGeneration hAvalancheGeneration AvalancheGeneration
  TotalRecombination SurfaceRecombination
```

```
 *-- Driving forces
  eGradQuasiFermi/vector  hGradQuasiFermi/vector

 *-- Band structure & Composition

  BandGap  BandGapNarrowing  Affinity
  ConductionBand ValenceBand

 *-- Optics
  AbsorbedPhotonDensity
  OpticalGeneration

}


Solve {

   Coupled (Iterations = 100000) { Poisson }
   Plot (FilePrefix= "n@node@_eqbm")
   Coupled (Iterations = 100000) { Poisson Electron Hole }

   Plot (FilePrefix= "n@node@_eqbm_coupled")

   Quasistationary (
     InitialStep=0.01 MaxStep=0.1 Minstep=1e-5
     Goal { ModelParameter="Optics/OpticalGeneration/ReadFromFile/Scaling"
               value=0.4711346}

   ) { Coupled { Poisson Electron Hole }
```

```
        CurrentPlot }
    Plot (FilePrefix= "n@node@_eqbm_coupled_optics")

    System("rm tmp*")

}
```

A.1.3 Sentaurus Device Simulator for Calculating 3D Triangular Silver Nano-Prisms' I-V Values

```
#-------------------------------------------------
# Organic Solar Cell Current-Voltage (I-V) Simulation
# Used Sentaurus Device Simulator

# Author: Wenjun Jiang
# All rights reserved
#-------------------------------------------------


Electrode {
  { Name="anode"    Voltage = 0.0 }
  { Name="cathode"    Voltage = 0.0 }
}


File {
  Grid                =    "n@node|sde@_ele_msh.tdr"
  OpticalGenerationInput    =    "n@previous@_tcl.tdr"
```

```
  Parameter            =    "@parameter@"
  Output            =    "n@node@"
  Plot                =    "n@node@"
  Current             =    "n@node@"
}



Math {
  -CheckUndefinedModels
  Digits=10
  StackSize            =    100000000    *100MB
  Extrapolate
  Iterations            =    40
  RhsFactor            =    1e40
  RhsMin            =    1e-20
  Traps(
    Damping            =    100
  )
  Notdamped            =    100
  RelErrcontrol
  Method            =    ILS(set=1)
  ExitOnFailure
  Number_of_threads        =    @threads@
  Number_of_Solver_Threads    =    @threads@
  #if "@_metalNP_h@" == "0"
    #- do nothing
  #else
    NonLocal "NLM" (
      Barrier(
```

```
        Region            =    "Thin_Prism"
      )
      Length            =    18e-7    *cm
      Permeation            =    18e-7    *cm
    )
  #endif
}


** Schottky Barriers
  Physics(MaterialInterface = "PEDOT/P3HTPCBM")            { Schottky }
  Physics(MaterialInterface = "@back_metal@/P3HTPCBM")        { Schottky }


Physics {
  Recombination (
    SRH
  )
  EffectiveIntrinsicDensity(
    NoBandGapNarrowing
  )

  #if "@_metalNP_h@" == "0"
    #- do nothing
  #else
    **- Barrier Tunneling
      #if [string match electron "@Barrier_Tunneling@"]
        eBarrierTunneling "NLM"
      #elseif [string match hole "@Barrier_Tunneling@"]
        hBarrierTunneling "NLM"
```

```
      #elseif [string match e_h "@Barrier_Tunneling@"]
        eBarrierTunneling "NLM"
        hBarrierTunneling "NLM"
      #else
        #- do nothing
      #endif
  #endif

**- Optics Simulation Added
  Optics(
    OpticalGeneration(
      QuantumYield(
        StepFunction(
          EffectiveBandgap
        )
      )
      ReadFromFile(
        Scaling            =    0.0
      )
    )
  )
}


Physics (region="active") {
  Mobility (
    eHighFieldSaturation (
      PFMob
      Eparallel
    )
```

```
  )
  EffectiveMass (
    GaussianDOS
  )
  Traps(
    (Donor Exponential fromCondBand Conc=1e+12 EnergyMid=0 EnergySig=0.5
      eXsection=1e-14 hXsection=1e-14
    )
    (Acceptor Exponential fromValBand Conc=1e+12 EnergyMid=0 EnergySig=0.5
      eXsection=1e-14 hXsection=1e-14
    )
  )

}


Plot {

 *-- Density & Currents
  eDensity hDensity
  eCurrent/Vector hCurrent/Vector TotalCurrent/vector
  eMobility hMobility
  eVelocity hVelocity
  eQuasiFermi hQuasiFermi

 *-- Temperature
  eTemperature hTemperature Temperature

 *-- Fileds & Charges
  ElectricField/vector Potential SpaceCharge
```

```
 *-- Doping profiles
  DopingConcentration DonorConcentration AcceptorConcentration

 *-- Generation & Recombination
  SRH  Auger  Band2Band
  eAvalancheGeneration hAvalancheGeneration AvalancheGeneration
  TotalRecombination SurfaceRecombination

 *-- Driving forces
  eGradQuasiFermi/vector  hGradQuasiFermi/vector

 *-- Band structure & Composition
  BandGap  BandGapNarrowing  Affinity
  ConductionBand ValenceBand

 *-- Optics
  AbsorbedPhotonDensity
  OpticalGeneration

}

Solve {

   Coupled (Iterations = 100000) { Poisson }
   Plot (FilePrefix= "n@node@_eqbm")
   Coupled (Iterations = 100000) { Poisson Electron Hole }
   Plot (FilePrefix= "n@node@_eqbm_coupled")

   Quasistationary (
```

```
    InitialStep=0.01 MaxStep=0.1 Minstep=1e-5
    Goal { ModelParameter="Optics/OpticalGeneration/ReadFromFile/Scaling"
              value=0.4711346}
  ) { Coupled { Poisson Electron Hole } }
  Plot (FilePrefix= "n@node@_eqbm_coupled_optics")

  NewCurrentPrefix = ""
  Quasistationary (
    InitialStep=1e-4 Increment=1.35
    MaxStep=1e-2 MinStep=1e-5 DoZero
    Goal { voltage = @V_Goal@ Name="anode" }

  ) { Coupled {Poisson Electron Hole }
      Plot(FilePrefix= "n@node@_0.1" When(Contact = "anode" voltage = 0.1 ))
      Plot(FilePrefix= "n@node@_0.2" When(Contact = "anode" voltage = 0.2 ))
      Plot(FilePrefix= "n@node@_0.3" When(Contact = "anode" voltage = 0.3 ))
      Plot(FilePrefix= "n@node@_0.4" When(Contact = "anode" voltage = 0.4 ))
      Plot(FilePrefix= "n@node@_0.5" When(Contact = "anode" voltage = 0.5 ))
      Plot(FilePrefix= "n@node@_0.6" When(Contact = "anode" voltage = 0.6 ))
      Plot(FilePrefix= "n@node@_0.7" When(Contact = "anode" voltage = 0.7 ))
      Plot(FilePrefix= "n@node@_0.8" When(Contact = "anode" voltage = 0.8 ))
  }

  System("rm tmp*")

}
```

A.1.4 Sentaurus Inspect for Calculating 3D Triangular Silver Nano-Prisms' EQE Values

```
#----------------------------------------
# Organic Solar Cell Post-Simulation Analysis -- EQE Curve
# Use Inspect

# Author: Wenjun Jiang
# All rights reserved
#----------------------------------------

## Set some parameters
  set width @width@
  ### incoming light intensity in [W/cm2]
    set intensity @Intensity@
  ### wavelength changes from [um] to [m]
    set lambda @<wavelength*1e-6>@
  set h 6.626176e-34
  set c 2.99792458e8
  set q 1.6021892e-19
  ### Area factor, changes from [A/um] to [A/cm2],
  ### notice here we shouldn't change to [mA/cm2]
    set conversion_factor    [expr 1e+8/($width*$width)]

## Load project
  load_library extend
  proj_load n@previous@_des.plt Model
  cv_createDS I_mod  "Model time" "Model cathode TotalCurrent" y

## Model result
```

```
  set Isc            [cv_compute "vecvaly(<I_mod>,1.0)" A A A A]
  set Jsc            [expr $conversion_factor * $Isc]
  ### EQE = (Jsc/e) / (J_AM1.5 / (E_photon=hc/lambda))
    set EQE            [expr 100 * $Jsc / $intensity * ($h * $c / $lambda / $q)]

## Load project
  set gc1 "n@node|TE@_eml"
  proj_load "$gc1.plt"
  set gc2 "n@node|TM@_eml"
  proj_load "$gc2.plt"

  set AreaFactor    [expr $width*$width*1e-4*1e-4*$intensity]
  set A_blend_1    [expr [ds_getValue $gc1 "AbsorbedIntegr active/AbsorbedPowerDensity"]
                                  /$AreaFactor]
  set A_blend_2    [expr [ds_getValue $gc2 "AbsorbedIntegr active/AbsorbedPowerDensity"]
                                  /$AreaFactor]
  ## Average
    set A_blend      [expr ($A_blend_1 + $A_blend_2)/2.0]

  set IQE            [expr $EQE / $A_blend]

## Output calculation result
  puts "DOE: EQE        [format %.4f $EQE]"
  puts "DOE: IQE        [format %.4f $IQE]"
```

A.1.5 Sentaurus Inspect for Calculating 3D Triangular Silver Nano-Prisms' I-V Values

```
#----------------------------------------
```

```
# Organic Solar Cell Post-Simulation Analysis -- IV Curve
# Use Inspect

# Author: Wenjun Jiang
# All rights reserved
#----------------------------------------

set width @width@

proj_load n@previous@_des.plt Model
proj_load experimental.plt Experimental

cv_createDS I_mod  "Model anode OuterVoltage" "Model anode TotalCurrent"
cv_create V_mod  "Model anode OuterVoltage" "Model anode OuterVoltage"
cv_createWithFormula P_mod  "<V_mod>*<I_mod>" A A

cv_createDS I_ex  "Experimental anode OuterVoltage" "Experimental anode TotalCurrent"
cv_create V_ex  "Experimental anode OuterVoltage" "Experimental anode OuterVoltage"
cv_createWithFormula P_ex  "<V_ex>*<I_ex>" A A


## Model Result
set Isc_mod        [expr -1.0*[cv_compute "vecvaly(<I_mod>,0.0)" A A A A]]
set conversion_factor    [expr 1.0e+11/($width*$width)]
set Jsc_mod        [expr $conversion_factor * $Isc_mod]
puts "DOE: Jsc_mAcm2    [format %.4f $Jsc_mod]"

set Voc_mod        [cv_compute "veczero(<I_mod>)" A A A A]
puts "DOE: Voc_V    [format %.4f $Voc_mod]"
```

```
set Pmpp_mod        [cv_compute "vecmin(<P_mod>)" A A A A]
set Pmax_mWcm2_mod    [expr -1.0 * $conversion_factor * $Pmpp_mod]
## In AM1.5G, incident irradiation is 100mW/cm2,
## while power conversion efficiency (PCE) is reported in %
set PCE_perc_mod    [expr $Pmax_mWcm2_mod / 100 * 100]
## puts "DOE: Pmax_mWcm2    [format %.2f $Pmax_mWcm2_mod]"
puts "DOE: PCE_perc_mod    [format %.2f $PCE_perc_mod]"

set ff_mod        [expr -100.0 * $Pmpp_mod / ($Isc_mod) / ($Voc_mod)]
puts "DOE: FF        [format %.2f $ff_mod]"


## Experimental Result
set Isc_ex        [expr -1.0*[cv_compute "vecvaly(<I_ex>,0.0)" A A A A]]
## 40nm active layer device with 0.018 cm^2 area
set cf_ex        [expr 1.0e+3/0.018]
set Jsc_ex        [expr $cf_ex * $Isc_ex]
puts "DOE:  Jsc_ex    [format %.4f $Jsc_ex]"

set Voc_ex        [cv_compute "veczero(<I_ex>)" A A A A]
puts "DOE: Voc_ex    [format %.4f $Voc_ex]"

set Pmpp_ex        [cv_compute "vecmin(<P_ex>)" A A A A]
set Vmpp_ex        [cv_compute "vecvalx(<P_ex>, $Pmpp_ex)" A A A A]
set Pmax_mWcm2_ex    [expr -1.0 * $cf_ex * $Pmpp_ex]
set PCE_perc_ex        [expr $Pmax_mWcm2_ex / 100 * 100]
## puts "DOE:  Pmax_ex    [format %.2f $Pmax_mWcm2_ex]"
puts "DOE: Vmpp_ex    [format %.4f $Vmpp_ex]"
puts "DOE: PCE_perc_ex    [format %.2f $PCE_perc_ex]"
```

```
set ff_ex        [expr -100.0 * $Pmpp_ex / ($Isc_ex) / ($Voc_ex)]
puts "DOE: FF_ex    [format %.2f $ff_ex]"
```

A.2 Scripts for AFM tip simulation

```
File{
   Grid      = "n@previous@_ele_msh.tdr"
   Plot      = "n@node@_des.tdr"
   Parameter = "pp@node@_des.par"
   Current   = "n@node@_des.plt"
   Output    = "n@node@_des.log"
}

Electrode{
   { Name="pcontact"    Voltage=0.0 }
   { Name="ncontact"    Voltage=0.0 }
}


Plot{
*--Density and Currents, etc
   eDensity hDensity
   TotalCurrent/Vector eCurrent/Vector hCurrent/Vector
   eMobility hMobility
   eVelocity hVelocity
   eQuasiFermi hQuasiFermi

*--Temperature
   eTemperature Temperature * hTemperature
```

```
*--Fields and charges
   ElectricField/Vector Potential SpaceCharge

*--Doping Profiles
   Doping DonorConcentration AcceptorConcentration

*--Generation/Recombination
   SRH Band2Band * Auger
   AvalancheGeneration eAvalancheGeneration hAvalancheGeneration

*--Driving forces
   eGradQuasiFermi/Vector hGradQuasiFermi/Vector
   eEparallel hEparallel eENormal hENormal

*--Band structure/Composition
   BandGap BandGapNarrowing Affinity
   ConductionBand ValenceBand

*--Nonlocal
   NonLocal
}


Math {
   -CheckUndefinedModels
   Number_of_Threads    = @threads@
   StackSize    = 100000000    *100MB
   Derivatives
   Extrapolate
```

```
   Iterations    = 30
   Notdamped    = 100
   ExitOnFailure
   RelErrControl
   Method    = ILS(set=1)
   ErRef(Electron)    = 1.e2
   ErRef(Hole)    = 1.e2
   RhsFactor    = 1e+40
   RhsMin    = 1e-20

   NonLocal "top_NLM" (
     Barrier(
        Region    = "tip_SiO2"
     )
     Length    = 10e-7    *cm
     Permeation    = 10e-7    *cm
   )
   NonLocal "bot_NLM" (
     Barrier(
        Region    = "SiO2_sub"
     )
     Length    = 10e-7    *cm
     Permeation    = 10e-7    *cm
   )

}

Physics {
   AreaFactor    = @<Third_Dim/1.0e+3>@
   EffectiveIntrinsicDensity(
```

```
      NoBandGapNarrowing
   )
  #if [string match electron "@Barrier_Tunneling@"]
   eBarrierTunneling "top_NLM"
   eBarrierTunneling "bot_NLM"
  #elseif [string match hole "@Barrier_Tunneling@"]
   hBarrierTunneling "top_NLM"
   hBarrierTunneling "bot_NLM"
  #else
   eBarrierTunneling "top_NLM"
   hBarrierTunneling "top_NLM"
   eBarrierTunneling "bot_NLM"
   hBarrierTunneling "bot_NLM"
  #endif

}

Physics (Material="Silicon") {
   Mobility(
      ConstantMobility
   )
   Recombination(
      SRH (
         DopingDependence
      )
      Auger
      Avalanche
      Band2Band
    )
}
```

```
Physics (Material="Liquid") {
   Mobility(
      ConstantMobility
   )
   Recombination(
      SRH (
         DopingDependence
      )
      Auger
      Avalanche
      Band2Band
    )
}

Solve {
   Coupled(Iterations=10000){ Poisson }
   Plot (FilePrefix= "n@node@_eqbm")
   Coupled(Iterations=10000){ Poisson Electron Hole }
   Plot (FilePrefix= "n@node@_eqbm_coupled")

   Quasistationary(
      InitialStep=1e-4 Increment=1.35
      MinStep=1e-5 MaxStep=0.025
      Goal{ Name="pcontact" Voltage=@V_pcontact@ }
   ){ Coupled{ Poisson Electron Hole }
      Plot(FilePrefix= "n@node@_1_3"
            When(Contact = "pcontact" voltage = @<V_pcontact/3.0>@ ))
      Plot(FilePrefix= "n@node@_2_3"
            When(Contact = "pcontact" voltage = @<V_pcontact*2.0/3.0>@ ))
```

```
      Plot(FilePrefix= "n@node@_3_3"
            When(Contact = "pcontact" voltage = @V_pcontact@ ))
    }

}
```

VITA

Wenjun Jiang is a PhD candidate in Physics at the University of Washington. He graduated with Bachelor of Science from University of Science and Technology of China (USTC) in 2007, and came to the University of Washington pursuing a PhD in theoretical condensed matter physics, under the supervision of Professor Scott T. Dunham since 2008. Wenjun Jiang is also a dual PhD candidate in NanoTechnology, and concurrent master's candidate in Electrical Engineering.